Declaration

The Registrar (Academic)

University of KwaZulu-Natal (Westville)

Dear Madam

I, Marcelino Adriano Macome

Reg.:   200300066

Degree: MSc Physics

Hereby declare that the dissertation entitled **"Characterization and improvement of a direct solar radiation detector"** is the result of my own investigation and research and that it has not been submitted in part or in full for any other degree or to any other University.

_____   December 13th, 2004

Signature

Dedication

This thesis is dedicated with love and gratitude to the memory of my elder brother, to my

father Marcelino and to my sister Virginia.

Acknowledgements

Abstract

A low-cost Direct Solar Radiation Detector (DSRD) was developed in house in the Department of Physics at the University of KwaZulu-Natal (Westville). A main use of this instrument is to gather solar energy data that are to be used in the design of systems that concentrate and convert solar energy into thermal energy (concentrating solar thermal energy systems). These data are compiled into a database from which the efficiency and potential use of many solar systems can be based.

It was required that the detector was fully characterized with respect to spectral range, polar (angular) response and environmental stability. Based on this analysis it was also required to investigate possible ways of improving the detector. An Eppley Normal Incidence Pyrheliometer (NIP) mounted on an Eppley Sun Tracker (ST) was used as a reference instrument. The ST is a power driven tracker with an axis parallel to the Earth's axis of rotation. The NIP and DSRD were mounted together on the tracker in order to correlate their responses and also to calibrate the DSRD.

The results indicate that the modified DSRD works better in that it follows the reference instrument. The correlation between the NIP data and the DSRD data is better with the value of correlation factor close to unity and the root mean square error value close to zero. This means that the modifications carried out on the detector have improved the low cost in-house detector and hence the quality of data collected.

Chapter 1

1. Introduction

For any scientific discipline to remain active and productive effectively and efficiently, the power of its instrumentation must grow significantly with time. Without this growth the discipline tends to stagnate and no new discoveries are made. This means that for the field of Science and Technology the development of instrumentation is paramount. As time passes, high-level functionality and simplicity for low cost instrumentation is needed depending on the complexity of the application needs.

An accurate assessment of solar resources is based upon accurately measured data. In particular, data on the spatial distribution of measured solar radiation, especially over a period of time, can be used in models as the basis for many engineering designs and economic decisions.

In most countries, a reliable and sustainable energy supply is very crucial in the context of economic development and may often be used as a measure against poverty. Statistics show that major parts of suburban and rural Africa, and many areas in the world, are

located in non-electrified areas [Gore, 2003]. The population in these areas depends on expensive and inconvenient energy sources like wood, coal, petroleum, paraffin, batteries and candles. These are also the most polluting sources of energy. A large number of schools are located in the areas with no electricity, thereby going to enormous problems to get water pumped and well treated. A lack of good treatment of water leads to a high possibility for diseases carried by contaminated water.

Solar radiation is a guaranteed and cheap infinite source of energy to any community in any part of the world. This is especially true for the rural areas in the countries situated inside the Sunbelt (that is 40° north to 40° south) [Cuamba et al, 2001]. Solar energy does not need a grid connection as compared to other sources of energy, in particular, the nonrenewable fuels. It is thus always close to where it is needed and does not cause any negative impacts to the environment.

Solar radiation is the main energy input that determines the physical, chemical and biological dynamics of landscape processes with a direct impact on human living. An understanding of solar radiation in terms of its properties and availability is a logical start to the discussion of its practical application as a source of energy. A means to capture solar radiation and to convert it into a useful energy resource is of paramount importance. An interpretation of solar radiation data in determining the influence of solar radiation over innumerable natural dynamic processes such as natural catastrophes, climatic changes and biological effects is also very important.

1.1   Aims and objectives

A main aim of the project is the characterization and improvement of an in-house Direct Solar Radiation Detector (DSRD). The improvement on the detector is expected to ensure that good quality and reliable data are collected. Thus, an indirect objective of the project is to improve the quality and reliability of collected solar radiation data.

1.2   Solar radiation spectrum

The electromagnetic spectrum extends from a wavelength of 10^4 to 10^{-12} m [McDaniels, 1984]. A concern of this research work is only a very small part of this spectrum, the solar radiation spectrum or SRS, which extends from a wavelength of ~300 nm to ~3000 nm. The SRS is made up of three main regions; the ultraviolet (UV) region, the visible region and the infrared (IR) region [Twidell and Weir, 1996].

1.2.1   The UV region

The ultraviolet or UV region of the SRS corresponds to wavelengths less than ~380 nm [Duffie and Beckman, 1991]. Ultraviolet radiation can not be detected by the human eye. A large amount of UV radiation is absorbed by atmospheric contents before it reaches the earth's surface. The smallest part of solar energy that reaches the surface of the earth is UV radiation.

1.2.2   The visible region

The visible region of the SRS is a part of the solar radiation spectrum that can be detected by the human eye and covers a wavelength from ~380 to ~780 nm [Duffie and Beckman, 1991]. The atmosphere is almost completely transparent to solar radiation in the visible region [Twidell and Weir, 1996]. Therefore, the largest part of solar energy that reaches the earth's surface is in the visible region.

1.2.3   The infrared region

The infrared or IR region of the SRS comprises all radiation with wavelengths greater than ~780 nm [Duffie and Beckman, 1991]. Infrared radiation is emitted by all objects that are at any temperature below ~700 K [Mcdaniels, 1984]. Water vapor and carbon dioxide in the atmosphere absorb about 20 % of the radiation in the IR region [Twidell and Weir, 1996], and so only about 80 % of this radiation reaches the surface of the earth.

1.3   Characterization methods

The characterization of the DSRD has been carried out with respect to its spectral response, its polar response and its environmental stability.

1.3.1   Spectral response

The characterization of the DSRD with respect to spectral response is a detailed account of how the detector responds to different wavelengths of solar radiation. It is a

requirement that the detector responds evenly to the same amount of energy and this response must be independent of the wavelength of the solar radiation.

1.3.2 Polar response

The characterization of the DSRD with respect to polar response is an account of the behaviour of the detector when it is misaligned with respect to the normal incidence of the radiation beam. If the collimating hole in front of the detector is not at a slope equal to that of the NIP, various errors may be introduced in the readings especially by reflection from the sides of the hole such that the DSRD overheads.

1.3.3 Environmental stability

By virtue of it being a detector of solar radiation, the DSRD is placed out doors where it is subjected to certain atmospheric elements that may damage or distort the readings of the detector. It is desirable, therefore, that the detector is tolerant to the instability of environmental effects such as rain, humidity, wind and any adverse temperature changes.

1.4   Perceived improvement

Based on the preceding statements, it is perceived that an improvement of the DSRD will be based on its spectral response to direct solar radiation, on its polar response to this radiation and on its physical location.

1.4.1 Spectral response

The curve of the spectral responsivity of the DSRD indicates that even though the detector is a direct solar radiation detector, it is sensitive to IR radiation as well. Thus, it is highly likely that the detector reads direct as well as diffused radiations. Several optical glass filters will be investigated to minimize the detection of other radiations besides direct solar radiation.

1.4.2 Polar response

When light strikes any surface, it may undergo all the known optical effects. For the DSRD these effects will be maximum when the collimating hole is not properly aligned with the direction of the sunlight. This may cause detections of unwanted components of the incident solar radiation. The viewing angle of the detector must be aligned properly for the collimating hole to coincide with the direction of the sunlight.

1.4.3 Environmental stability

The housing of the DSRD is not very well sealed such that it allows moisture to accumulate onto the detector surface. The collimating hole is open to the atmosphere and so allows moisture and rain to accumulate onto the detecting surface and this will affect the readings. The black colour of the housing absorbs radiation and this may have the effect of raising the temperature of the interior of the housing which may affect the detecting surface. An increase in temperature is known to increase the measured current

[McPherson, 2004a] in diodes of this type. An improvement to the DSRD would involve proper sealing and possibly the use of a white housing.

1.5   Brief description of the DSRD

The DSRD is made up of an integrated circuit (IC) and an external circuit (EC) both of which are housed in a rectangular plastic box with holes for feeding electrical signals to a data logger and for collimating the solar beam.

The IC is an OPT101 monolithic circuit which consists mainly of a photodiode and an amplifier. The photodiode is operated in the photoconductive mode, it has an active area of 5.244 mm^2. It detects radiation in the wavelength range of ~280 to ~1100 nm and it is connected such that the incident radiation is converted into a current. Its spectral response varies with respect to the wavelength and it peaks at 850 nm [Burr-Brown, 1996]. The amplifier is connected such that it converts current generated from the photodiode into an output voltage which increases linearly with the intensity of solar radiation. This amplifier is able to handle both single and dual power supplies and is therefore ideal for battery operated equipment like the DSRD.

The EC circuit is made up of a variable resistor and a battery. The variable resistor is connected in series with the internal resistor of the amplifier in the IC, and this helps to increase the responsivity of the amplifier. The battery is used mainly for supplying power

7

to the whole circuit. However, the battery is also used for its low noise output such that the overall electrical noise of the system is minimal [McPherson, 2003].

1.6   Thesis outline

The thesis consists of five chapters, beginning with this introduction. Chapter 2 outlines the theory that served as background to this present project and consists mainly of a description of the interaction between solar radiation and the earth. In particular, a brief description of the concepts evolving in interaction between the sun, the earth and the atmosphere.

Chapter 3 is a description of the experimental procedure carried out. The experiment concentrates on measuring direct solar radiation using the DSRD to be improved. The readings from the DSRD are then compared with those of the reference instrument to establish the improvement required. Afterwards, several measurements were carried out to test the DSRD and to establish how the improvements could be incorporated. A description of the data acquisition system and the calibration technique are also included in this chapter.

Chapter 4 is a presentation and a discussion of the results, the analysis of which have established that the improvements on the DSRD have improved the quality of data taken. In this way, they show that the characterization was necessary. The thesis ends with

chapter 5 which is the conclusion based on the results. Here possible future work for further improvement of the DSRD is also presented.

Chapter 2

2. Theory

Solar radiation is a form of electromagnetic energy emitted by the sun and it travels through space in the form of a wave. There are various reasons for studying solar radiation. Often solar radiation is studied for climatological, synoptic, biological or energetic purposes. The spectral distribution of solar radiation is worthy of study since the absorption, transmission and reflection of radiation by any object is dependent upon the wavelength of the radiation as well as the type of absorbent material, the properties of the absorbing surface and the angle of incidence [Twidell and Weir, 1996].

2.1   Solar Radiation Spectrum

Solar radiation incident onto the top of the earth's atmosphere can be classified into three main regions with respect to the wavelength, and this is called the solar radiation spectrum or SRS. Figure 2.1 shows the spectral distribution of solar radiation and this

represents the compiled standard spectrum based on high altitude and space measurements [Twidell and Weir, 1996].

Figure 2.1: *A curve [...] earth-sun distance adopted [...] 1996]. The area under th[...] op of the atmosphere.*
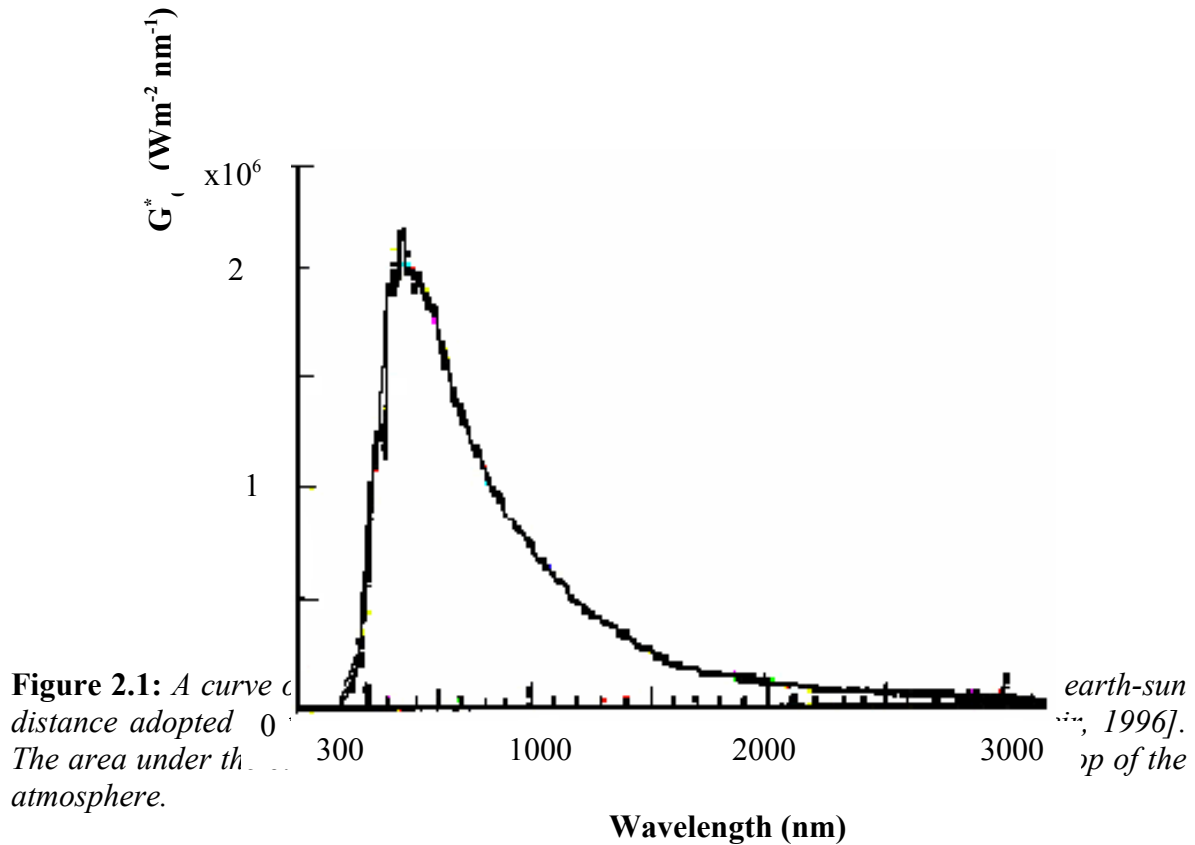
Wavelength (nm)

The <u>first</u> region of the SRS is made up of short wavelength radiation, commonly known as ultraviolet (UV) radiation. The UV itself is divided into three regions. The first region extends up to 280 nm, the second between 280 and 350 nm and the third covers the range between 350 and 380 nm. The atmosphere serves as a filter by preventing UV radiation from reaching the earth's surface. The first part of UV radiation is completely blocked by atmospheric gases like oxygen (O_2) and ozone (O_3). This first part is also radiation that is biologically harmful. The second and third parts of UV radiation are able to reach the

earth's surface even though they are severely scattered by atmospheric gases. UV radiation has a practical use in water disinfection [Twidell and Weir, 1996] because of its high potential to penetrate matter.

The second region of the SRS is made up of radiation of medium wavelengths and is called the visible spectrum since it can be perceived by the human eye. The visible spectrum is an extremely narrow band when compared to the other bands. Nevertheless, about half of the solar energy incident at sea level is in this region which extends from ~380 to ~780 nm [Duffie and Beckman, 1991]. A clear sky becomes an open window for visible solar radiation to reach the earth's surface. For this reason, the amount of solar energy measured at sea level is significantly in the visible band of the SRS.

The third and last region of the SRS extends to all wavelengths greater than ~780 nm [Duffie and Beckman, 1991] and is commonly called the infrared (IR) region. Because of the long wavelengths, it is the most highly reflected radiation of the spectrum. IR radiation can be emitted by any object at temperatures lower than ~700 K [McDaniels, 1984], even at ambient temperature. IR radiation represents almost 50 % of extraterrestrial solar radiation and ~20 % of this is absorbed by water vapor and carbon dioxide present in the atmosphere. This IR radiation represents a small fraction of energy emitted by the sun and measured at sea level.

Approximately 99 % of solar energy reaching the earth's surface is contained in the region between 300 and 3000 nm. The distribution of solar energy as shown by the SRS

indicates that 9 % of solar energy reaching the earth's surface is in the UV region, 49 % is in the visible spectrum and 42 % is in the IR region. This is based on an air mass ratio equal to 1 [McDaniels, 1984]. This absorption at different wavelengths is shown in the spectrum of Figure 2.2.
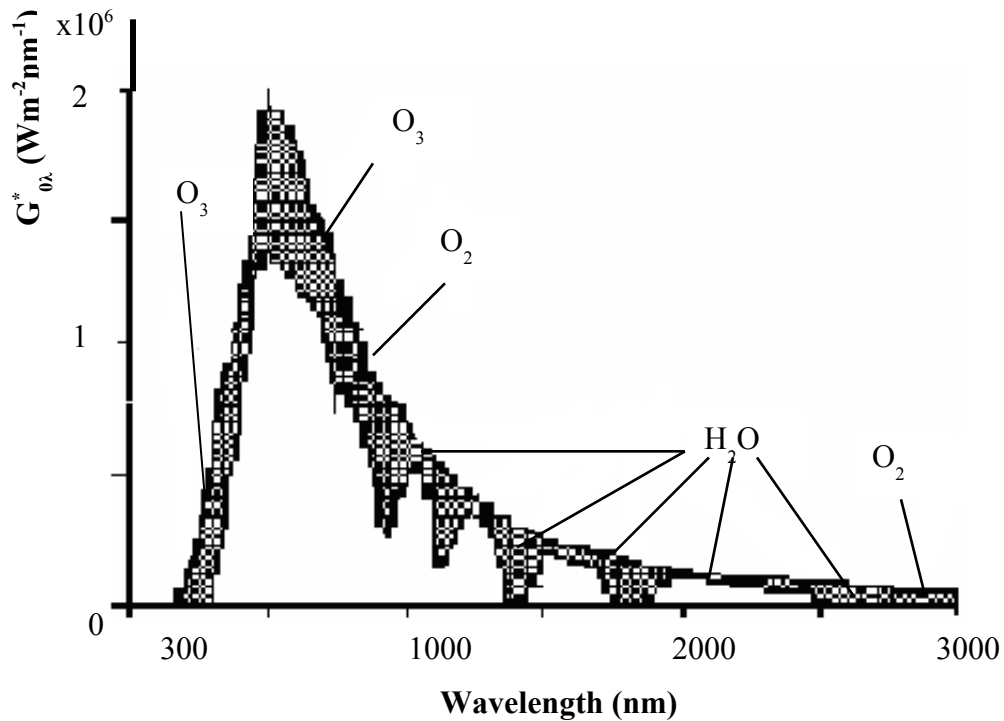
Figure 2.2: *The SRS based on the solar radiation measured at sea level [after Website 2]. This spectrum reveals the attenuation of solar radiation by the atmosphere. The shaded area indicates the radiation that does not reach the earth.*

2.2   Attenuating effect of the earth's atmosphere

The solar radiation that reaches the top of the terrestrial atmosphere is referred to as extraterrestrial radiation. The estimated amount of this radiation per unit time, per unit area (of a surface perpendicular to the direction of propagation), at mean sun-earth distance, is 1367 Wm^{-2}. This figure has been adopted by the World Radiation Center

(WRC) and is called the solar constant [Duffie and Beckman, 1991]. Nevertheless, almost half of this radiation is absorbed by air molecules or reflected and scattered by clouds and small atmospheric particles before it reaches the earth's surface.

The absorption and scattering levels of the atmosphere depend on the amount of air mass between the observer and the sun. This means that the absorption and scattering mechanisms are functions of the number of particles that the radiation must pass through. Solar radiation scattering is also a function of the size of particles relative to the wavelength of the radiation [Website 2]. The air mass is basically comprised of water vapor, gases and solid particles that are present in the atmosphere.

The path length of solar radiation towards the earth's surface through air molecules changes with time and this will be discussed in Section 2.3. The lower the sun is in the sky with respect to a detector (or to an Observer) on the earth's surface (that is around sunrise or sunset) the longer the path length between the sun and the earth's surface. It is also valid to say that in this situation, the air mass between the sun and the earth is greater. The minimum amount of air mass occurs at solar noon in any given clear day.

The attenuation of solar radiation by gas constituents in the atmosphere describes clear and dry conditions and is given by the optical air mass and the optical thickness. The blue color of the clear sky is a result of blue light scattering by air molecules in the third region of the UV spectrum. When the sun rises or sets, the path of the solar beam is

longer with the result that the blue light scattering is more pronounced such that red light is dominant. The overall result is that the sky appears red [Website 2].

Clouds are the strongest attenuators of solar radiation. This attenuation depends on the optical properties of the clouds, the position and number of layers of clouds through the atmosphere, as well as the thickness and density of the clouds [Website 4]. The most significant process in cloud attenuation is reflection. Very dense clouds, about a km in thickness, are said to reflect back into space 90 % of the incident solar radiation [Website 1]. Figure 2.3 is a diagram that summarises the different attenuation aspects of solar radiation.

In many applications, a study of solar radiation under clear sky conditions is very important. Maximum solar energy is obtained when the sky is clear and dry. Terrain topography like inclinations, as well as shadowing effects of neighboring terrain features, modify the radiation input to the earth's surface in different locations. The elevation above sea level determines the attenuation of radiation by the thickness of the atmosphere [Website 4].
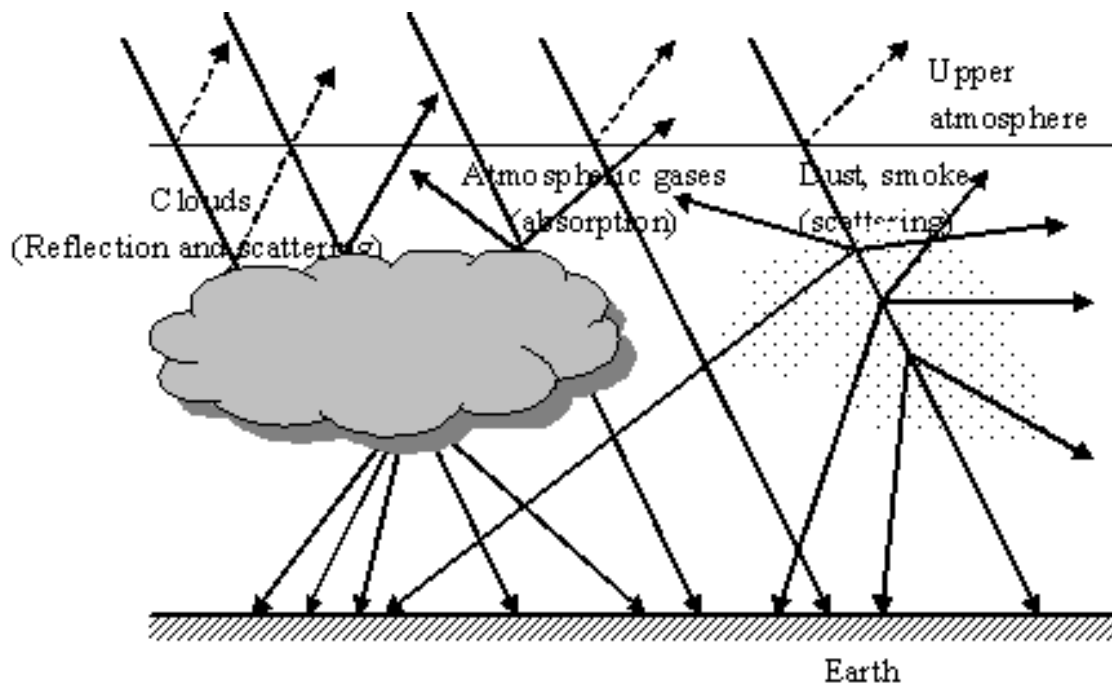
Figure 2.3: *A diagram that shows the attenuation of solar radiation by atmospheric components and the significant attenuating process for each atmospheric constituent [after McDaniels, 1984].*

2.3 Sun-Earth geometry

A measurement of direct solar radiation requires a sun tracking system for continuous readings. The position of the sun in the sky for a given latitude, longitude, year, day and time can be determined from the geometry of the sun-earth system and is very important for a good orientation of the collector surfaces.

To an observer on the earth the sun apparently moves across the sky following a circular arc from horizon to horizon [Website 3]. Figure 2.4 is a schematic representation of the path of the sun across the sky and of the incident beam through atmosphere towards the

16

surface of the earth for a given day. The basic parameters for the determination of the sun's position for a particular time are also indicated.

Figure 2.4 shows that the strength of the incident solar beam for any horizontal surface depends on the position of the sun in the sky and this is defined by a zenith angle, θ. The greater the value of θ, the weaker the incident solar radiation and this means that the path length of the incident solar radiation is larger for a large value of θ. The opposite is also true.
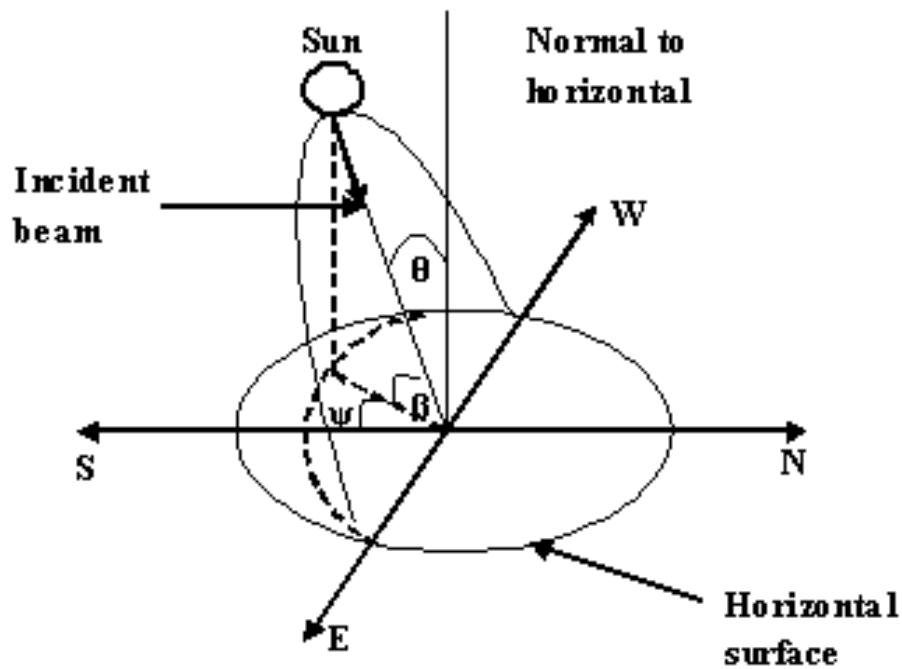
The

Figure 2.4: *A diagram that shows the sun's path as seen by an observer on the earth's surface for a given day. The sun's position can be described in terms of the zenith angle (θ), the azimuth angle (Ψ) and the solar altitude angle (β).*

declination (δ) is the angular position of the sun at solar noon with respect to the plane of the equator [Duffie and Beckman, 1991]. In other words, it is the latitude of the point where the sun is overhead at solar noon, south negative. It varies from $-23.45°$ to $23.45°$

throughout the year according to the variation of the seasons. The declination expresses the tilt of the axis of the earth rotation relative to the sun for a given day. Figure 2.5 illustrates the variation of the declination with respect to the earth's plane of rotation for particular days during the year. It is of interest to mention that the declination varies smoothly from a positive number at midwinter to a negative number at midsummer for the southern hemisphere.
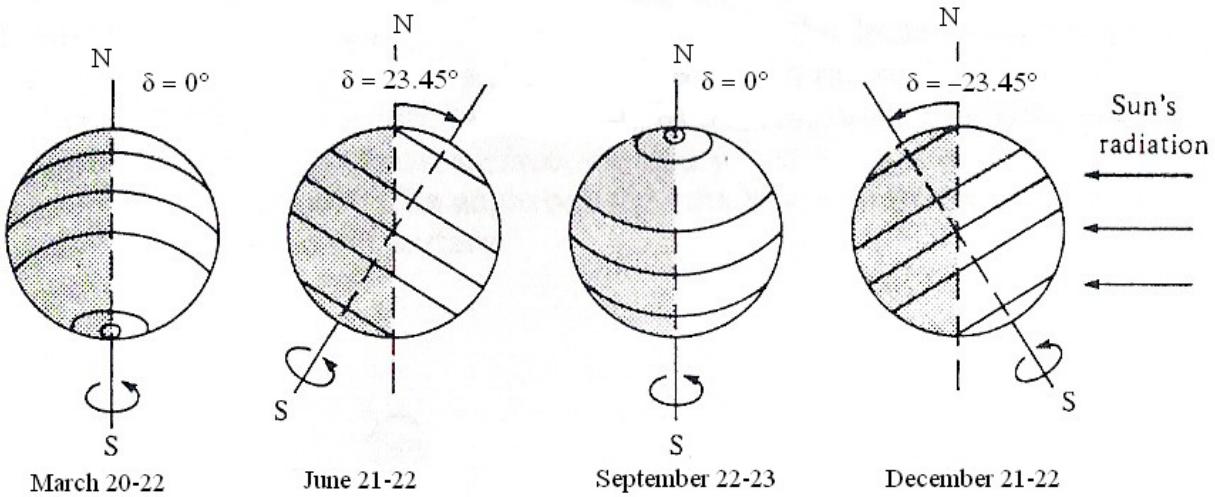
Figure 2.5: *The earth as seen from a point far from its orbit and the variation of the declination for particular days of the year for the southern hemisphere [after Twidell and Weir, 1996]. In June, the north pole is inclined near to the sun and so has more sunshine, while in December the same is true for the south pole.*

Several definitions based on empirical approximations are presented in the literature for the declination. One of them is [Duffie and Beckman, 1991]

$$\delta = 23.45 \sin\left[\frac{360}{365}(284 + n)\right] \tag{2.1}$$

where 23.45 is the maximum value of the sun's declination (δ_o) when the sun is exactly above one of the tropics and this corresponds to December 21-22 and June 21-22 (see Fig. 2.5). The value of 360 is the maximum angle of revolution of the earth around the

18

sun in a 365 day-long year and *n* is the day number in a year where on 1st January n = 1 and on 31st December n = 365 (or 366 in a leap year). The value of *n* for any day of the month can be found by use of Table 2.1. Here, the value of 284 is an empirical value suggested by Duffie and Beckman [1991].

Table 2.1: *The number of days in a year (n) for the jth day of the month [after Duffie and Beckman, 1991]*

Month	*n* for jth day of month	Date (j)	*n* day of year
January	j	10	10
February	31+j	20	51
March	59+j	2	61
April	90+j	15	105
May	120+j	11	131
June	151+j	17	168
July	181+j	25	206
August	212+j	30	242
September	243+j	10	253
October	273+j	21	294
November	304+j	18	322
December	334+j	31	365

Note: In a leap year February has 29 days in this case on 31st December n = 366.

The **solar altitude** (β) is the angle in a vertical plane between the sun's rays and the projection of the sun's rays on the horizontal plane, while the **latitude** (φ) is the angular location of a given point on the earth's surface south or north of the equator and it is considered positive in the north. It varies between -90° at the South Pole and 90° at the North Pole.

The **azimuth angle** (ψ) is the angular displacement of the projection of beam radiation on the horizontal surface, measured from the south. Conventionally, in the southern

hemisphere, ψ is negative for surfaces that face east of north and positive for surfaces that face west of north [Duffie and Beckman, 1991]. The **hourly angle** (ω) represents the angular displacement of the sun. This is measured east or west of the local meridian due to the earth's rotation around its axis at one degree per four minutes. The hourly angle is negative in the morning and positive in the afternoon.

The **zenith angle** (θ) is the angle between the sun's rays and the local vertical. This is the angle of incidence of beam radiation with respect to an imaginary line perpendicular to a horizontal surface at the site in question. The zenith angle changes from 0° when the solar beam is perpendicular to the horizontal surface, to 90° when the sun is at the lowest point in the sky. For a horizontal surface, the zenith angle is defined analytically as

$$\cos\theta = \cos\varphi \ \cos\delta \ \cos\omega + \sin\varphi \ \sin\delta \qquad (2.2)$$

where φ is the local latitude, δ is the sun's declination and ω is the hourly angle. The **angle of incidence** (θ_0) is the angle between the line of incident solar radiation onto a surface and the normal to that surface. If the surface is placed horizontally, $\theta = \theta_0$. Maximum solar radiation collection occurs when the surface of a solar collector is placed such that the angle of incidence is equal to zero and this is when the solar beam is normal to the surface.

Although, the earth's orbit is assumed to be circular in most cases, it is actually elliptical. Therefore, the distance between the sun and the earth changes as the earth makes its passage around the sun throughout the year and this causes the seasons. The earth's daily rotation around its axis and its yearly revolution around the sun both contribute significantly to the variation and distribution of solar radiation over its surface. Figure 2.6

illustrates the orbit of the earth and the variations in the distance between sun and earth during the earth's revolution around the sun.
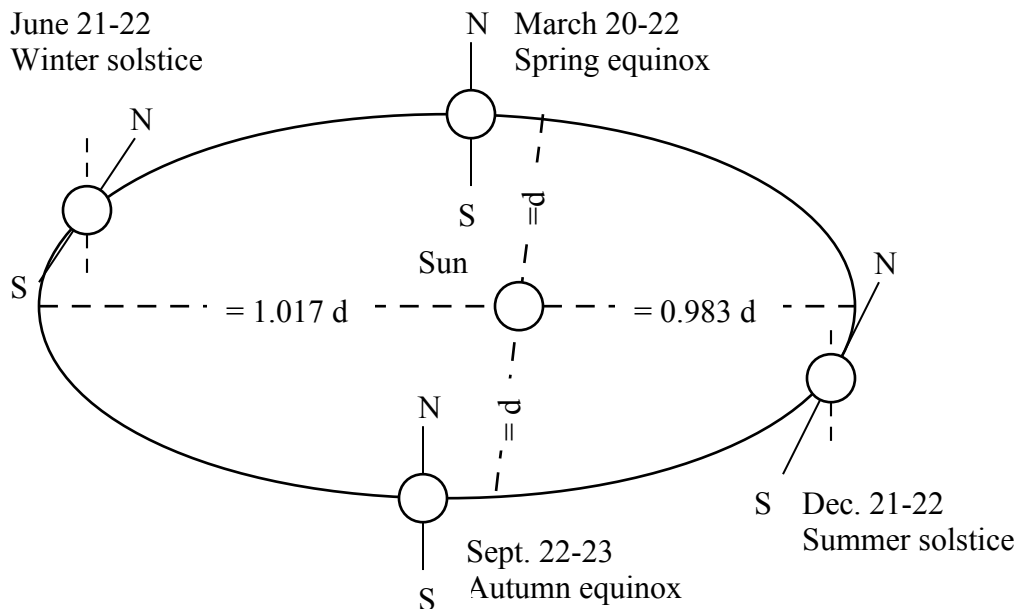
Figure 2.6: *The orbit of the earth around the sun showing the solstice and equinoxes, as well as the changes in the sun-earth distance during the earth's revolution*

The daily rotation of the earth around its axis and the interaction between sun's rays and the earth's surface is shown in Fig. 2.7.
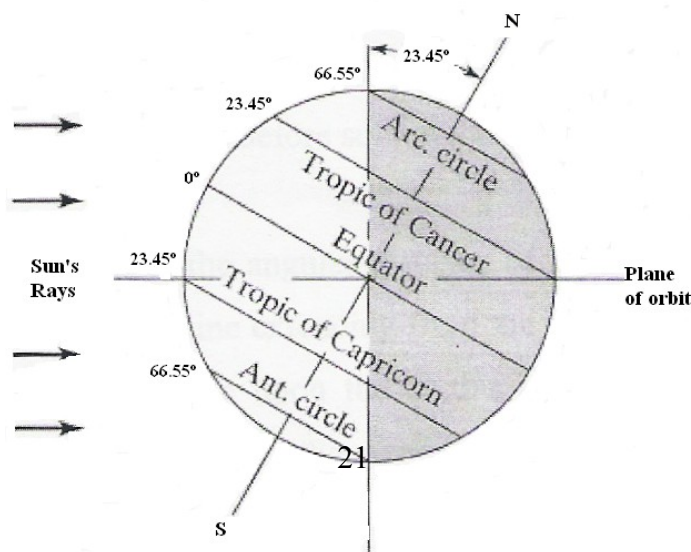
Figure 2.7: *A representation of the sun's rays as they interact with the earth's surface [after Website 3]. As the earth rotates, the points located in the shaded part move towards the illuminated part of the earth.*

In addition to this, the changing length of daylight and darkness as well as the changing of seasons has to be taken into account in any calculations and designs.

When the sun sets, the zenith angle $\theta = 90°$ and by Eq. (2.2), the sunset angle will be given by

$$\cos\omega_s = -\tan\varphi\,\tan\delta \tag{2.3}$$

where ω_s is the sunset angle, which is just the angular displacement of the sun as measured with respect to solar noon. The length of day is a function of declination and latitude. Since Eq. (2.3) gives the length of the day from midday it is multiplied by 2 to obtain the length of day N, hence

$$N = \frac{2}{15}\cos^{-1}\left(-\tan\varphi\,\tan\delta\right) \tag{2.4}$$

where 15 (=360°÷24 hours) is used to convert the result in Eq. (2.4) from degrees to hours since the earth covers 360° in 24 hours, δ is the angle of the sun's declination and φ is the latitude of the location.

2.4   Solar time (*ST*) and local clock time (*LCT*)

Solar time is a basic parameter used in solar radiation calculations and does not coincide with local clock time [Duffie and Beckman, 1991]. A clock day is exactly 24 hours while a solar day differs slightly at ~24.25 hours [Website 3]. This is because the earth's rotation and the obliquity of the earth's orbit are not regular. The earth, during its rotation and revolution, is subjected to gravitational interactions with other planets in the solar system. These interactions are one of the sources of the differences in time. In scientific or engineering calculations it is necessary to convert clock time to solar time for better accuracy.

The equation of time gives the difference between solar time and local clock time. It is given by [Website 3]

$$E = 0.165\sin 2B - 0.126\cos B - 0.025\sin B \tag{2.5}$$

in hours, where *B* is a day angle in degrees and is given by

$$B = \frac{360(n-1)}{365} \tag{2.6}$$

where 360 is as defined in Eq. (2.1) for a 365 day year and *n* is the day number in a year. The relationship between solar time (*ST*) and local clock time (*LCT*) is given by

$$ST = LCT + \frac{1}{15}\left(L_{std} + L_{loc}\right) + E \tag{2.7}$$

where 15 is as defined in Eq. (2.4). Here L_{std} is the longitude of the Standard Meridian for the local time zone and L_{loc} is the longitude of actual location both in degrees west and degrees east according to localization of the observer in relation to Greenwich Meridian.

Once solar time is established, the hour angle ω can be calculated. By noting that the hour angle varies at the rate of 15º per hour, that $\omega = 0$ at solar noon and that the sign convention is $\omega < 0$ before solar noon, the equation for hour angle is

$$\omega = 15(ST - 12) \tag{2.8}$$

where 12 is the number of hours elapsed from solar midnight to noon.

2.5 Spatial distribution of solar radiation

Solar radiation is unevenly distributed [Website 1], varies in intensity from one geographic location to another and depends on the latitude, longitude, elevation, season and time of day. A large area of the southern hemisphere is occupied by the oceans and this factor contributes strongly to the amount of cloud cover. This is one source of the difference between the southern and northern hemispheres in terms of the availability of solar radiation.

The geographic distribution of total solar radiation on a global scale is divided according to its intensity into four broad belts around the earth [Website 1]. Figure 2.8 illustrates the geographic distribution of solar radiation. This distribution is very important for the

Best conditions   **Good conditions**   **Fair conditions**   **Poor conditions**
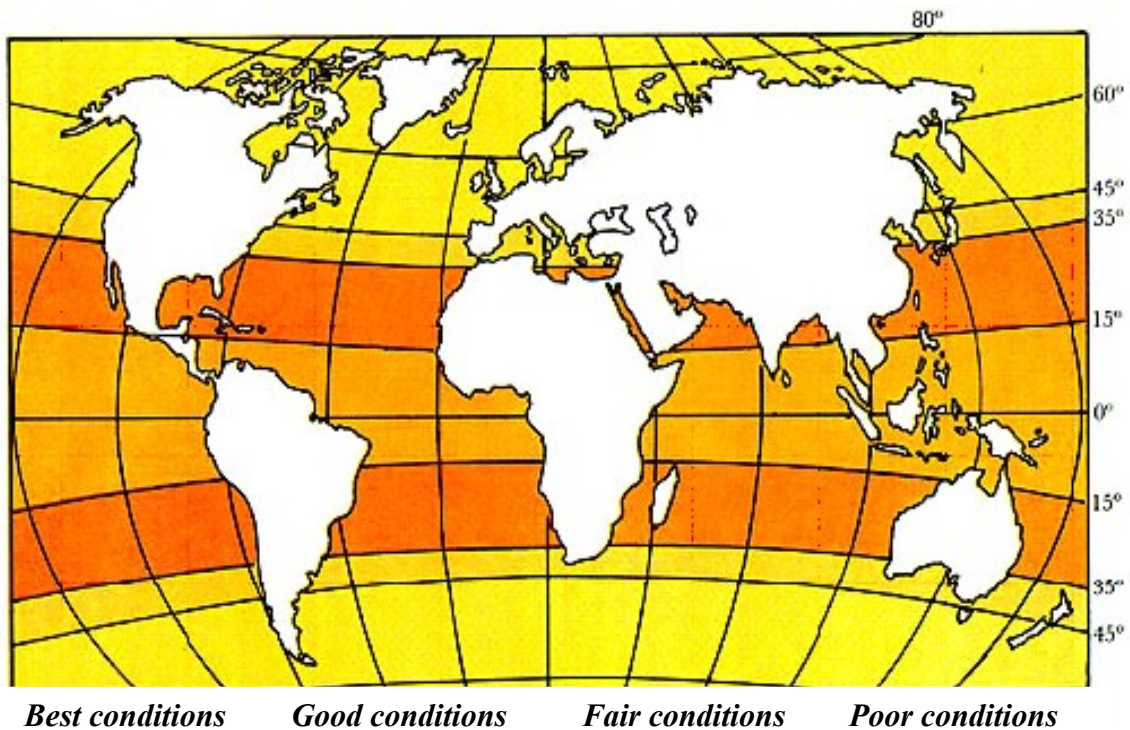
Figure 2.8: *A worldwide distribution of solar radiation into belts indicating the feasibility of solar applications [after Website 1] around the globe.*

assessment of the feasibility of solar applications in different locations around the globe.

2.5.1   The belt with the best conditions of sunshine.

The best conditions belt corresponds to regions situated between latitudes 15º and 35º south (or north) of the equator. These regions are climatically semi-arid and so they receive large amounts of direct solar radiation, mainly because of limited cloud coverage

25

and rainfall throughout the year. It is estimated that 3000 hours of sunshine per year are available [Website 1] in this belt.

2.5.2 The belt with good conditions of sunshine

The regions of good conditions of sunshine comprise the region between latitudes 15º south and 15º north of the equator. Unlike the belt with the best conditions, the cloud cover here is most frequent, with the consequence that the precipitation level is high. Associated with a high frequency of precipitation is high humidity with the consequence that there is a high proportion of scattering and reflection of solar radiation. The average number of sunshine hours is estimated at 2500 per year in this belt [Website 1]. The annual variation of solar radiation is not significant in this belt simply because seasonal variations are also not significant [Website 1]. This is consequent to the fact that the annual change in declination is small and so the annual change in sun-earth distance is also small.

2.5.3 The belt with fair conditions of sunshine

The regions with fair conditions of sunshine lie between 35º and 45º both sides of the equator. In these regions the inclination of the axis of the earth changes considerably and this leads to changes in the sun-earth distance. As a result of this significant variation in the sun-earth distance, seasonal variations as well as hours of sunshine are greater than in other belts. Despite this, the average sunshine hours is roughly the same as for the two

belts (~2500 hours) [Website 1] already described. This is because the annual level of humidity is lower and thus, a lower frequency of cloud coverage.

2.5.4 The belt with poor conditions of sunshine

The belt with poor conditions of sunshine covers latitudes further than 45º both sides of the equator. In these regions, half of the total solar radiation reaching the earth's surface is diffuse radiation, and this is because the solar radiation is scattered by the large amounts of air mass that it traverses. There is a large air mass to traverse because to an observer on earth in these regions, the sun is further away. The scattering occurs at a higher proportion in winter than in summer, mainly because of a frequent and extensive cloud cover [website 1]. The annual average hours of sunshine is estimated at <2500.

Other factors that determine the spatial distribution of solar radiation are based on the sun's position above the horizon and can be calculated using astronomic formulas [Website 4] and parameters such as latitude, declination and hourly angle.

2.6   Solar radiation components

The solar radiation that arrives at the earth's surface consists fundamentally of three components. These are direct (beam), diffuse (sky) and reflected solar radiation.

2.6.1 Direct (or beam) solar radiation

Direct solar radiation is radiation that reaches the earth's surface without having been scattered by the atmosphere. Direct solar radiation is a very important variable in the assessment of the performance of solar energy systems capable of concentrating solar radiation. However, there is a worldwide shortage of radiometric stations with the capability to measure direct solar radiation or solar radiation in general [Rivington et al, 2002]. Some methods have been developed for estimating direct solar radiation and these are based on available data. To predict the amount of direct solar radiation it is assumed that the solar beam traverses a path clear of all particles.

2.6.2 Diffused (or sky) solar radiation

Diffused (or as conventionally called, diffuse) solar radiation refers to that radiation which comes from the entire sky. This is the radiation received from the sun after it has been scattered by the atmosphere. Diffuse solar radiation is typically of short wavelength and is therefore more scattered by the atmosphere. On clear days diffuse solar radiation is small compared to direct solar radiation, but for scientific calculations it cannot be ignored. On completely cloudy days only this radiation may reach the earth's surface. To predict the amount of diffuse solar radiation on the earth's surface it has been assumed that the sky is the diffuse source and that it is a uniform radiator of this type of radiation [Myers, 2003].

2.6.3 Reflected solar radiation

Reflected solar radiation is that radiation which reaches the earth's surface after its direction has been changed by surrounding objects like clouds, buildings and trees. Generally, the amount of solar radiation reflected from the surface of an object depends on the location of the object, the orientation of the surface and the solar reflectance characteristics of the surrounding surface [Website 3]. The reflectance of the ground, for example, varies with the type of ground cover.

The total amount of solar radiation incident onto a surface per unit area per unit time is called irradiance. It is calculated at any instant as a sum of the above three components of solar radiation.

2.7 Direct solar radiation measurements

Instruments that are used for measuring solar radiation are generally referred to as radiometers. They are grouped differently according to the detection principle used. Common principles include thermomechanical, thermoelectrical, calorimetric and quantum or photodetection principles. Direct solar radiation detectors are constructed generally in a telescopic design meaning that the solar beam is collimated. In general, the sensing element receives only radiation from the sun through a narrow angular aperture.

2.7.1   Thermomechanical detection

Detection by the thermomechanical principle is based on thermodynamic expansion. The sensing element consists of a bimetallic strip. The absorbed solar energy heats the strip and this results in bending of the strip proportional to the amount of incident solar energy. The resulting curvature of the strip is normally transmitted mechanically to a writing pen that draws a characteristic graph on a specially prepared paper [Uiso, 2004].

2.7.2   Thermoelectrical detection

Detection by the thermoelectrical principle also utilizes the heating effect of solar radiation. Here the detecting element is a transducer. The amount of solar energy absorbed is converted first into heat which then causes a rise in temperature at the junction of the transducer and this generates a current that can be measured. Examples of thermoelectrical devices are the pyroelectrics, the thermistors and the thermocouples. These are described below.

In *pyroelectric devices* the absorbed radiation produces a change in the temperature of the pyroelectric material. The change in temperature causes a change in polarity resulting in a polarization current. This current is thus dependent on the rate of change of the temperature on the pyroelectric material [Odon, 2001]. This constitutes the difference between pyroelectric devices and other thermoelectrical devices in which the output signal depends only on the value of the temperature and not on its variation.

Thermistors are made from a semiconductor material. The detection principle lies in the inter-dependence between temperature and semiconductor resistance. The resistance of a semiconductor decreases with increasing temperature and can be expressed [Guyot, 1998] as

$$R(T) = R_0 \left(\frac{1}{T} - \frac{1}{T_0} \right) e^b \tag{2.9}$$

where R is the resistance at absolute temperature T, R_0 is the resistance at the reference temperature T_0 and b is a constant depending on the material of which the semiconductor is made.

A *thermocouple* is made up of two conductors made of two different materials. The basic principle relies on the temperature difference between two junctions of the thermocouple. One is in contact with a surface that absorbs solar radiation and is called a hot junction, the other is in contact with a surface that does not receive any solar radiation and is called a cold junction [Myers, 2003]. The temperature of the cold junction serves as a reference. The differential heating is achieved by having the hot junction painted with a non-selective black paint of high absorbtance and the cold junction painted with a white paint of high reflectance. Figure 2.9 is a diagram of a thermocouple.
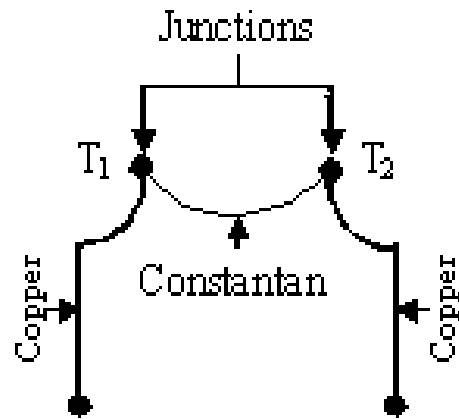
Figure 2.9: *A thermocouple design where T_1 and T_2 are the temperatures at the junctions [after Guyot, 1998].*

When solar radiation is incident onto the junction, an electromotive force (emf) is created across it. This emf is a function of the temperature difference between the junctions and the type of conductive material used [Uiso, 2004]. The emf developed in a single thermocouple is normally very small such that the thermocouple is not suitable for measuring small temperature differences [Guyot, 1998; Uiso, 2004]. To increase the suitability, several thermocouples are often arranged in series to form a thermopile. The emf is then multiplied by the number of thermocouples.

The basic function of a thermocouple is explained by the Seebeck effect, which is a combination of three effects; the Peltier effect, the Volta effect and the Kelvin effect [Guyot, 1998]. The *Peltier effect* occurs when current passes through a junction of two conductors such that a certain amount of heat is absorbed or released according to the direction of the current. The ratio of the heat to the current is a constant. The *Volta effect* occurs when two conductors or semiconductors are in contact such that a potential

difference is created between them. This potential difference depends only on the nature of the conducting material. The *Kelvin effect* occurs when two pieces of the same conductor are brought to different temperatures, such that electrons move from the piece at higher temperature to the one at lower temperature. An internal electric field is produced that follows the temperature gradient [Guyot, 1998]. Modern designs incorporate a potentiometer to generate voltage when a change of temperature is detected [Website 5].

Thermoelectrical detectors are the most widely used because they exhibit good stability and their spectral response does not depend on the wavelength of the incident solar radiation, but on the amount of energy contained in the incident solar radiation.

2.7.3   Calorimetric detection

Detection by the calorimetric principle is based on the heating effect of solar radiation on a fluid. A blackbody cavity forms the detecting device in some calorimetric detectors. The cavity absorbs incident solar energy which is converted into heat. Water is then circulated around the cavity and heated up. The amount of solar energy absorbed is determined from the temperature of the heated water and its flow rate. A main disadvantage of this detecting device is that it does not give instantaneous readings nor does it convert the heating effect into an electrical signal. It is therefore not widely used [Website 5].

2.7.4 Quantum detection

Detection by the quantum principle is based on direct conversion of solar radiation into an electrical signal. Quantum (or semiconductor) detectors are represented predominantly by silicon photodiodes and are becoming the most popular, easy-to-use devices [Duffie and Beckman, 1991]. However, their use is often limited to a specific wavelength or spectral band since they respond selectively to the wavelength of the incident radiation. In other words, their spectral responses vary with respect to the wavelength of the solar radiation spectrum. Nevertheless, the most interesting aspect in quantum detectors is the changing radiation levels which are mainly instantaneous and linear. In general, the temperature dependence is very small [Duffie and Beckman, 1991] and this makes quantum detectors very important for measuring highly fluctuating events. Henceforth, the term quantum will be used for the description of the detectors that use the direct conversion of solar radiation into an electric signal.

2.8   Commercially available DSR instruments

The most common and commercially available instruments for measuring the available direct solar radiation are pyrheliometers. Their construction is typically telescopic, which means that the detected radiation reaches the detecting device through a narrow aperture. The initial development of the pyrheliometer was influenced by an interest in the determination of the value of the solar constant [Uiso, 2004]. There are different designs of pyrheliometers and a brief description of the four main designs is given below.

34

2.8.1 Description of Pyrheliometers

a) *The absolute cavity pyrheliometer*

The absolute cavity pyrheliometer (ACP) consists of cavities painted with a highly absorbing black paint. This type of pyrheliometer is absolute because it is self-calibrated [Uiso, 2004]. The evolution of the ACP is described by Duffie and Beckman [1991]. Because of its high accuracy, this pyrheliometer serves as a basis for determining the solar constant and also as a basis for the World Radiometric Reference (WRR). Figure 2.10 is a diagram of the cavities that constitute the sensing element in an ACP.
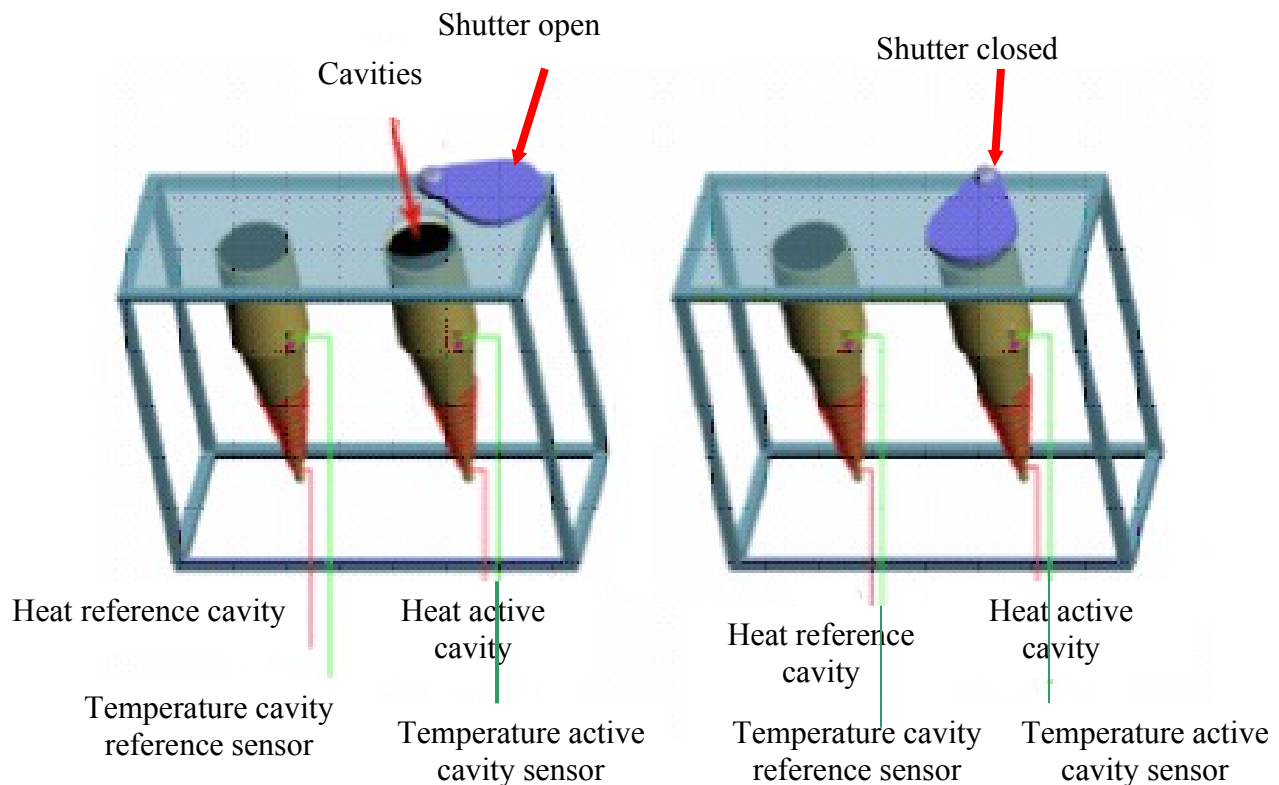
Figure 2.10: *A diagram of the cavities that constitute the sensing elements in an absolute cavity pyrheliometer. The active and reference cavities are maintained at the same temperature. The reduction in required electrical power to maintain this balance when incident light is absorbed by the active cavity is a measure of the incident power.*

An example of an ACP is the Eppley absolute cavity pyrheliometer. It consists of primary and secondary cavities which are painted black. In operation, the primary cavity is

alternately shielded from and exposed to, solar radiation and the temperature difference between the cavities maintained by electrical heating [Uiso, 2004]. The power supplied to the heater is decreased if the cavity is exposed to solar radiation (or increased if the cavity is shielded from solar radiation). The electrical power necessary to maintain the temperature difference is equivalent to the change in incident solar radiation. This is [Uiso, 2004]

$$H = k(P_1 - P_2)$$ (2.10)

where H is the decrease in electrical heating, k is a constant determined for each ACP, P_1 is the supplied electrical power when the cavity is shielded from the solar beam, and P_2 is the electrical power when the cavity is exposed to the solar beam.

b)   *The Ångström compensation pyrheliometer*

The Ångström compensation pyrheliometer (ÅCP) consists of two equal blackened manganin plates set such that they can be shielded from the sun [Duffie and Beckman, 1991]. Each plate is fitted with a copper-constantan thermocouple in such a way that each can be electrically heated. A diagram of the Ångström compensation pyrheliometer is shown in Fig. 2.11.

When measuring solar radiation one plate (P2) is shielded from the sun and supplied with an electric current. The current is adjusted to cancel the thermal difference with the other plate (P1) which is exposed to the solar beam. In the measurement process the plates are shielded alternately using reversible switches (S1 and S2) to compensate any faults in the symmetry of the device [Guyot, 1998].

36
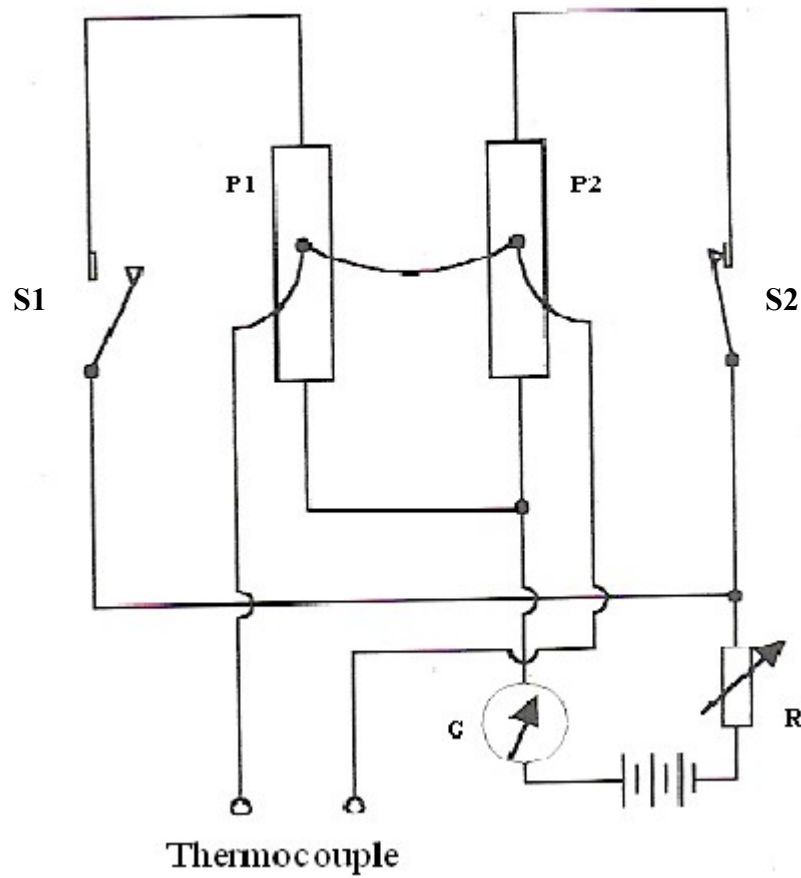
Figure 2.11: *A circuit diagram of the Ångström compensation pyrheliometer in which R is a temperature dependent variable resistor and G is a galvanometer which indicates the current flux.*

The amount of solar radiation absorbed is equal to the electrical power dissipating into the plate that has been shielded from the sun, hence

$$E_s = kI^2 \qquad\qquad (2.11)$$

where E_s is the energy generated by the direct solar radiation, k is the calibration constant and I is the current from the heating element. The calibration constant depends on the resistance of the plate, its area, the coefficient of absorption of the material that composes

the plate and the paint. The output of the ÅCP is an electrical signal that can be measured as a current.

c) *The Kipp & Zonen actinometer*

The Kipp & Zonen actinometer (KZA) is a pyrheliometer whose characteristics are based on the Linke-Foussner design [Duffie and Beckman, 1991]. It consists of a 40-junction constantan-manganin thermopile with hot junctions (heated by solar radiation) and cold junctions. All these junctions are contained in a case. The cold junctions are kept in thermal contact with the case. This case contains massive copper rings with a very large thermal capacity to prevent any influence of solar radiation on the temperature of the cold junctions [Guyot, 1998]. The large thermal capacity also serves to limit any oscillations of the temperature inside the case. The temperature of the hot junctions increases rapidly when they are exposed to the solar radiation. A measure of the direct solar radiation is given by a difference in temperatures between the hot junctions and the cold junctions. This difference generates an electrical current that can be measured as a voltage drop across a resistor placed at the output of the thermopile, using a data logger or a voltmeter.

d) *The Eppley Normal Incidence Pyrheliometer (NIP)*

The normal incidence pyrheliometer (NIP) measures the direct component of solar radiation at normal incidence. The pyrheliometer consists of a brass tube that has been painted black inside and that incorporates on its base a multijunction thermopile [Duffie and Beckman, 1991]. The tube is filled with dry air at atmospheric pressure and sealed at the viewing end by an infrasil II (or quartz) window which is 1 mm thick [Website 6].

The instrument is fitted with a manually rotatable disc which can accommodate three filters and leave one aperture for measurements of the total short wavelength spectrum (~100 to ~3 000 nm). The radiant heat raises the temperature of the thermopile which produces an electrical signal and this is measured as a voltage. Fig. 2.12 shows a photograph of the instrument that has been used in this research work.
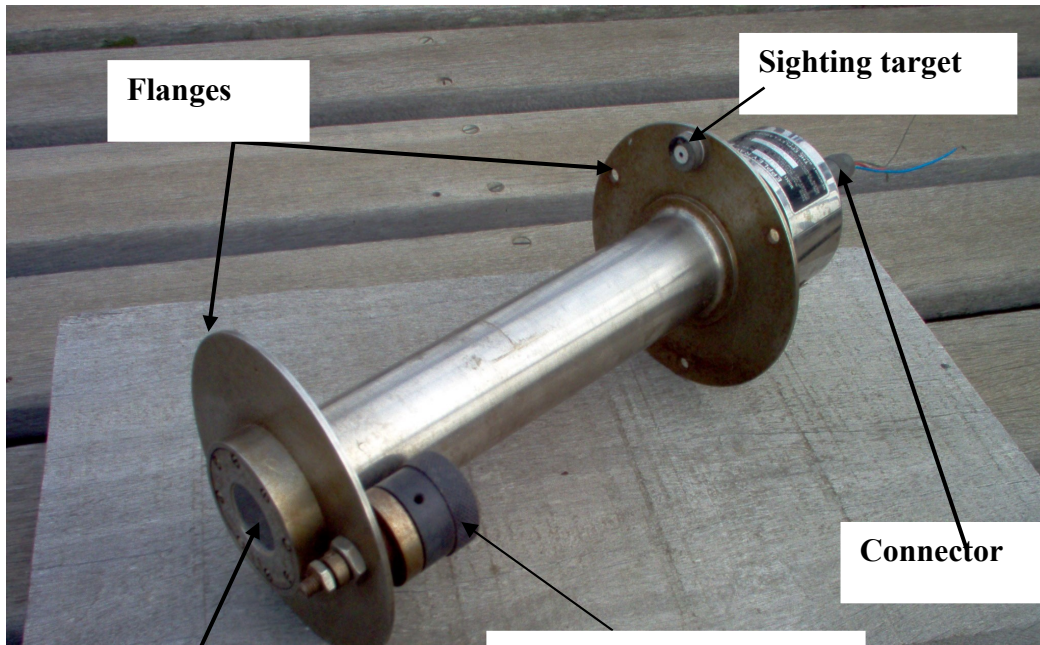
Figure 2.12: *A photograph of the Eppley Normal Incidence Pyrheliometer (NIP) showing the viewing window and the sighting target.*

The NIP has two circular flanges which are provided with a detection arrangement for alignment of the pyrheliometer to the sun. The flanges are placed at each end of the tube. The aperture angle (or the full angle field of view) of the pyrheliometers varies from design to design and ranges from 3° to 15°. This variation in aperture angle is influenced

by different objectives in view [Ångström and Rodhe, 1996]. The aperture angle of the NIP used in this work is 5.7º.

2.8.2   The Pyrheliometric scale

The latest Pyrheliometric scale was established in 1975 and this is the world radiometric reference (WRR). The WRR was established by using a group of high-accuracy, self-calibrating, absolute cavity pyrheliometers of different types. Numerous comparisons were carried out between pyrheliometers during the International Pyrheliometer Comparison (IPC) meetings held every 5-years in Davos, Switzerland [Guyot, 1998; Uiso, 2004]. The World Meteorological Organization (WMO) maintains the WRR at the Physical Meteorological Observatory (PMO) in Davos [Myers, 2003]. The WRR represents the sum of direct solar radiation and atmospheric radiation in the field of view of the measuring instruments, with an accuracy better than ± 0.3 % [Guyot, 1998].

2.8.3   Classification of pyrheliometers

Pyrheliometers are classified as standard, first class and second class. The standard class includes all pyrheliometers which are highly accurate and self-calibrated so that they constitute the best class of pyrheliometers. The first class is that with good stability calibrated against the standard class. The second class is made up of those pyrheliometers that are in continuous field operation and these are the worst compared to the standard and first classes. This classification is based on criteria established by the Commission for Instruments and Methods of Observation (CIMO) of the WMO [Guyot, 1998; Uiso,

2004]. The classification criteria for the pyrheliometer takes into account several aspects and these are the sensitivity, the stability, the temperature, selectivity, linearity and time constant of the instrument. Table 2.2 summarizes the details of the criteria.

Table 2.2: *A summary of the criteria used in the classification of pyrheliometers [after Uiso, 2004]*

	Standard	First class	Second class
Sensitivity (mWcm^{-2})	± 0.2	± 0.4	± 0.5
Stability (% change per year)	± 0.2	± 1.0	± 2.0
Temperature (max. % error due to ambient variation)	± 0.2	± 1.0	± 2.0
Selectivity (max. % error due to leaving from assumed spectral response)	± 1.0	± 1.0	± 2.0
Linearity (max. % error due to non-linearity)	± 0.5	± 1.0	± 2.0
Time constant max. (sec.)	25	25	60

According to the above criteria, the ACP and ÅCP are classified as standard pyrheliometers, the NIP and the KZA as first class pyrheliometers while the rest of pyrheliometers belong to the second class group.

2.8.4 Calibration and standardization of DSR instruments

The calibration and standardization of DSR instruments aims mainly to establish the accuracy of the pyrheliometers, and to normalise a measurement to the same scale [Uiso, 2004]. A Calibration is, further to this, dedicated to the determination of the

characteristics of the pyrheliometer and proper factors to convert an output value to an equivalent radiant flux unit.

Any pyrheliometer can be calibrated by comparison with a first class pyrheliometer whose characteristics are well known. Another way that a calibration can be carried out is by using a substitution method. This requires that a standard source of radiation is present. The output of the reference instrument is compared to the output of the instrument that is to be calibrated. This method is, however, applicable only to instruments that possess the same spectral response [Uiso, 2004]. First class pyrheliometers are usually calibrated against the standard class of pyrheliometer and this is done during the IPC. The second class pyrheliometers, on the other hand, are calibrated against first class pyrheliometers.

2.8.5 The sun tracking system

For continuous measurements of direct solar radiation, pyrheliometers are mounted on a sun tracking system. There are different types of sun trackers. Earlier designs use a single-axis of rotation that is aligned parallel to the earth's axis of rotation. This type of sun tracker has a synchronous motor which is power driven, and it rotates 360° every 24 hours. The support platform of the pyrheliometer swings around the axis in an east-west direction. The platform can be adjusted according to the changing declination. Figure 2.13 shows a photograph of a single-axis tracking system, the Eppley Sun Tracker model ST-1 that has been used in this work.
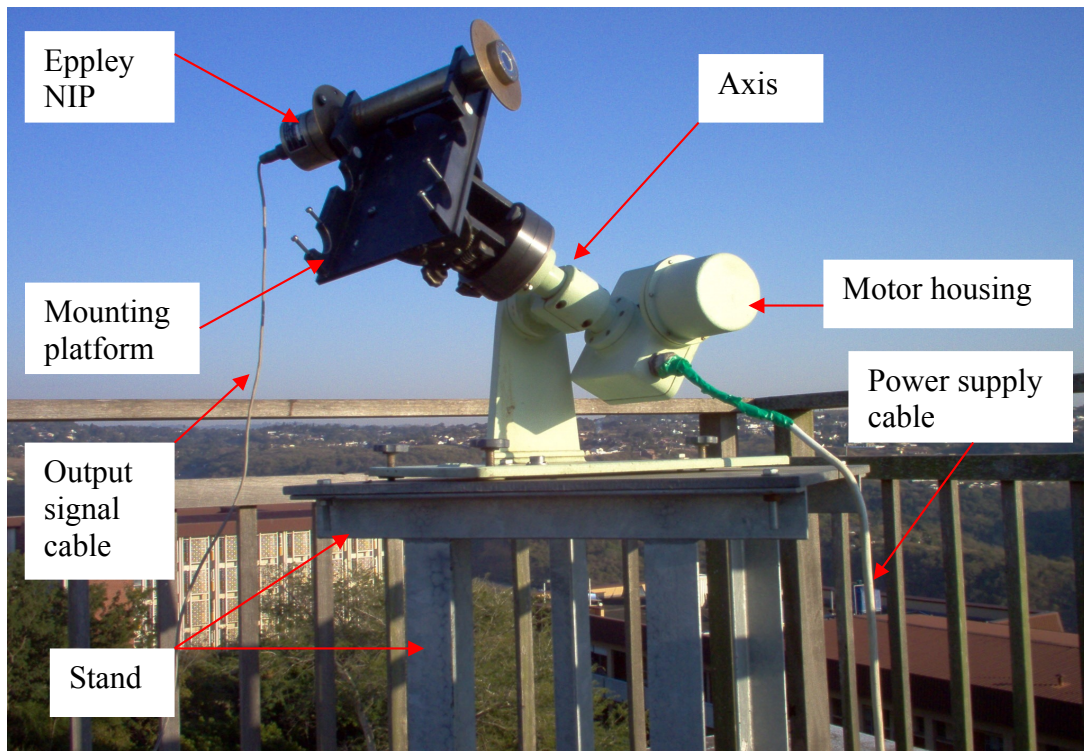
Figure 2.13: *The Eppley sun tracker model ST-1, with an Eppley NIP mounted to measure direct solar radiation.*

The connecting cable of the pyrheliometer turns around the axis of rotation as the tracker rotates, and gets entangled. The cable thus needs to be disconnected and reconnected after a complete rotation to avoid possible damage. Further to this, the pyrheliometer has to be aligned on a daily basis. This means that use of the sun tracker ST-1 requires that the pyrheliometer is supervised every few hours to ensure the accuracy of measurements. Due to the demand for supervision of the single-axis sun tracker, new types of sun tracking systems with double rotation using two stepping motors were developed. An
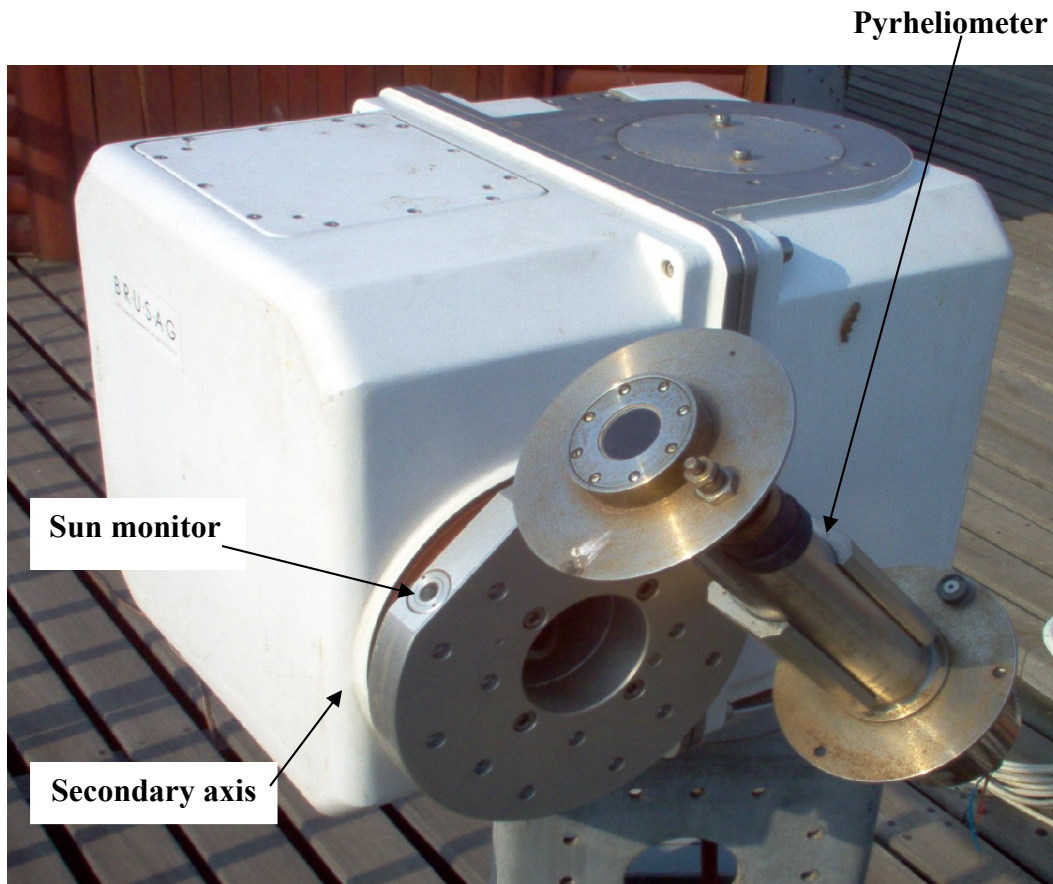
Figure 2.14: *The Brusag sun tracker, with a pyrheliometer mounted to measure direct solar radiation. The secondary axis moves in line with a change in the azimuth angle.*

example of a double-axis sun tracking system, the Brusag Sun Tracker which has been used in this work, is shown in Fig. 2.14.

The motors are controlled by a microprocessor which constantly calculates the sun's position. This type of sun tracker is designed to operate in a clock or sun mode and this allows the system to keep tracking even when the sun is completely obscured. As night falls, the moving part of the system retraces its path and stops at a position where it coincides with the position of sunrise. For the sun operating mode, a sun monitor is installed parallel to the pyrheliometer on the secondary axis. The sun monitor "sees" the sun as it is and this allows the microprocessor to align the system. These second generation of sun trackers provide a better accuracy than the single-axis tracking systems.

Despite the recognized accuracy of current commercially available direct solar radiation instruments, particularly the NIP, increasing costs are involved in the acquisition of these instruments. The tracking system also requires expensive technical demands in terms of maintenance and this leads to a reduction of solar radiation data at many locations in the world [Iziomon et al, 1999]. This situation is particularly predominant in areas where application needs may be plentiful.

2.9   Alternative approaches to DSR measurements

The demand for solar radiation systems is increasing and the need to know the amount of solar radiation available is important for proper planning and design of solar radiation systems. The lack of solar radiation data makes it difficult for proper planning and implementation of diverse solar radiation projects that would help to meet or at least to

supplement energy needs of many productivity sectors, with special emphasis on rural communities situated far from an electricity grid [van den Heetkamp, 2002]. As a solution, engineers and scientists have been adopting models that predict the collectable direct solar radiation for a given day at the location of interest. In this work, another approach is given that is concerned with direct measurement of solar radiation.

2.9.1   Direct solar radiation models

Several solar radiation models have been developed in different parts of the world to attempt to solve the scarcity of solar radiation data [Jacovides et al, 1996].

The techniques that have been used in solar radiation modeling are either statistical or physical. The statistical Ångström technique correlates sunshine duration and solar irradiance [Duffie and Beckman, 1991]. Another statistical technique correlates the incoming global solar irradiation with the earth's irradiance measured in the visible portion of the electromagnetic spectrum by satellite radiometers [Colle et al, 1999].

Figure 2.15 is an example of the results of solar radiation modeling [Twidell and Weir, 1996]. It depicts a variation of the solar irradiance throughout the year. The figure can be a useful guide to the average solar irradiance as a function of latitude and season. The physical method of modeling solar radiation is based on optical properties of the atmosphere such as absorbance, transmittance and reflectance. In this method changes in atmospheric air mass and cloud cover are considered.

Solar radiation models are based on historical data of incident radiation at the location in question or on data from an area with similar characteristics of weather and climate, which ideally must cover a number of years. This information is, however, rarely available [Jacovides et al, 1996].

A
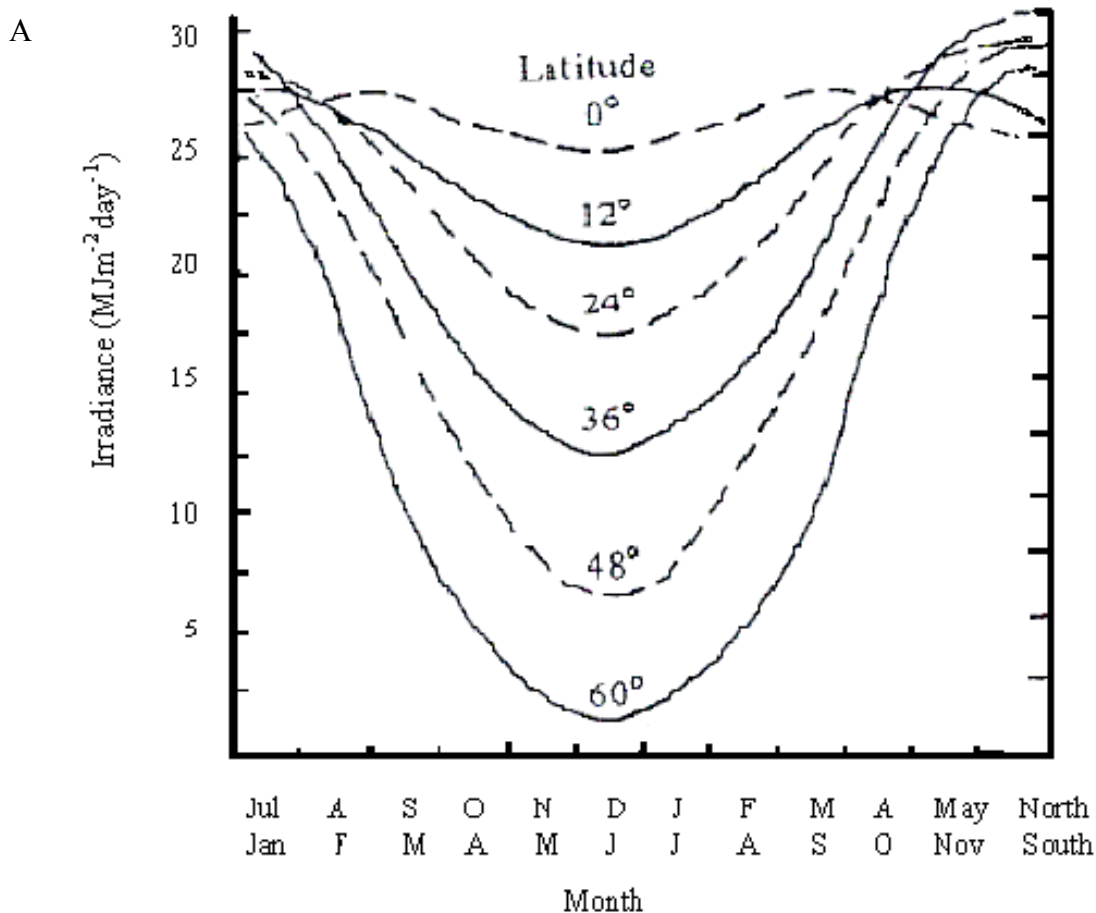
Figure 2.15: *The expected variation of the solar irradiance with latitude and season on a horizontal surface plane on a clear day [after Twidell and Weir, 1996].*

majority of meteorological authorities possess records of sunshine duration [Campbell Scientific, 1998]. The sunshine duration is measured using a Campbell-Stokes recorder. The recorder consists of a solid glass sphere and a piece of paper card behind it that is

graduated with a time scale synchronized to the movement of the sun. The solar beam becomes focused by the solid glass sphere such that it burns and carbonises the card leaving a trace. The length of the trace equates to sunshine duration [Duffie and Beckman, 1991].

2.9.2   The inefficiency of solar radiation models

Solar energy is the basic fuel for solar-based technologies [Myers, 2003]. An assessment of the efficiency and feasibility of these technologies requires solar radiation data, and where it is lacking, modeling is an alternative. However, these models are based on measured data, and frequently the uncertainty or accuracy of the data is not known [Myers, 2003]. As an example of this uncertainty, measurements of sunshine duration by the Campbell-Stokes recorder have some degrees of subjectivities mainly because the carbonization process is not efficient and may not occur when the card is wet. It is also a process that depends on the strength of the solar beam that strikes the solid glass sphere [Duffie and Beckman, 1991].

The accuracy and validation of any measured data depends on the calibration of radiometers. The calibration is based on the World Radiometric Reference (WRR) solar measurement scale and the overall uncertainty in the scale is 0.35 % [Myers, 2003]. Further to this, the calibration of radiometers comprises a series of comparisons with pyrheliometers that symbolise WRR with working reference cavity pyrheliometers that are used by calibration laboratories [Myers, 2003], and against which the on-field pyrheliometers are calibrated. This introduces a sequence of uncertainties in solar radiation models.

A large number of meteorological stations are often located at sites that are distant from solar radiation utilization and prospecting sites. This problem leads to a need for a development of interpolation models. These interpolation models may also transfer certain magnitudes of uncertainties to solar radiation models.

Statistical methods in general estimate solar radiation based on hourly, daily, monthly and yearly averages. This eliminates any fluctuations in solar radiation data that may be interrelated with changes in atmospheric conditions.

Predictions of direct solar irradiance are strongly affected by temporal and spatial factors such as air molecules, smoke and dust particles, atmospheric ozone, water vapor and carbon-dioxide. The order of fluctuations in these variables is somewhat difficult to predict, mainly because it is also related to different dynamic processes and factors that take place on the earth. Some of these factors arise from human activity.

Most physical models, even though they take into account many of these variables and are said to have a good accuracy, are often found to fail in some respects when applied to conditions in other locations [Iziomon et al, 1999]. This reveals a lack of uniformity and consistency in the variations of these variables from one site to another.

A complete record of past irradiance data can be used as an alternative to modeling, but this depends on the high technical and acquisition costs of industrially available solar

radiation instruments. These data are used to predict future irradiance, but only in a statistical sense. The most significant data for engineering purposes is the day-to-day fluctuations in irradiance as they affect the amount of energy storage that a solar energy system would require [Twidell and Weir, 1996].

Real-time data of solar radiation available on the ground requires a proper instrument that works continuously to give the behavior of solar radiation at every second. The availability of real-time data is very important for the control of the flow rate of heat transfer fluids in concentrating solar thermal systems. Quantum detectors seem to be a good option to overcome the scarcity of real-time data in that they are cheaper and so can be mass-produced. Thus, a large number of them will reduce the propagation of uncertainties.

2.10   Basic principles of quantum detectors

Quantum detectors are constructed from semiconductor materials. Amongst the elements, silicon (Si) and germanium (Ge) are of great importance in the fabrication of semiconductor devices. These two elements are characterized by having four valence electrons in a covalent bond.

The Silicon semiconductor has a low electron mobility to give a low drift velocity and is very manageable, principally because its doping properties are good [McPherson, 1997]. Some of the properties of silicon and germanium are shown in Table 2.3.

Table 2.3: *Properties of pure silicon and germanium [compiled from different authors cited in the text]*

	Silicon	Germanium
Atomic number, Z	14	32
Atomic mass, M	28.1 amu	72.6 amu
Density, ρ	2330 kg m^{-3}	5320 kg m^{-3}
Energy gap, E_G at 300 K	1.12 eV	0.72 eV
Electron mobility, μ_e at 300 K	0.135 m^2 s^{-1}V^{-1}	0.39 m^2 s^{-1}V^{-1}
Hole mobility, μ_h at 300 K	0.048 m^2 s^{-1}V^{-1}	0.19 m^2 s^{-1}V^{-1}
Intrinsic resistivity at 300 K	2300 Ω m	0.46 Ω m

Conduction in semiconductors is due to two charged particles of opposite sign, moving in opposite directions when under the influence of an electric field. For a pure (or intrinsic) semiconductor, it is required that electrons in the valence band acquire a certain amount of energy to be able to move from the valence band to the conduction band. This energy must exceed the energy difference between the top of the valence band and the bottom of the conduction band, the so called band gap of width given by

$$E_G = E_C - E_V \qquad\qquad (2.12)$$

where E_G is the width of the energy band gap, E_C is the energy level at the bottom of the conduction band and E_V is the energy level at the top of the valence band.

When an electron leaves the valence band to enter the conduction band a vacancy (or hole) is created in the valence band [Close and Yarwood, 1976]. The region in which this vacancy exists has a net positive charge. These electrons and holes are the particles that are responsible for conduction in a semiconductor. Electrons in a semiconductor can be exited by bombardment with external particles such as photons or by thermal effects.

2.10.1 Incidence of a photon onto a semiconductor

For an incident photon to cause a movement of an electron from the valence band towards the conduction band, it is necessary that the photonic energy exceeds the energy of the band gap. This means that this process is a function of the wavelength, λ of the incident photon since

$$E = h\nu = \frac{hc}{\lambda} \tag{2.13}$$

where h is Planck's constant, ν is the frequency of the incident photon, c is the speed of the photon and λ is the wavelength of this photon.

For intrinsic silicon, where E_G=1.12 eV at 300 K, the maximum wavelength for detection of radiation, λ_{max} is equal to 1109 nm which is situated in the infrared region. Photons of lower wavelength, especially in the visible region (~380 nm to ~780 nm) of the electromagnetic spectrum, are thus able to generate free electrons in a silicon semiconductor.

In general a pure semiconductor exhibits poor conductivity [Smith, 1983]. To increase the conductivity of a semiconductor two methods are used. The first is related to the fact that the concentration of free carriers increases exponentially with temperature, while the second involves adding small quantities of selected elements (or impurities) to the semiconductor.

2.10.2 Current flow

The two factors that contribute to the movement of electrons (or holes) in a semiconductor result in current flow. The first factor is the difference in the concentration (or density) of the electrons and holes (or current carriers) throughout the semiconductor. This difference in density will generate a diffusion of carriers towards the region of the semiconductor with a low density of carriers. The current generated is called a *diffusion current* [Sze, 1969]. For a flux in one dimension, the diffusion current density due to electrons and holes is given [Smith, 1983] by

$$J_d = \left(D_n \frac{dn}{dx} + D_p \frac{dp}{dx} \right) e \tag{2.14}$$

where, J_d is the diffusion current density, e is the charge of each diffusive particle, D_n is the diffusion constant for electrons, D_p is the diffusion constant for holes, $\frac{dn}{dx}$ and $\frac{dp}{dx}$ are the concentration gradients of electrons and holes respectively, p is the number of holes and n is the number of electrons.

The diffusion of charged particles is a statistical phenomenon and not due to any external influences [Smith, 1983]. The mobility of a charged particle in an electric field and the diffusion constant are both related by the Einstein equation

$$\frac{\mu}{D} = \frac{e}{kT} \tag{2.15}$$

where μ is the mobility of the charged particles, D is the diffusion constant, k is the Boltzman constant and T is the absolute temperature.

The current carriers will move due to an induced electric field and the current generated is designated *drift current* [Smith, 1983]. The drift current density is given by

$$J_D = \left(n\mu_n + p\mu_p \right) e\varepsilon = \sigma \varepsilon \tag{2.16}$$

where σ is the electrical conductivity of the semiconductor material, μ_n is the mobility of electrons, μ_p is the mobility of holes and ε is the electric field. The total current density in the x-direction is then given as

$$J = \sigma\varepsilon + \left(D_n \frac{dn}{dx} + D_p \frac{dp}{dx} \right) e \tag{2.17}$$

the sum of the diffusion current and the drift current.

The speed at which a semiconductor device can respond to changes of an external excitation depend on the process of rearrangement of electrons and holes in order to re-establish equilibrium after the exciting effect has ceased. The time between the perturbation and the return to equilibrium is called the life-time of the current carriers [Sze, 1969].

2.10.3 The *p-n* junction behavior

The *p-n* junction is a combination of an *n*-type semiconductor material and a *p*-type one. For Si (or Ge) an *n*-type semiconductor is obtained by adding a small quantity of pentavalent atoms in intrinsic Si (or Ge) while a *p*-type semiconductor results from the addition of a trivalent atom.

When a *p*-type semiconductor is brought into contact with an *n*-type semiconductor within a single crystal, a depletion region is formed near the *p-n* junction. Within this depletion region there are no free carriers. However, at a temperature of 300 K thermal agitation or vibration of atoms occurs in a crystal and this will produce a few charge carriers when electrons acquire sufficient energy to break the covalent bond. This gives rise to the formation of electron-hole (*e-h*) pairs in a continuous process. The higher the temperature the greater the rate at which generation and recombination of *e-h* pairs occurs [Hughes, 1995].

Under open-circuit conditions, there is no voltage applied across the *p-n* junction and no current flows in the external circuit. However, across the junction there are two equal currents flowing in opposite directions [Close and Yarwood, 1976]. The reason is that the separation of charged particles due to diffusion generates an electric field in the semiconductor which will act to oppose the diffusion of current carriers [Close and Yarwood, 1976].

When a voltage is applied across the junction current flow occurs. This current is a result of electrons moving from the *n*-type part of the semiconductor to enter the *p*-type part. Holes move in the opposite direction. The current is defined in general [Streetman, 1990] as

$$I = I_s \left[\exp\left(\frac{eV}{\eta kT} \right) - 1 \right] \tag{2.18}$$

where I_s is the reverse saturation current, V is the voltage applied across the junction and η is a constant which characterises the device. The value of η varies from ~1 when a

diffusion current dominates to ~2 when the bulk recombination current is dominating [Sze, 1969].

The junction is at reverse bias (RB) when the positive terminal of the source of voltage is connected to the *n* side of the junction and the negative terminal is connected to the *p* side as in Fig. 2.15.
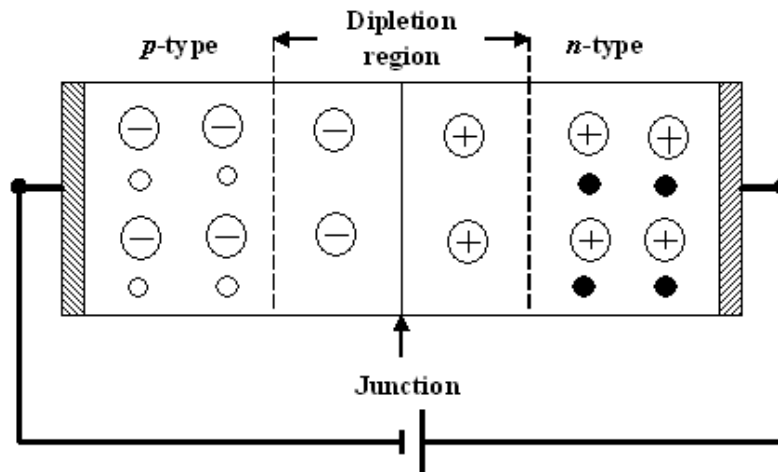
Figure 2.15: *A schematic representation of a p-n junction. The polarity of the voltage source is reversed with respect to the p-n junction. The ● represents an electron and the ○ a hole.*

In reverse bias a small current flows across the junction because applying a voltage in reverse increases the potential barrier to inhibit movement of majority carriers (electrons from *n* to *p* and holes from *p* to *n*). The width of the depletion region increases with an increase in reverse bias [McPherson et al, 1997]. Current flow through the junction results from a few electrons that are thermally generated in the *p*-type material and a few holes generated in the *n*-type material. This current is called *reverse saturation current* defined in Eq. (2.18) and is largely independent of the voltage [McPherson, 2004]. Reverse saturation current will increase with increasing temperature. A low value of

reverse saturation current is one of the advantages of silicon over germanium [Smith, 1983]

The junction is at forward bias (FB) when the positive terminal of the external voltage source is connected to the *p* side of the junction as shown in Fig. 2.16.
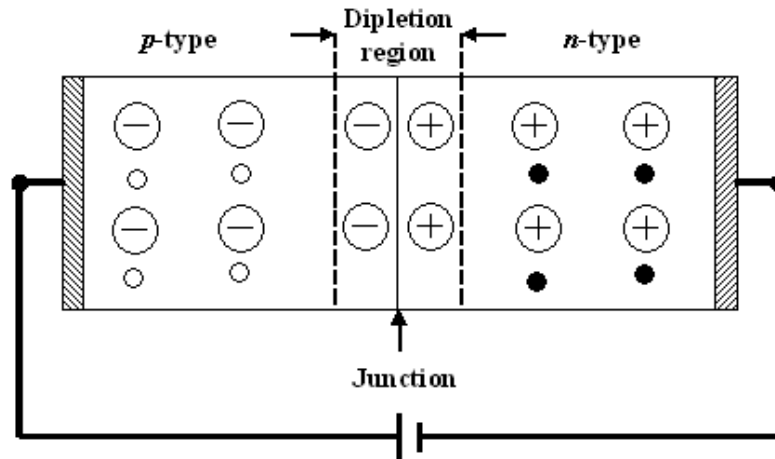

Figure 2.16: *A schematic representation of a p-n junction. The polarity of the voltage source is made forward with respect to the p-n junction. The ● represents the electron and the ○ a hole.*

A consequence of forward biasing the *p-n* junction is a reduction of the potential barrier and the depletion region width. The probability of majority carriers possessing the required energy to cross the barrier is greatly increased [Smith, 1983] with the result that there is large current flow for very small voltages. In this way a *p-n* junction acts as a rectifier in that it allows current flow in FB and none at all in RB.

There are three capacitive effects associated with the *p-n* junction of a semiconductor and each of these is related to the type of voltage applied. These are the depletion region capacitance, C_T, the diffusion capacitance, C_D and the dynamic diffusion capacitance, C_d

[Close and Yarwood, 1976]. The depletion region capacitance occurs at reverse bias. Since the width of the depletion region increases with reverse bias, the number of stationary charges in this region is increased. Thus,

$$C_{\mathrm{T}} = \frac{\mathrm{d}Q}{\mathrm{d}V} \qquad (2.19)$$

where $\mathrm{d}Q$ is the fixed charge variation and $\mathrm{d}V$ is the change in voltage. The charge variation in a time interval $\mathrm{d}t$ is given by

$$I = \frac{\mathrm{d}Q}{\mathrm{d}t} = C_{\mathrm{T}} \frac{\mathrm{d}V}{\mathrm{d}t} \qquad (2.20)$$

and is the current I.

The *diffusion capacitance*, is associated with forward bias. This capacitance results from the injected charges that are stored in the vicinity of the junction. There have been occurrences of negative capacitance in some radiation-damaged *p-n* junctions [McPherson, 2002]. The *dynamic diffusion capacitance* occurs when the applied forward voltage varies with time.

2.10.4 Detection of radiation

When radiation impinges on a *p-n* junction of a semiconductor, and the incident radiation has energy that exceeds the energy gap of the semiconductor, *e-h* pairs are generated. The number of *e-h* pairs produced will be determined by the amount of energy that the incident radiation possesses which is itself a function of the wavelength [Close and Yarwood, 1976]. At reverse bias, the minority carriers generated by the radiation will

flow through the junction as a result of the electric field, and a current proportional to the intensity of the incident radiation will be measured [Hughes, 1995].

An advantage of operating a *p-n* junction at reverse bias in radiation detection is that leakage currents that are due to thermal agitation at room temperature can be reduced. This is because the semiconductor attains a wide band gap and the probability that the majority of current carriers will possess sufficient energy to traverse the band gap diminishes. It is a requirement that substrate material used for the fabrication of radiation detectors is of a high atomic number to ensure a high stopping power [McPherson, 1997].

Semiconductor detectors are of small size, operate at high speed and their thickness can be tailored to suit almost any application requirements. The short time constant that characterizes them, makes semiconductor detectors ideal for measurement of events that highly fluctuate with time such as direct solar radiation.

The electrical characteristics of a semiconductor detector may be altered by the incident radiation that it is intended to detect, an effect referred to as radiation-induced damage [McPherson, 1997]. This constitutes a main disadvantage of these detectors. Another disadvantage is the dependence of the spectral response of the detectors on the wavelength of the incident radiation [Duffie and Beckman, 1991]. Figure 2.17 illustrates a variation of the relative sensitivity of a silicon photodiode with wavelength.
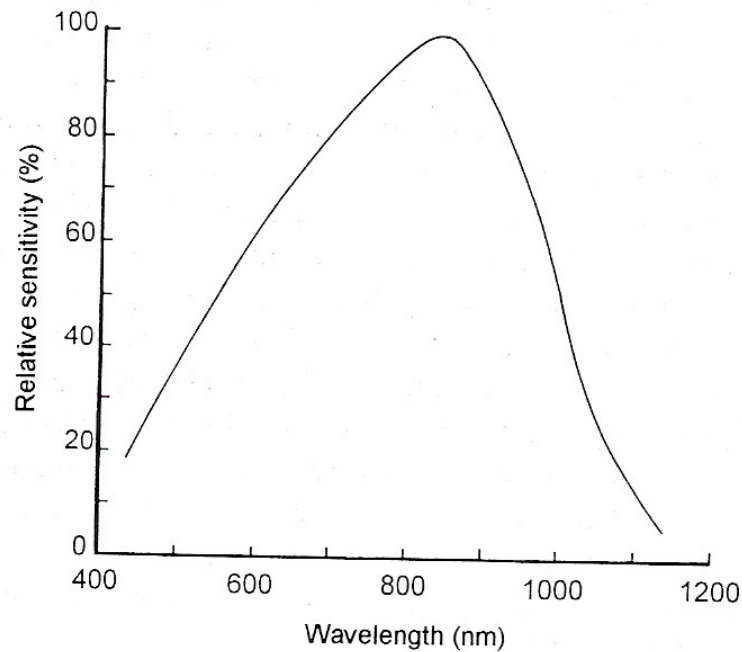
Figure 2.17: *A variation of the relative sensitivity of a silicon photodiode with the wavelength of the incident radiation [after Guyot, 1998].*

2.11 Optical glass filters

Optical filters are often used to correct the spectral response of semiconductor detectors because they can attenuate or block certain wavelengths of radiation or enhance the spectral sensitivity of the detector and hence produce an overall desired detector response [Ryer, 1998]. The overall responsivity of a semiconductor detector is equal to the product of the responsivity of the sensor and the transmission of the filter. Because of this, an ideal filter transmission curve can be obtained only if a desired overall sensitivity is given and the responsivity of the detector is known.

The spectral transmission of a filter varies logarithmically with respect to filter thickness. In other words, the filter's bandwidth decreases with the filter thickness and this is known as Bouger's law [Ryer, 1998]. The spectral responsivity of a semiconductor detector can be modified by varying the thickness of the filter to match a selected or desired function. Equation (2.21) represents a description of the effect of thickness on transmission the Bouger's law in mathematical form given as

$$\frac{\log \tau_{i1}}{d_1} = \frac{\log \tau_{i2}}{d_2} \tag{2.21}$$

where τ_{i1} and τ_{i2} represent the internal transmittances of the two filters involved, and d_1 and d_2 are the thicknesses of the filters in question. Here, τ_{i1} and τ_{i2} are defined as the fraction of incident irradiance transmitted through the filters. The relation of Eq. (2.21) applies only to two filters that are made from the same material.

When light passes through two mediums of different indices of refraction, a certain amount of reflection losses must be expected. Due to these losses, the internal transmittance is greater than the external transmittance [Ryer, 1998]. In accordance with Fresnal's law, reflection losses can be quantified by

$$r = \frac{(n-1)^2}{(n+1)^2} \tag{2.22}$$

where r is the reflection losses index of the filter and n is the ratio of the refractive indices.

There are two groups of filters and these are distinguished by their construction and principle of operation. The first group is the interference filter, which is based on a

harmonic interference between waves to provide very narrow pass bands. These filters are capable of bandwidths less than 10 nm. An interference filter consists of thin metallic layer films spaced half the desired wavelength apart by a dielectric spacer [Website 7]. The other group of filters is the absorptive filters, and these are based on the absorption of a particular bandwidth. This type of filter consists of glass that has been doped with a certain amount of dye that absorbs particular colours only [Website 7].

Filters may also be classified according to the spectral bandwidth of interest into flat response, photonic, broadband colour, neutral density, narrow band, wide band optical and sharp cut filters. The sharp cut filters, flat response filters and the broadband filters constitute the group of filters that are assumed to be ideal in this project. Sharp cut filters are frequently used to filter out radiation of long wavelength [Ryer, 1998]. The flat response filters can be used to tailor the spectral response of a detector such that its response to solar radiation is uniform; that is, for the same amount of irradiance, the instrument will have an equal response and this is independent of wavelength. The broadband filters are used to pass a broad band of light and this blocks any unwanted spectrum ranges.

Rapid changes in temperature are known as thermal shock and the effect can cause changes in the filter properties [Website 7]. Exposure to high humidity or corrosive environments can produce spotting or straining. This alters the surface properties of the filter and results in an increased scattering of radiation on its surface, thus decreasing the transmission through the filter [Website 7].

2.12   Description of the DSRD and its circuit

The DSRD is an instrument designed to measure direct solar radiation. This instrument was developed for gathering solar radiation data cheaply and on a real time basis. It was also designed as a user friendly detector. It detects radiation by using the quantum detection principle which, as mentioned earlier, is based on the direct conversion of solar radiation into an electrical signal. The DSRD is made up of an integrated circuit (IC) and an external circuit (EC), both of which are housed in a black, rectangular and rigid plastic box. Holes for collimation of the solar beam, for the power supply lead and for feeding the electrical signal to the data logger have been drilled on the box.

The IC is an OPT101 monolithic combination of a photodiode and an amplifier. The noise performance of the IC depends on several factors. These are the bandwidth on which the amplifier operates, the feedback resistance, the feedback capacitance and the capacitance of the photodiode. The advantage of a monolithic combination is the high possibility of elimination of leakage current errors, noise pick-up and gain peaking due to stray capacitance [Burr-Brown, 1996]. The time constant of the IC is $RC = 0.71\,\mu s$, which is the time in which the IC responds to changes in the measured effect.

The photodiode constitutes the sensing element of the DSRD and has an active area of ~5.22 mm^2. It is operated in the photoconductive mode. In this mode, it coverts the solar energy falling onto it into an electrical current which is proportional to the amount of

solar radiation absorbed. In general, photodiodes respond strongly to the radiation at near infrared, and this makes thermal noise in such diodes an effect to be strongly taken into account.

The amplifier operates as an integrating amplifier and is an inverting operational amplifier. It is connected onto the IC such that the current flowing from the photodiode is converted into a voltage which is the output. Thus, the DSRD signal can be read directly by a data logger. Fig. 2.18 shows a photograph of the integrated circuit in DSRD.
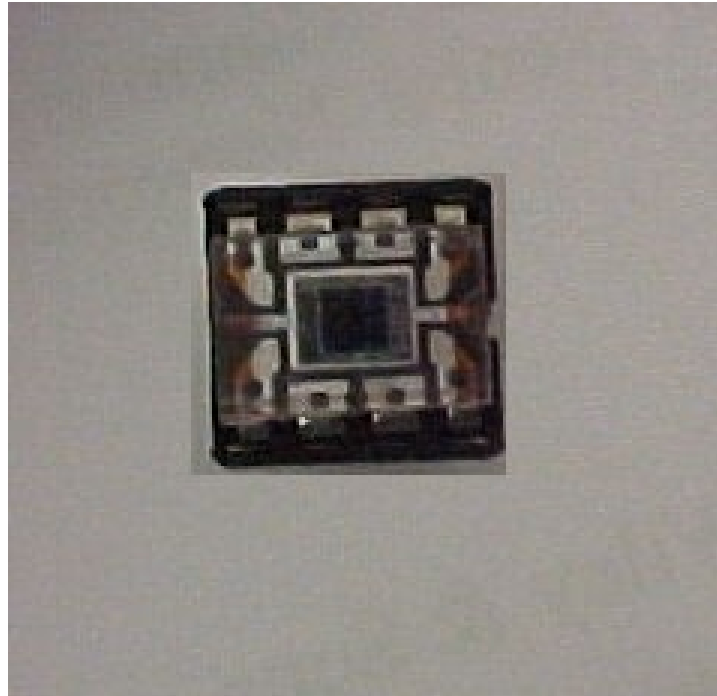
The EC consists of a variable resistor, a battery and a toggle switch. The variable resistor

Figure 2.18: *A photograph showing the photodiode in the centre on the integrated circuit of the OPT101 used in the DSRD.*

is introduced to adjust amplification of the signal and also to vary the time constant. The battery is used for voltage supply to the entire circuit of the DSRD. The switch allows either the battery or the power supply to be used in accordance with the voltage source

used to bias the detector.   A schematic diagram of the DSRD circuit is shown in Fig.
2.19.
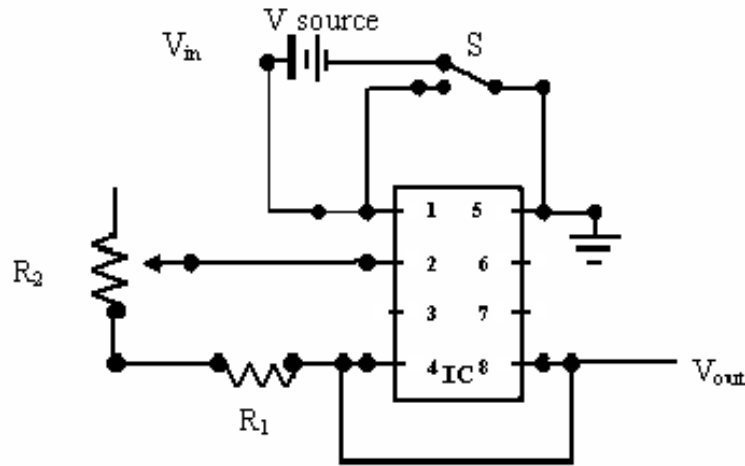
Figure 2.19: *A schematic diagram of the DSRD circuit. Here, R_2 is the variable resistor which allows for adjustment of the sensitivity of the detector.*

The bias voltage supplied to the DSRD is represented by V_{in} which is supplied to the OPT101 through pin 1. The output voltage, V_{out}, is a measure of the amount of solar energy received on the detecting surface of the OPT101 and is obtained through pin 8. The resistor R_2 is a variable resistor which allows for adjustments of the sensitivity and the time response of the detector.

Chapter 3

3. Experimental Methods

Several preliminary measurements were carried out in order to characterize the DSRD and thereafter, the investigation focused on possible ways of improving the detector. A new DSRD was built to incorporate the improvements. This new detector was designated DSRD2 and the old one DSRD1. All subsequent measurements were carried out on detector DSRD2. The detecting diode and electronics of the two detectors are the same.

3.1   Characterization of detector DSRD1

The characterization of detector DSRD1 was based on the spectral response, the angular or polar response and the environmental stability of the detector. By characterizing the spectral response, it was intended to investigate how the detector tracks the variation of direct solar radiation early in the morning and late in the afternoon. The reason for this investigation is related to the fact that the detection principle of the sensor OPT 101 is based on the wavelength of radiation. In general, the sensitivity of the sensor to radiation is more pronounced in the IR region. This suggests that the detector will respond to direct solar radiation unevenly especially when IR radiation is predominant. It is preferred that the detector responds according to the amount of energy absorbed. By polar response characterization, it was intended to investigate how the detector responds when it is not properly aligned with respect to the normal of incidence. This is facilitated by the fact that the maximum intensity of direct solar radiation is obtained when the incident solar

beam is perpendicular to the collecting surface. Here, the size of the aperture through which the detector sees the sun plays an important role by preventing the detector from picking up unwanted radiation. By characterizing the environmental stability of the detector, it was intended to investigate how the detector would stand up to variations in meteorological conditions like temperature, rain, moisture and humidity.

3.1.1   Spectral response

Detector DSRD1 is designed to detect solar radiation in the wavelength range between 320 and 1100 nm. The characteristic spectral response of the OPT101 sensor (shown in Fig. 3.1) indicates that the responsivity of the detector is more pronounced in the IR region, with a peak at 850 nm. This means that the detector will indicate a high output when IR radiation is predominant. In order words, the output of detector DSRD1 will increase as the sun goes lower and lower in the sky, taking into account the attenuation of the solar beam discussed in Sections 2.2 and 2.3. Another contributing factor to the increased output is the significant emission of IR radiation by the earth and any objects on its surface during the time when the sun sets. This enhances the predominance of the IR radiation in the sky and hence increases the readings of the detector.

A change of the detector response according to the wavelength of the absorbed radiation is a common and well-known characteristic in photodetectors. Figure 3.1 shows the spectral response of the DSRD1 detector.
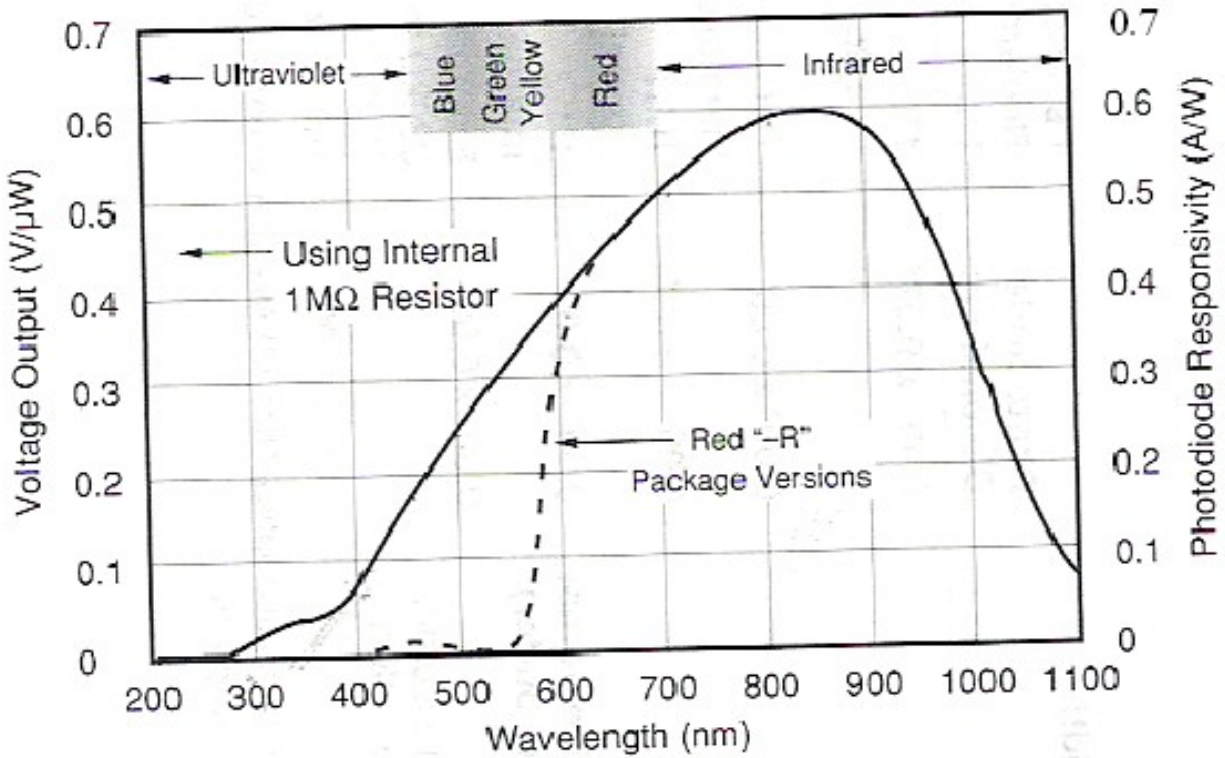
Figure 3.1: *A spectral response of the OPT101 sensor which shows a peak at ~ 850 nm indicating that the detector is more sensitive at this wavelength [after Burr-Brown, 1996].*

In an attempt to improve the detector, two different filters were tested on it and these are a blue optical glass filter (BG39) and the optical glass filter (KG). It was intended to test both filters to determine which of the two produced a better overall response in combination with the DSRD1 detector. The blue colour of the optical glass filter is to enhance the transmission of ultraviolet radiation. The filters were chosen by taking into account their characteristics, the solar radiation spectrum, the distribution of solar energy along the solar spectrum and the attenuation of solar radiation by atmospheric contents.

68

The BG39 filter is a bandpass Schott filter that allows transmission of radiation only in the range between ~320 nm and ~700 nm with a peak at about 500 nm. Figure 3.2 illustrates its transmission curve with respect to solar radiation.
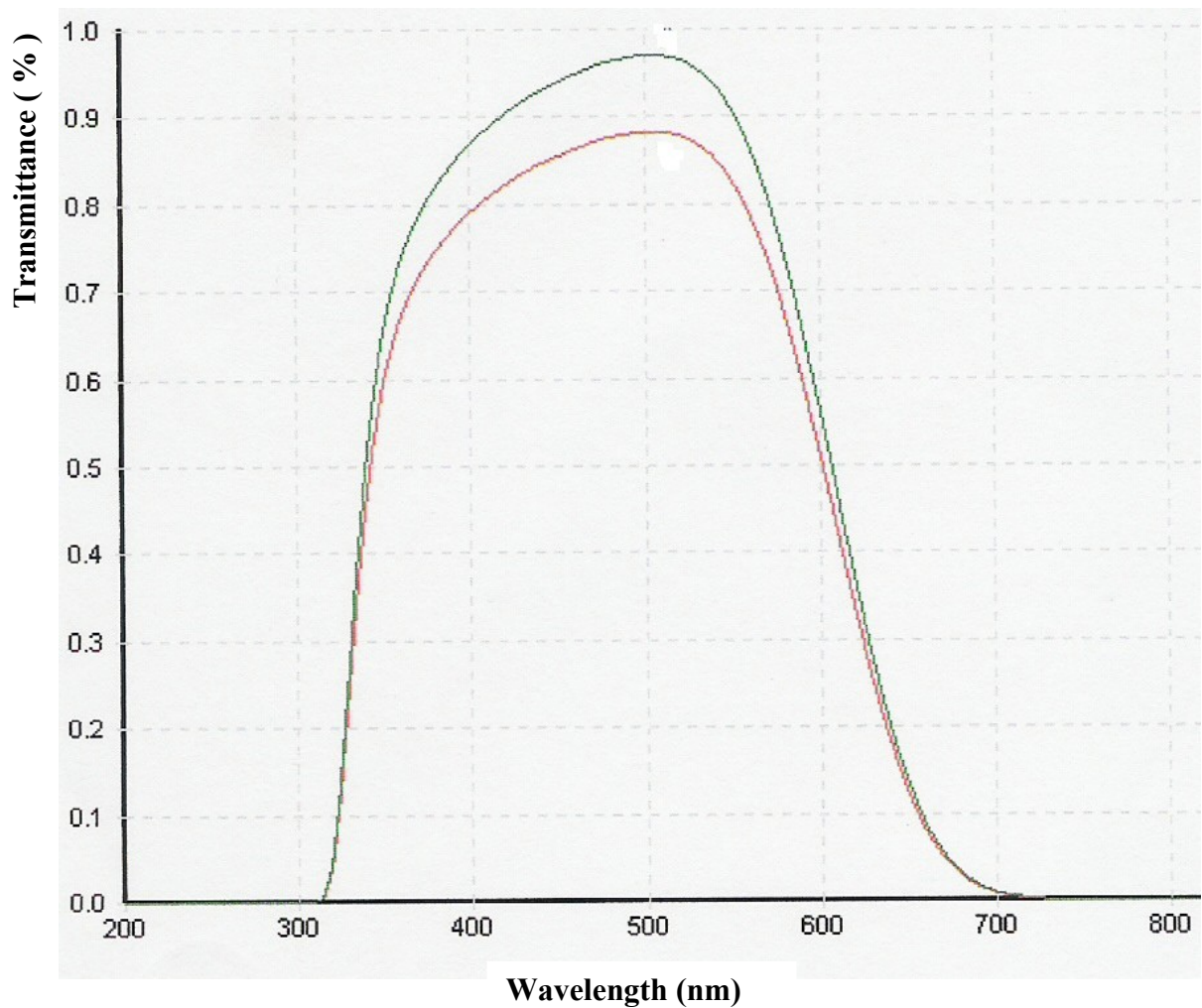
Figure3.2: *The transmission curve of the Schott optical glass filter BG39 which was tested for its applicability for modification of the spectral response of the DSRD1 detector.*

In the spectral transmission curve shown in Fig.3.2, the green line represents the internal transmittance and the red line the external transmittance. The thickness of the filter is d (= 1 mm) and the reflection factor is P (= 0.91). The overall spectral response of the detector representing combination of spectral responsivity of the sensor and the schott glass filter BG39 is shown in Fig.3.3.
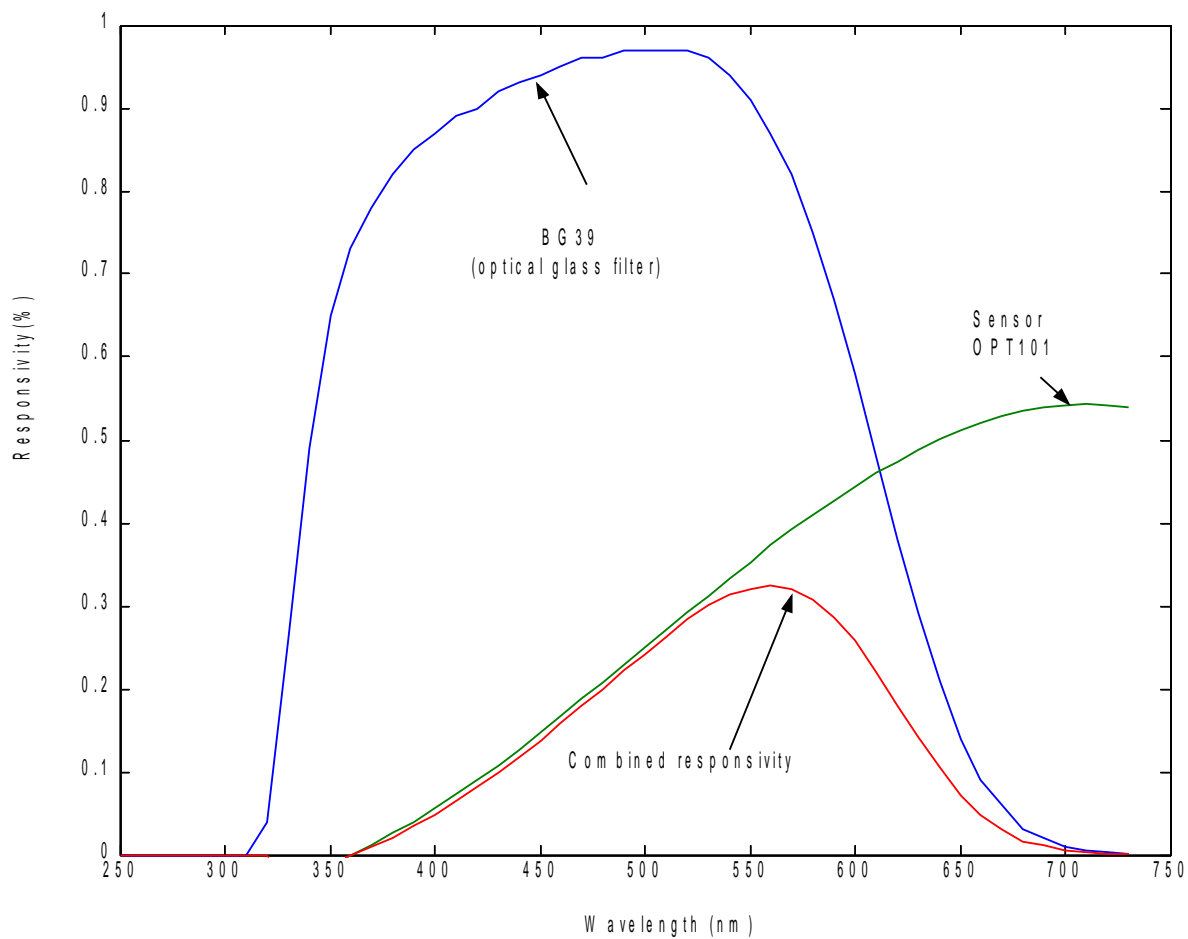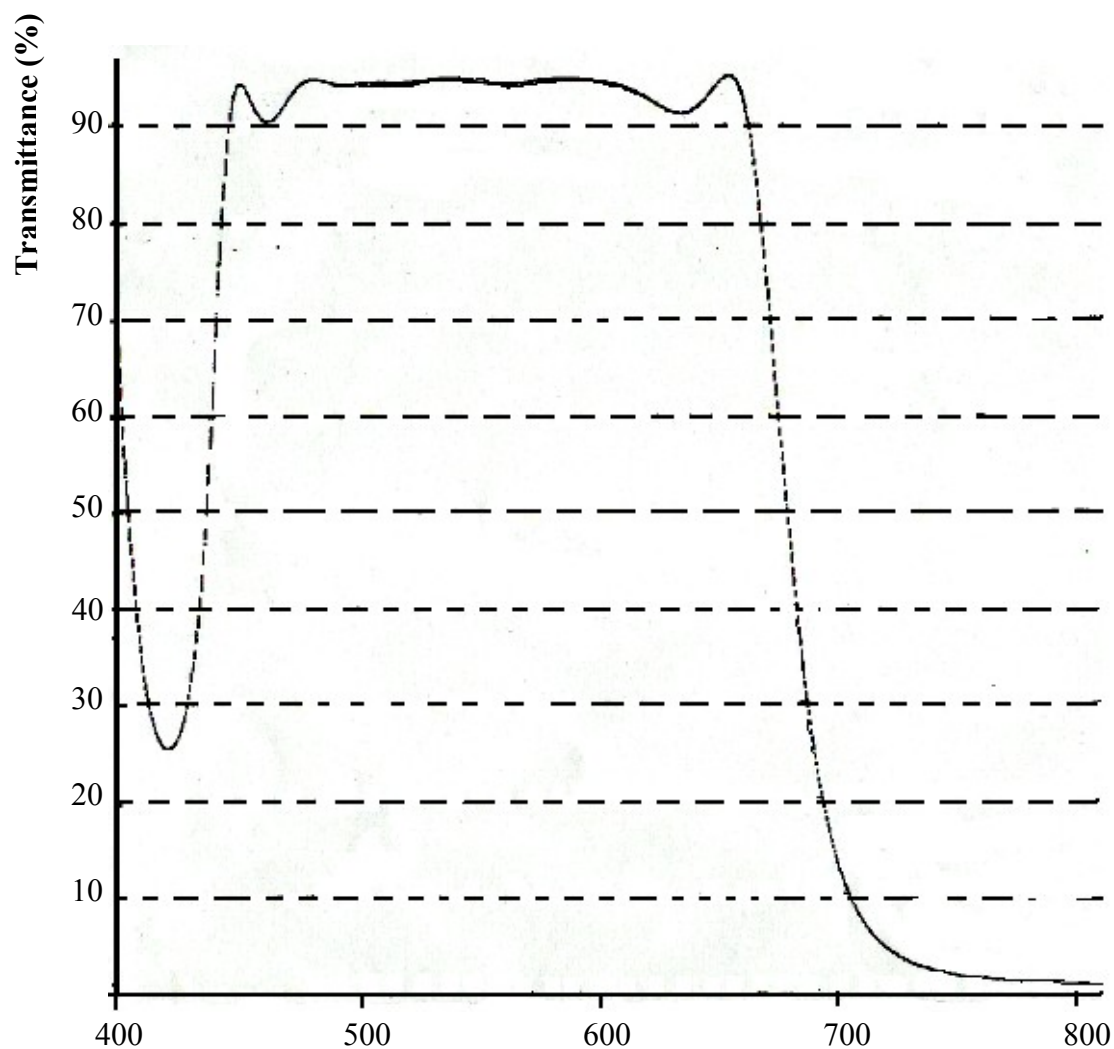

Figure 3.3: *The overall spectral response of the OPT101 sensor and the optical glass filter BG39. The combined responsivity is shifted to a wavelength of ~550 nm as shown by the red curve.*

Figure 3.3 suggests that the DSRD1 coupled to the BG39 filter will detect direct solar radiation between the wavelength range of ~350 nm and ~700 nm. In other words, the overall responsivity of the detector combined with BG39 filter will be given by the area under the red curve in Fig. 3.3. Another aspect that can be noted from the figure is related to the shift towards a wavelength of ~550 nm. Thus, detector DSRD1 in the situation of Fig. 3.3 will be less sensitive to solar radiation in the IR region and therefore good for this research work.

It is vital to underline the fact that the most important part of the solar radiation spectrum for this project is the visible region, and this is because a major portion of the energy that reaches the earth's surface is situated in this region. Radiation in the IR region has an input but in a small proportion compared to radiation in the visible region since a major part of solar energy in the IR region is strongly absorbed by water vapor and carbon dioxide as discussed in Section 2.1. Besides this, IR radiation is also radiated by any object at ambient temperature and it is desired that the detector measures only direct solar radiation.

The KG filter is a broadband Schott optical glass filter which transmits radiation between the wavelength ranges of ~400 nm and ~800 nm. The spectral transmission curve of the KG filter is shown in the scan of Fig.3.4 and shows a peak plateau from about 450 nm to 660 nm.

Figure 3.4: An *illustration of* the **Wavelength (nm)** *ce curve of the KG filter showing a peak plateau from about 450 nm to 660 nm (reproduced from Optocon.).*

This filter is almost uniformly transparent in the visible region of the SRS but is opaque to UV and IR radiation. It should therefore be ideal for correction of the spectral response of the DSRD1 detector. A combination of the spectral responsivity of the DSRD1 detector and the KG filter is shown in Fig. 3.5, and indicates a combined responsivity at a wavelength of about 650 nm (red curve).
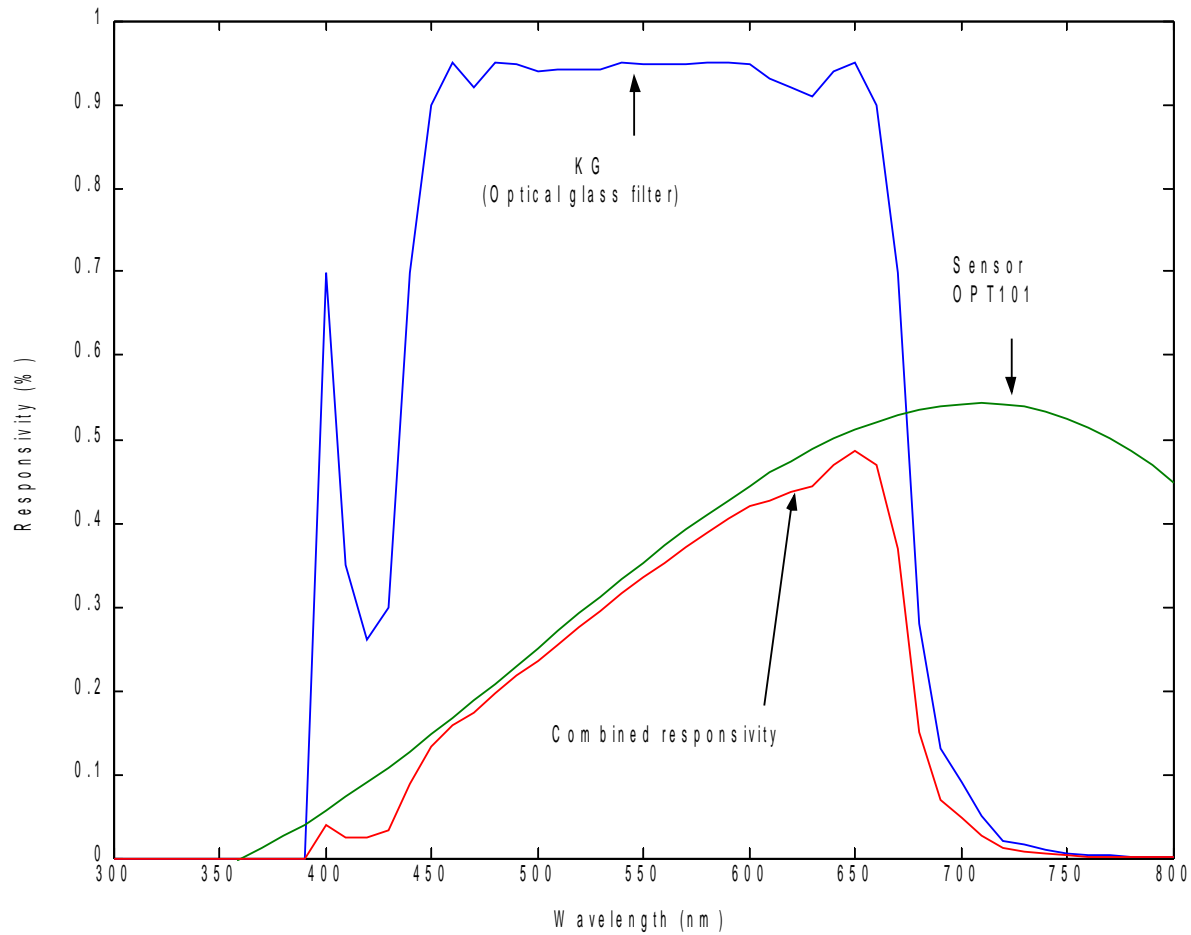
Figure 3**.5:** *The overall responsivity of a combination of the OPT101 sensor and the optical glass filter KG. The figure indicates a resultant peak responsivity at ~650 nm as   by the red curve.*

A comparison of Fig. 3.3 and Fig. 3.5 shows that, a combination of the OPT101 sensor and the BG39 filter produces a responsivity area that is smaller than a combination of the OPT101 sensor and the KG filter. This would seem to imply that the best combination of filter and detector is achieved between the OPT101 sensor and the KG filter.

3.1.2 Polar (Angular) response

The response of the DSRD1 detector with respect to the angle of incidence of the solar beam is very important for an assessment of the collimation. The solar beam is collimated in order to restrict the detection of different and unwanted wavelengths. The collimating hole is of a diameter of 1 mm and is 10 mm long. The dimensions offer a full angle field of view of about 5.2°. The full angle field of view is an angular aperture from which the detecting surface sees the sun.

For detector DSRD1 the full angle field of view was chosen by taking into account the fact that the detector is needed to provide a signal from which the flow rate of a heat exchange fluid of a solar thermal energy system can be controlled online. It is also needed to determine the saturation value of the detector for dimensions that give a full angle field of view bigger than 5.2°. If direct solar radiation is measured without any consideration of the variation of atmospheric conditions, the full angle field of view is found to vary from ~ 8° to ~15°. In the design of solar energy storage systems, it is ideal to have a full angle field of view ranging between 5° and 6°.

In general, an aperture that has a full angle field of view below 4° is not practical for general meteorological network purposes. On the other hand, an aperture with a full angle field of view greater than 8° enables an instrument to measure, in addition to direct solar radiation, radiation from the aureole. Under ordinary conditions counts ranging between 1.5 and 7.0 percent of the direct solar radiation are possible [Ångström and Rodhe, 1996].

It has been shown [Ångström and Rodhe, 1996] that if it is desired to attain an accuracy greater than that corresponding to 1.5 percent in the measurements by pyrheliometers of common construction, full consideration must be given to the aperture of the instrument and to the turbid conditions of the atmosphere.

3.1.3   Environmental stability

The test for environmental stability is intended to measure the ability of the detector to withstand changes in ambient temperature, in precipitation, in humidity and in dust content. A black perspex block 10 mm thick and with a collimating hole was placed in front of the box. The perspex was placed such that the solar beam could be focused through the hole to the detecting surface which is just a simple p-i-n diode.

The housing of the DSRD1 is black and is made of plastic, factors that are significant contributors to the amount of heat absorbed. The absorbed heat should lead to an increase in temperature within the housing and surroundings of the detector. The rise in temperature causes an increase in the measured current [McPherson, 2004[a]] in such p-i-n diodes. A temperature sensor was incorporated in the housing of the DSRD2 detector to investigate the effect of temperature changes on the measured current. The black perspex box was replaced with a white perspex box to reduce possibilities of heat absorption. It is possible that the effects of heat absorption may only be observed over a long-term, so that the replacement of the black box with a white was assumed as a long term preventive measure.

The housing of the detector was not well sealed and this could cause damage to the detector by accumulation of moisture and dust onto the detecting surface. Further, unwanted radiation may be detected through these unsealed points, thereby distorting detector readings. A properly sealed housing is expected to prevent negative performance of the detector and to provide long-term durability.

Another improvement on the detector was to use an insulated terminal to connect the cables that feed the signal to the data logger and the voltage to the detector. The DSRD1 was built such that either a battery or an external power supply could be used. A toggle switch was incorporated to switch either the battery on or the external power supply on. The connectors and the toggle switch were, however, not water-proof and not at all suited for corrosive environments. In DSRD2 a sealed connector was used which holds 6 pins through which signals can be passed.

The filter was placed in such a way that besides filtering solar radiation it could also act to block moisture and dust from accumulating in the collimating hole. In these ways, the interior of the housing could be assumed completely sealed from the outside and also assumed to be at a temperature tolerable to the detecting surface. Figure 3.6 is a photograph of the DSRD1 and the DSRD2 showing various improvements carried out on the DSRD1.

(a)

Terminal connectors for the output signal and to supply voltage

The sight element

Collimating hole

Power switch

(b) Mounting sight   Cable connector   The sight element

Cable for voltage bias and output signal

Filter glass
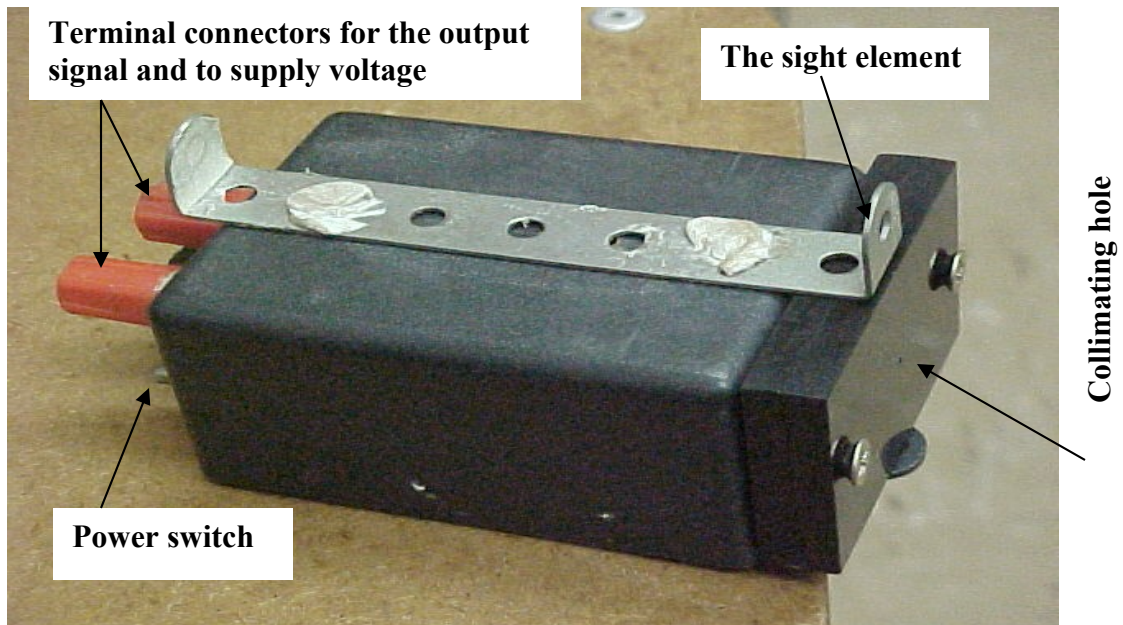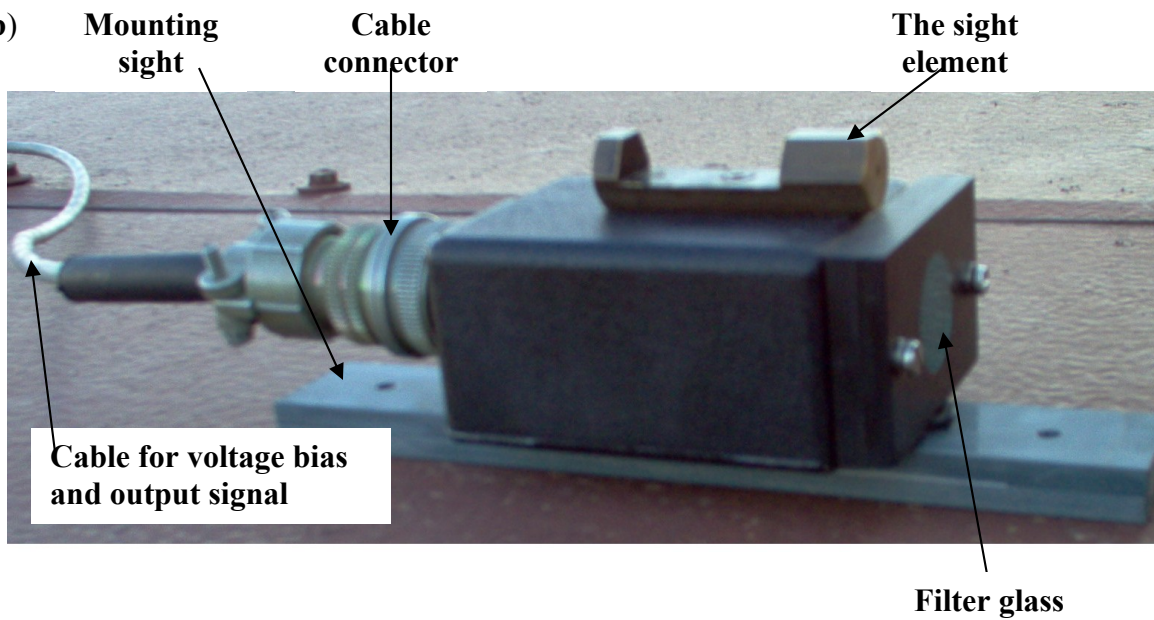
Figure 3.6: *A photograph of the DSRD1 (a) and the DSRD2 (b) detectors which incorporates various improvements carried out on the DSRD1.*

3.2   Calibration

In general, the goal of a calibration is to correct for small imperfections that are unavoidable in instruments operating under hostile conditions such as instruments for solar radiation measurements. A proper calibration of instruments for measuring direct solar radiation is intended to provide accurate measurements which are very important for evaluating the performance of solar systems. For example, the accuracy of solar cells calibrated as primary reference cells is directly dependent on the accuracy of the pyrheliometer used to measure the direct solar radiation that reaches the solar cell. Factors that influence the accuracy of pyrheliometer calibrations have been investigated [Thacher et al, 2000] and it was found that uncertainties of 0.8 % at a level of 2-sigma are still present.

The DSRD2 was calibrated using a comparison technique with the Eppley NIP whose characteristics are well known. The direct solar radiation data recorded from both instruments were plotted on the same graph to establish similarities and differences between the readings of the two instruments. A correlation factor was determined by plotting a graph of DSRD2 data against NIP data then fitting a polynomial regression equation. A best correlation occurs when the polynomial fit gives a root square (R^2) equal to one. A calculation of the error was also carried out. When a correlation is established the output of the DSRD2 can be converted from a voltage unit into an irradiance unit, in Wm^{-2} since the conversion factor for the NIP is known and is with on the casing of the instrument as 7.58×10^{-6} V/Wm^{-2}.

3.3 Experimental procedures

In this section a description is given of the steps followed in carrying out the measurements of direct solar radiation in order to investigate the characteristics of the DSRD1 detector.

3.3.1 Installation of the equipment

The equipment required to run the experiment was installed on a deck built on the rooftop, of the physics building at the University of Kwazulu Natal (Westville Campus). The roof is ~22.5 m high and ~325 m above sea level. The site was carefully chosen taking into account the different aspects that could introduce negative influences to the measurements. The aspects are listed as follows:

1. No object would cast a shadow over the location at any time during the measurements in an entire year.

2. To prevent any possible electrical noise interference, the cables from the instruments to the data acquisition system were made to be as short as possible.

3. All electronic equipment has been installed far away from any sources of electromagnetic waves.

4. The detectors (DSRD1, DSRD2 and NIP) were mounted on the Eppley sun tracker that is also mounted onto a rigid stand with good mechanical stability and well leveled to prevent any movement of the instruments during bad weather

days. The stand was solidly fastened to the roof-deck. However, as explained on page 42, the tracker can be aligned manually to cater for the solstices.

5. It was ensured that a free circulation of the operators and any visitors within the area would not interfere with the measurements.

6. No reflecting shiny surfaces such as roofs, light poles, white buildings or buildings with glass are located in the line of sight of the detectors.

7. The detectors were mounted such that there was a clear view of the sun at sunrise and at sunset.

3.3.2 Data acquisition system

The data acquisition system comprised a Hewlett Packard (HP) data logger model 34970A and a 20 channel multiplexer. The data logger was connected to a desktop computer via an RS-232 serial port. The software used to enable data manipulation is Bench Link. The data scanning time interval was set to one second. The connection between the instruments and the data acquisition system was achieved by a multicolor cable isolated from possibilities of electromagnetic shocks and rust to prevent electrical noise. It was also designed to be water-proof.

3.3.3 Measurement procedures

In measuring direct solar radiation, data were acquired using a data logger which was remotely controlled by a desktop computer using a serial interface. The data logger was set to scan readings at a time interval of one second and the data were recorded from

sunrise to sunset. The instruments used in the measurement are the DSRD1 detector, the DSRD2 detector and the Eppley NIP and these were mounted together on an Eppley sun tracker model ST-1. The data capturing was done in the following sequence.

1. A measurement of the direct solar radiation using the DSRD1 detector and the Eppley NIP only. This was intended to find the correlation between the readings of both instruments, where the NIP served as a reference. A voltage of 9.0 V was supplied using a 9.0 V battery.

2. The DSRD1 detector, the DSRD2 detector and NIP were all mounted together on the ST-1 tracker. The DSRD2 was fitted with the BG39 optical glass filter. A voltage of 9.0 V was supplied from a 30 V power supply unit.

3. Step 2 was repeated, but with the DSRD2 detector fitted with the KG optical glass filter.

4. The measurements were performed with no filter on the DSRD2 in order to compare with the readings of DSRD1 taken with no filter.

5. The DSRD1 was fitted with first the BG39 filter and then with the KG filter and measurements taken. The black perspex housing the DSRD2 was replaced with white perspex for investigation of the effect of temperature.

6. The battery on the DSRD1 was replaced with the power supply unit and the DSRD2 was powered from the battery. This is because it was assumed that the output signal of the DSRD1 had been affected by use of the battery as voltage supply.

7. Measurements of temperature in the interior of the detector housing were carried out using a temperature sensor LM 35 which was located near the sensor of the DSRD2.

This sensor is made up of a semiconductor and it gives an output signal in volts, where 10 mV is equivalent to 1 ° C.

In measuring polar response, measurements were performed as follows:

1. A measurement of direct solar radiation with the instrument aligned properly assuming this as the zero of angular position with respect to the solar beam. The angle of incidence was measured using a compass.
2. Data were recorded for different angles between $0°$ and $40°$ by varying the angle of incidence using the line of sight of the sun tracker

Chapter 4

4. Results and Discussion.

In this chapter, the results of the characterization and improvement are presented together with the results of the calibration. A major part of the measurements were carried out on averagely clear sky days. This is because it was required that the instrument be calibrated for clear sky days [Duffie and Beckman, 1991]. On a clear sky day, fluctuations in direct solar radiation with the time of day are comparable to those found in the standard solar radiation spectrum measured at sea level. A clear sky day is a day on which the obstruction of direct solar radiation is negligible. In this case, the atmosphere is assumed completely transparent to solar radiation. A turbid sky day is a day on which there are a lot of suspended particles called aerosols that cause a high level of scattering of solar radiation. The atmosphere is then assumed to be an opaque body through which no light passes.

The detection principle of the DSRD is based on direct conversion of the incident solar energy into a current which is then converted into a voltage. This is achieved by connecting an amplifier as a transimpedance on the integrated circuit of the DSRD. A resistance connected across the thermopile output converts the current produced at the

junction into a voltage. Thus, the output of the DSRD is a voltage signal. The output of the NIP is also a voltage signal. The conversion of energy in both detectors into a voltage signal is to enable the data logger to take readings directly from the detector. The magnitude of the output signal given by both DSRD1 and DSRD2 is of greater order compared to the magnitude of the output signal given by the reference instrument, the NIP. This is because the gain of the DSRD is greater than the gain of the NIP because the DSRD has a higher-gain amplifier incorporated in the circuit (see page 62). This situation has been corrected by calibrating the DSRD. The plot of direct solar radiation data collected using the NIP is indicated with the blue curve, while the plot of data collected with the DSRD1 is indicated with the red curve and the plot of data collected with the DSRD2 is indicated with the pink curve.

The NIP, being the reference instrument, is very important and deserves a brief description of its characteristic response to solar radiation. The trace shown in Fig.4.1 is a plot of direct solar radiation measured in volts with the NIP during a clear sky day. Before 07:00 the graph suggests that there is no variation in the amount of solar energy measured because it is before the sun rises. This occurs because the detection principle of the NIP is based on the difference in temperature between the junctions of the thermopile and its sensing element. After sunrise, the instrument absorbs solar energy and this causes a rise in temperature which produces an electrical current that can be measured as a voltage.

The graph of Fig. 4.1 also shows that the instrument gives negative values just before sunrise. The data logger was programmed to commence the recording process at 06:45 which was the estimated sunrise for that day. The negative readings suggest that the temperature difference on the junction of the thermocouple is negative and the sensing element is not absorbing energy but releasing it since there is no sun.
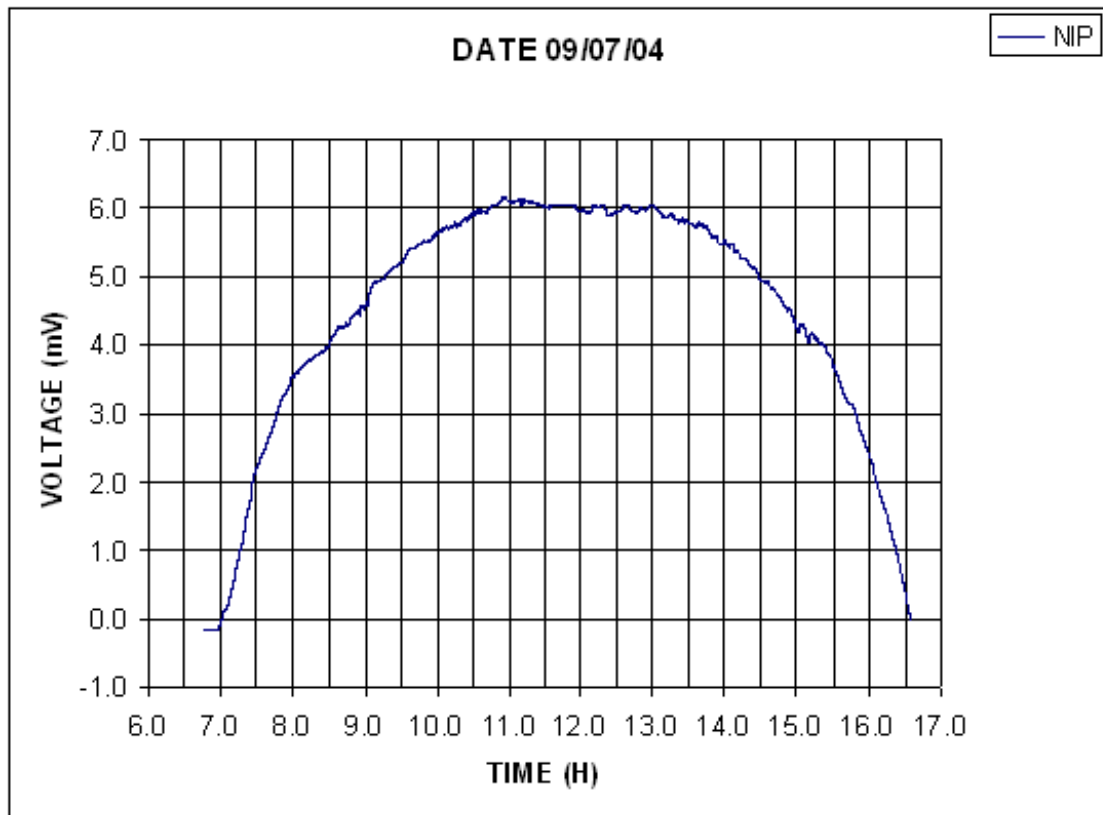
Figure 4.1: *A graph of direct solar radiation measured in volts using the NIP. The graph depicts the variations of the amount of solar energy that is available for a particular day.*

Another possible source of this fault in the instrument is the fact that it has not been calibrated since it was shipped in 1996 [Dhavraj, 1998]. This apparent weakness of the instrument is not expected to affect the results much though.

4.1   The DSRD1 and the NIP on a clear day

An experiment was conducted in order to investigate a general behavior of the DSRD1 detector in terms of its response to variations of solar radiation in comparison to the NIP. The data were taken on different days but under clear sky conditions. Four sets of measurements were performed, firstly with no filter, then with the KG filter, thirdly with the BG39 filter and finally using a power supply. The results are presented below.

4.1.1   The DSRD1 (with no filter) and the NIP

A concern and a most important aspect of the experiment is the way that the DSRD1 readings track the variation of solar radiation as given by the reference instrument. The results are shown in Fig. 4.2. The red curve represents a plot of direct solar radiation in volts measured using the DSRD1 and the blue curve is a plot of direct solar radiation also in volts, measured using the reference instrument, the NIP. The measurements were taken on 25th June 2004.

The scaling on the vertical axes is different due to the difference in magnitude between the readings of the DSRD1 and the NIP, the DSRD1 readings being about six times those of the NIP. The same axis system is used to enable a comparison in terms of how the measurements taken with the DSRD1 track the characteristic variations of solar radiation according to measurements obtained from the NIP.
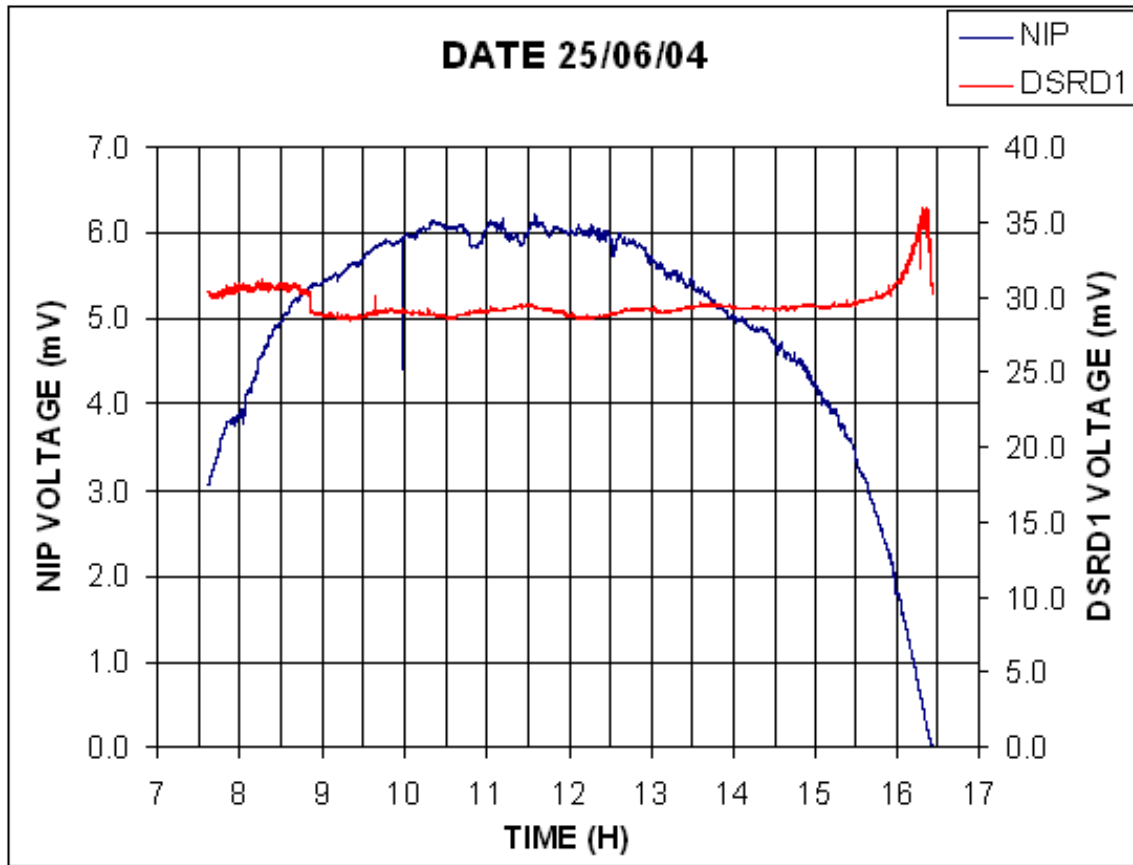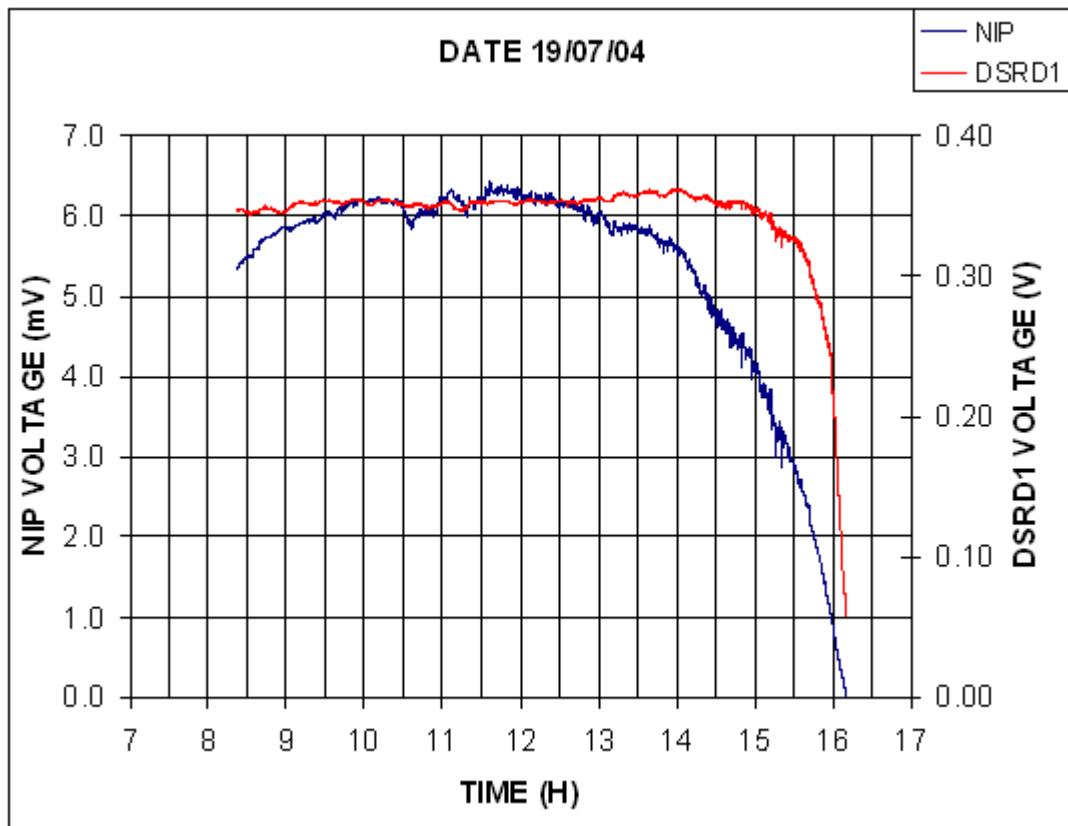
Figure 4.2: *A plot of direct solar radiation measured in volts using the DSRD1 (with no filter) and the reference instrument, the NIP. Here, the voltage applied to the DSRD1 was supplied from a 9.0 V battery.*

The graph of the reference instrument (blue) shows an increase in solar radiation intensity from sunrise to about 11:30 after which it starts to decrease until sunset at about 16:30. For a clear sky day this is the expected behavior of the variation in direct solar radiation intensity measured at sea level, taking into account the attenuation of solar radiation. In contrast, the graph of direct solar radiation measured using the DSRD1 shows no significant variations in intensity between about 07:30 and 15:30, after which it shows an increase towards sunset. This is a clear indication of malfunction of the DSRD1 detector for measuring direct solar radiation mainly since it should read zero at sunset. Because

there is more IR radiation towards sunset, it means that the DSRD1 is more sensitive to this type of radiation. The first filter used is thus aimed at cutting off this radiation.

4.1.2   The DSRD1 (with filter KG) and the NIP

The attempt to correct the spectral response of the DSRD1 was by the use of a cut-off glass filter, KG. The results of the performance of the DSRD1 combined with the filter are indicated in figure 4.3. These measurements were taken on 19th July 2004.
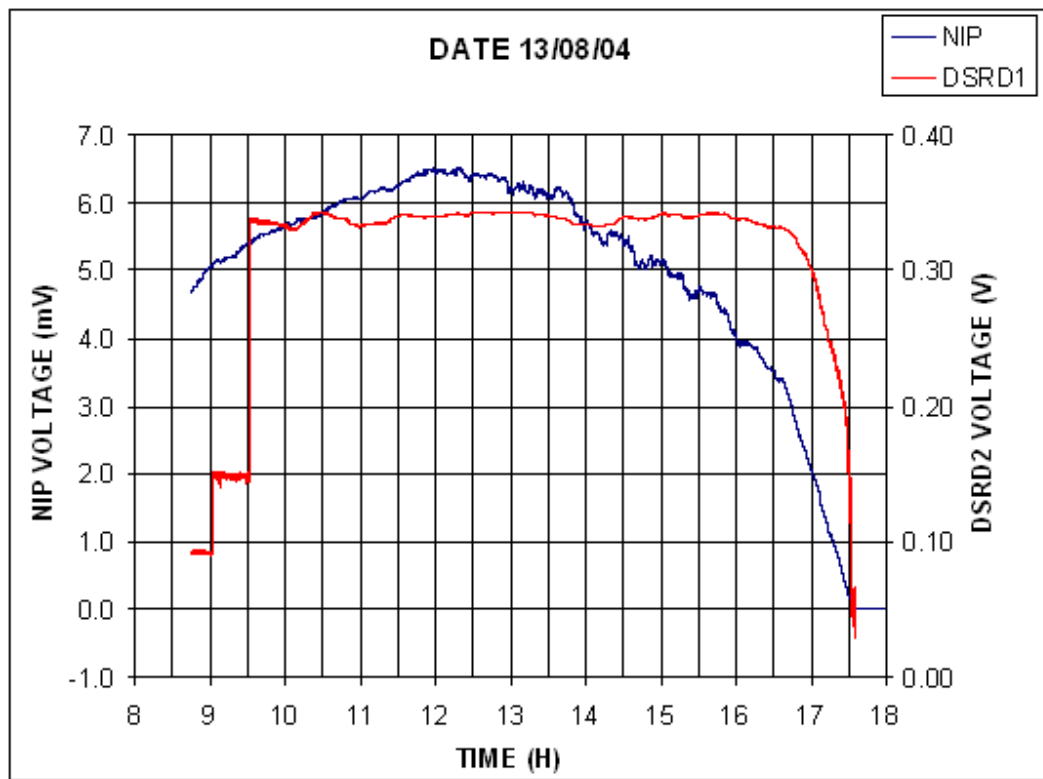

Figure 4.3: *A plot of direct solar radiation measured in volts using the DSRD1 (coupled to KG filter) and the NIP. A 9V battery was used as the voltage supply. (Note that the left scale is given in V).*

Figure 4.3 shows no significant difference in the readings given by DSRD1 except that towards sunset the results now indicate a decrease in direct solar radiation received. This

is contrary to the results plotted in Fig. 4.2. Another observation is that the magnitude of the signal from the DSRD1 has decreased dramatically by 2 orders of magnitude. The effect of IR radiation as indicated in figure 4.2 is not present here, which suggests that the filter is working to prevent IR radiation from the detecting element.

4.1.3   DSRD1 (with filter BG39) and the NIP

Figure 4.4 is a plot of solar radiation measured with the DSRD1 (coupled to the BG39 filter) and the NIP. The voltage is still supplied from the 9.0 V battery.

Figure 4.4: *A plot of direct solar radiation measured in volts using the DSRD1 (coupled to the BG39 filter) and the NIP. The voltage was supplied from a 9.0 V battery.*

The plot indicates that the spectral response of the detector has been modified although it is still not tracking the variations of the direct solar radiation properly as shown by the

results from the reference instrument. At 09:00 and at 09:30 the solar energy measured by

the DSRD1 increased abruptly before leveling off followed by another rapid decrease.

These results disagree with those given by the reference instrument. However, the results

indicate that the filter is working to block out IR radiation.

4.1.4 The DSRD1 (using a power supply, with no filter) and the NIP

The measurements were performed with a 30 V power supply unit in place of the 9 V

battery. Figure 4.5 shows the results of these measurements which were taken with no
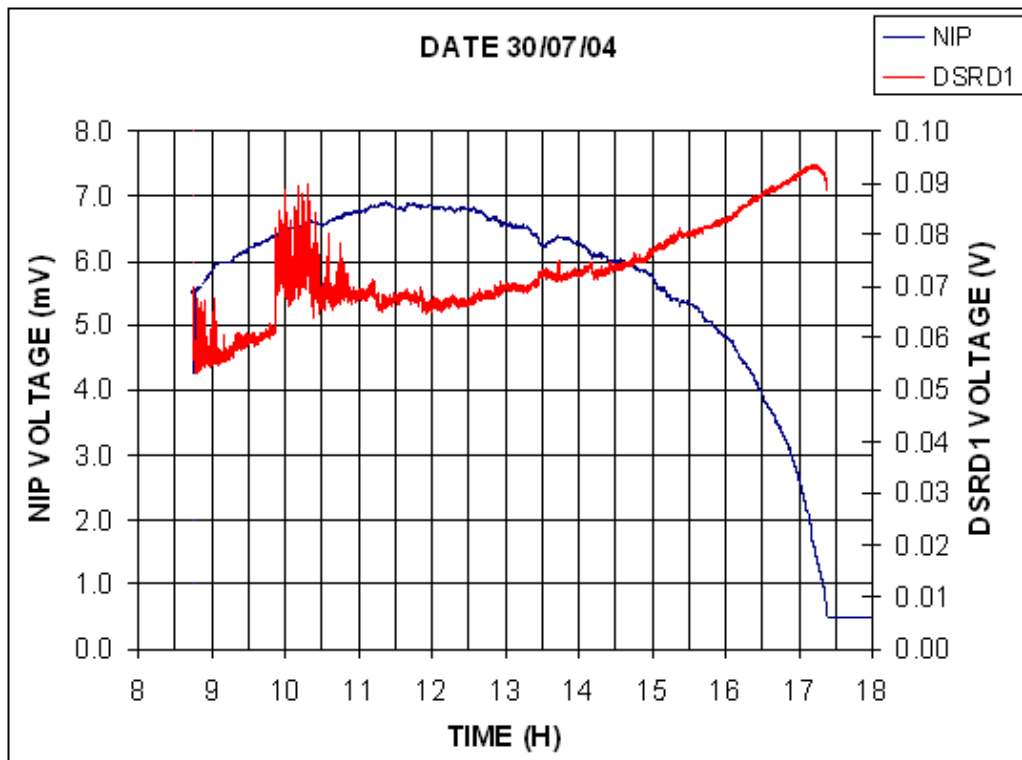
Figure 4.5: *A plot of direct solar radiation measured in volts using the DSRD1 (with no filter) and the NIP. The voltage was supplied from a 30 V power supply unit.*

filter. The data were taken on 30th July 2004. This plot reveals no improvement in the

readings given by DSRD1. In contrast to the readings of the reference instrument, the

90

readings of the DSRD1 suggest a turbidity in the sky between 08:45 and 11:00. Moreover, from 12:30 the readings of the DSRD1 suggest an increase of the amount of detected solar energy. Both of these results disagree with the readings of the NIP, and this can be attributed to the electrical noise associated with the power supply unit.

4.2   The DSRD1 and the NIP on a turbid day

On a turbid day, the scattering of the solar beam is higher and the amount of solar energy received on the earth's surface is lower and should show a predominance of infrared radiation.

4.2.1 The DSRD1 (with no filter) and the NIP

A presentation of direct solar radiation measured in volts using the DSRD1 detector and the NIP on a turbid day is shown in figure 4.6. The NIP readings reveal significant fluctuations in solar radiation intensity around noon and this means that during this period there was some interference that could be a spontaneous cloud cover or a spontaneous turbidity. However, the readings of the DSRD1 indicate no considerable variations in the amount of solar energy received during this period. Also, in contrast to the reference instrument, between 08:30 and 09:30, the readings suggest a decrease while from 16:00 the readings suggest an increase in the amount of solar energy received. The data were taken on 22nd July 2004.
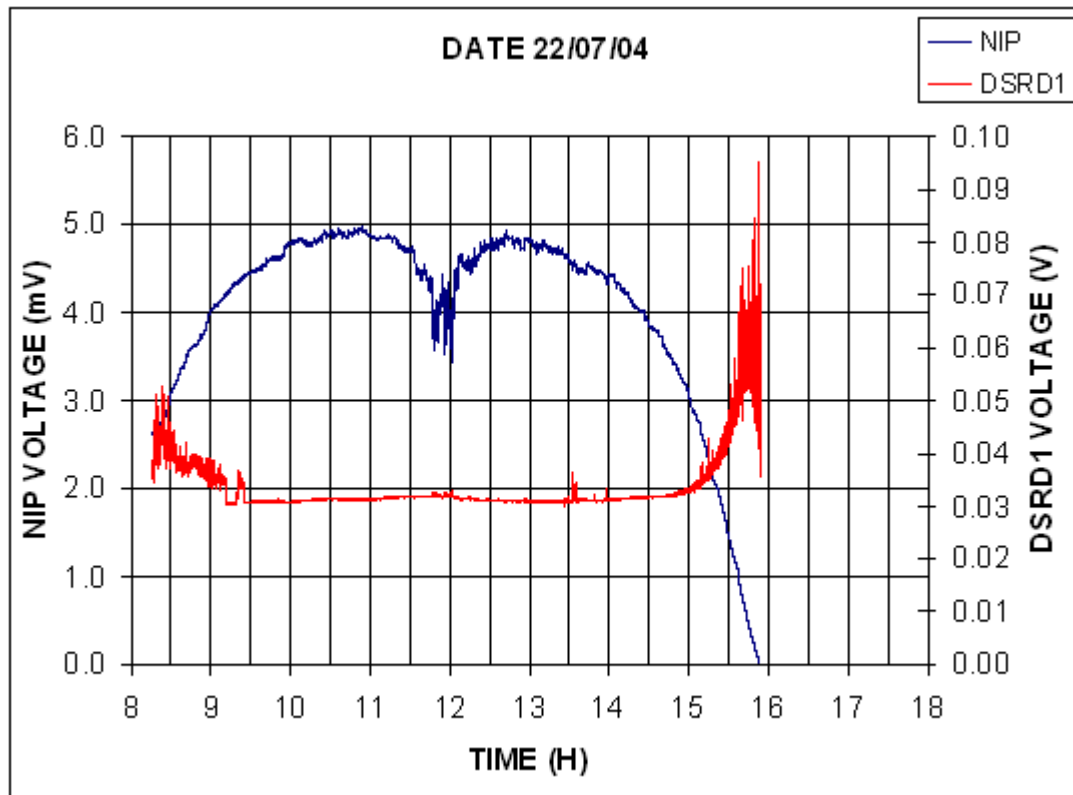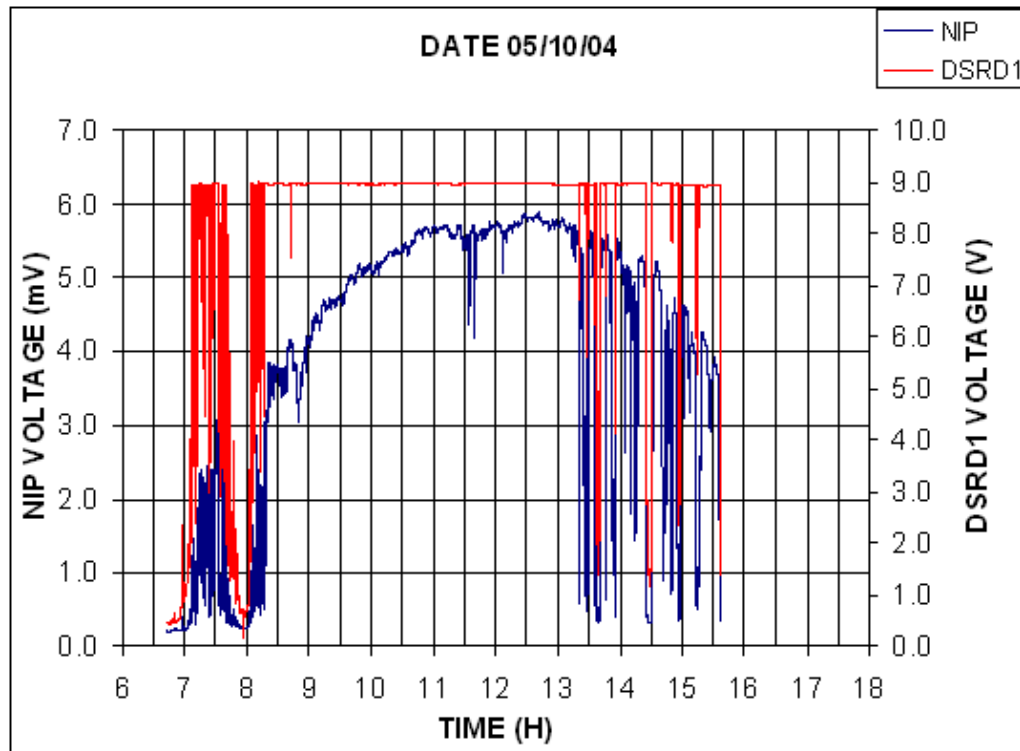
Figure 4.6: *A plot of direct solar radiation measured in volts using the DSRD1 and the reference instrument, the NIP. The voltage was supplied from a 9.0 V battery and the DSRD1 incorporates no filter.*

4.1.3   The DSRD1 (with the KG filter) and the NIP

In Figure 4.7, the results of the direct solar radiation measured in volts using the DSRD1 detector incorporating the KG filter on a day with a turbid atmosphere, are presented. The voltage was supplied to the DSRD1 from a 30 V power supply unit. Here, the interference occurred for almost the entire day with more significance between sunrise and ~09:00 and later between 13:00 and ~15:30. An error in the data acquisition system occurred that necessitated an interruption on data scanning just before sunset, hence the lack of data from about 15:00. The measurements were taken on 5th October 2004.
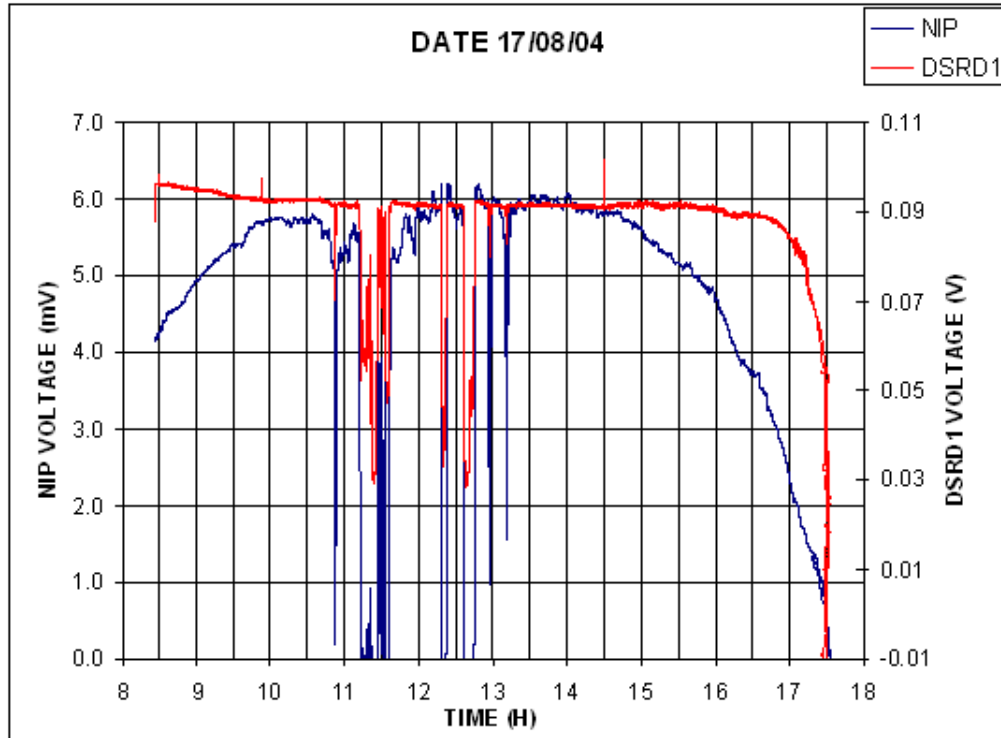
Figure 4.7: *A plot of direct solar radiation measured in volts using the DSRD1 and the NIP on a turbid day. The DSRD1 incorporates the KG filter and the voltage is supplied from the 30 V power supply unit (note that the left scale is given in V).*

comparison of the DSRD1 results and the NIP results reveals that the readings of the DSRD1 do not follow the variations in the amount of solar energy that reaches the earth's surface as indicated by the reference instrument. However, the detection of IR radiation, the predominant radiation during periods of intense scattering like on a turbid day, seems to be eliminated. For instance, this is indicated in the turbid period between ~07:00 and ~08:15 where the red trace shows a minimum.

93

4.2.3 The DSRD1 (with the filter BG39) and the NIP

The results of the measurements of direct solar radiation using the DSRD1 and the NIP on a turbid day are shown in Fig. 4.8. The voltage supplied to the DSRD1 was from the 30 V power supply unit. The measurements were carried out on 17th August 2004.

Figure 4.8: *A plot of direct solar radiation measured in volts using the DSRD1 and the NIP on a turbid day. Here, the DSRD1 incorporates the BG39 filter and the voltage is supplied from the 30 V power supply unit.*

The results shown in figure 4.8 indicate that around 10:30 to 13:00 there was interference in the atmosphere. A comparison of the DSRD1 readings and the NIP readings indicates that the readings from the former instrument do not follow the variations in the amount of solar energy that is received as shown by the reference instrument. However, the detection of IR radiation has been eliminated as shown by the lack of increase in voltage at around sunrise and sunset.

94

The overall results from the DSRD1 measurements reveal several aspects. Firstly, in both figures 4.2 and 4.3 the graphs show nearly similar characteristics. This is as if the amount of direct solar energy was increasing at near sunset times. For those situations when the DSRD1 incorporates an optical glass filter, a kind of malfunction is revealed. These results suggest that the detector sensitivity is more pronounced in relation to IR radiation since this type of radiation is predominant at sunset. Another observation is that the DSRD1 responds equally during the day, especially over the period when solar radiation should reach a peak value. This suggests that this poor correlation could be due to some alteration of the original characteristics of the detector, which could have caused by exposure to moisture and dust. It is for this reason that the DSRD2 detector was built using a sensing element with the same characteristics.

4.3   The DSRD2 and the NIP on a clear day

This section is a presentation of the results of the various improvements carried out on the DSRD1 with respect to the spectral response. The improvement is focused on coupling a glass filter to the detector to give an overall response. It is hoped that the response will better characterize the amount of direct solar energy received on the earth's surface especially on a clear sky day. The results are presented first, for the case with no filter and then for the two cases when the detector is coupled to the two different filters.

95

As mentioned earlier the blue trace represents data collected with the NIP and the pink trace, the data collected with the DSRD2.

4.3.1 The DSRD2 (with no filter) and the NIP

The DSRD2 was mounted together with the NIP on the sun tracker for a comparison of their responses. A plot of direct solar radiation measured in volts using the DSRD2 and the NIP is shown in Fig. 4.9.

The blue curve represents the measurements of taken with the NIP and the pink curve
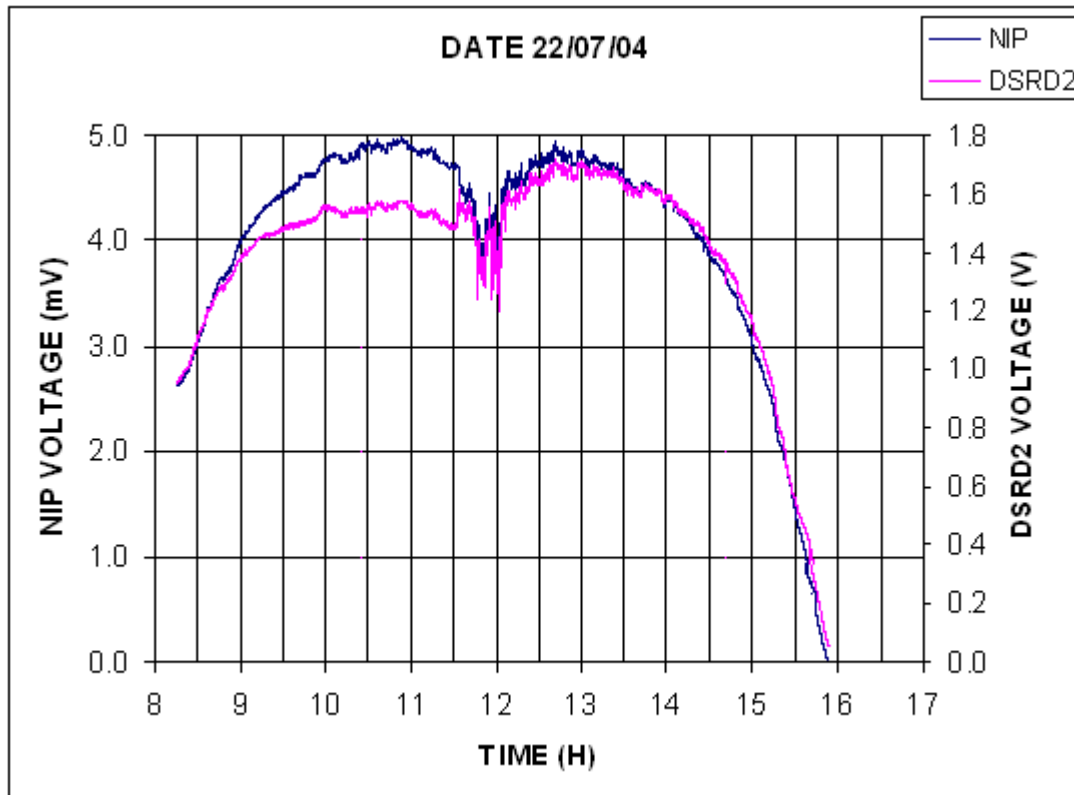
represents the measurements taken with the DSRD2. The data indicates that the DSRD2

Figure 4.9: *A graph of direct solar radiation measured in volts using the DSRD2 and the NIP. The voltage to the DSRD2 detector was supplied from the 30 V power supply unit.*

with no filter tracks the variations of direct solar radiation in a similar manner as the reference instrument. Since the sensing element is the same in both detectors, this means

that the optical properties of the sensing element on the DSRD1 detector must have been altered. This may have been caused by moisture and dust that could have accumulated in the housing and onto the surface of the sensor. This could have happened because the housing of the DSRD1 is not properly sealed. However, the DSRD2 graph does not exactly follow the NIP graph especially just before midday where the NIP reads higher than the DSRD2.

The fact that the readings of the DSRD2 between ~08:45 and ~12:15 are lower than the readings of the NIP suggests that the response of the sensor in the DSRD2 is dependent on the wavelength of solar radiation. This means that the DSRD2 responds better to radiation at near infrared region, which occurs in the period from sunrise until ~09:00 and from around 15:00 when the sun moves towards sunset. However, the traces indicate that even if the correlation is not good, the detecting device can be used to measure direct solar radiation with a reliable accuracy.

Figure 4.10 shows the plot of correlation between readings taken with the DSRD2 and those taken with the NIP. Also shown in red is a curve fit to the data and this can be used to correct the small imperfections on the readings of the DSRD2 that are observed from
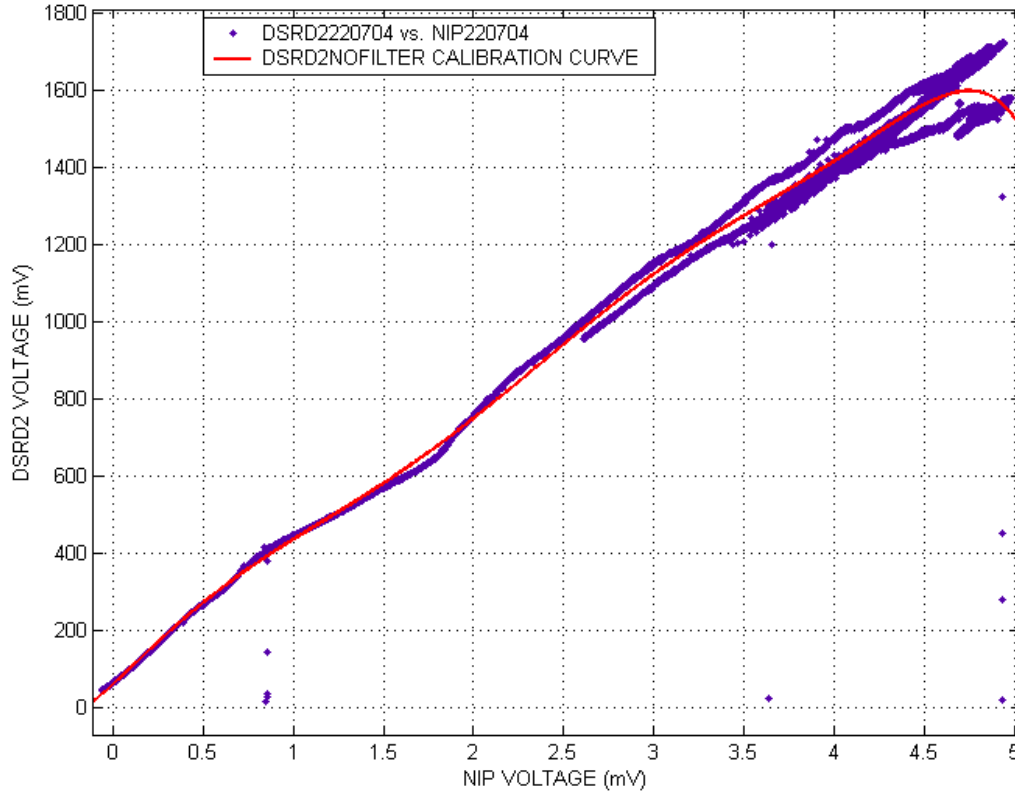
the plot. The plot shows a significant deviation of the calibration curve in relation to the plot of correlation from 1.5 mV of the NIP voltage.

The calibration curve displayed is a well-known and long-established polynomial function of the 8th order established from that of first order (a linear equation as $bx^1 + c = y$) and that of second order (a quadratic equation as $ax^2 + bx^1 + c = y$) and so on. It is given by

$$P = P_1x^8 + P_2x^7 + P_3x^6 + P_4x^5 + P_5x^4 + P_6x^3 + P_7x^2 + P_8x + P_9 \qquad (4.1)$$

Figure 4.10: *A graph of correlation between the DSRD2 and the NIP measurements. The red curve represents the calibration factor which must be taken into account to correct the readings of the DSRD2 in order that they agree with those from the reference.*

where $P_1, P_2, P_3, \ldots P_9$ are the polynomial coefficients whose values are given in Table 4.1 and x represents the data points. In the table, SSE, the sum square error, is a measure of total deviation of the data points to the curve fitting, R^2 is the root square that indicates how successful the fit is for calibration of the DSRD2 with respect to the reference instrument and RMSE is the root-mean-square error which shows how far the evaluated points are from the reference. A good fit will have $R^2 \sim 1$ and RMSE ~ 0.

Table 4.1: *A summary of the polynomial coefficients of the calibration curve and errors introduced by measuring direct solar radiation with no filter on the DSRD2.*

Data set	Polynomial coefficient								
	P_1	P_2	P_3	P_4	P_5	P_6	P_7	P_8	P_9
22/07/04	-0.0976	0.5482	6.586	-70.55	240.6	-323.4	87.07	435.4	58.25
	The goodness of fit								
	SSE			R^2			RMSE		
	72.33			0.97638			0.514		

4.3.2 The DSRD2 (with the KG filter) and the NIP

For the correction of the spectral response of the DSRD2 optical glass filters were implemented. In this section the results of the measurements performed using the DSRD2 coupled to the KG filter and the NIP are presented. The filter was fitted in such a way that it could double as a seal to prevent any rain, moisture or dust from entering the enclosure and accumulating onto the surface of the sensor. In this way the collimating hole was also sealed. Thus, the DSRD2 was able to withstand any atmospheric conditions. It could therefore be left on the tracker overnight such that sunrise and sunset data could be recorded. To start measurements at sunrise all that is required is to set the data logger.

Presented in Fig. 4.11 is a plot of direct solar radiation measured with the DSRD2 after it had been fitted with the optical glass filter KG and the NIP. This filter transmits radiation only in the visible region of the solar radiation spectrum (0.4 μm 0.75 μm) and also at far infrared (λ>10 μm). For a better visualization and easier comparison of the manner that both instruments track the variations in the amount of solar energy measured, the measurements obtained from the DSRD2 incorporating the KG filter were plotted together with the measurements obtained from the NIP on a same graph. The plot was generated from the data taken on 9th July 2004. The data scan begun at 06:45 and the graph shows a decrease in measured energy even though it was not sunrise yet. Since the sensing element of the DSRD2 is a photodiode and it has an integrated amplifier, this situation may be associated to leakage current.

On the other hand, the DSRD2 is detecting infrared radiation which is predominant after sunset and in atmospheric conditions that cause high scattering of solar radiation. When the sun rises the type of radiation predominant is in the visible region therefore after 07:00 the graph shows an increase of solar energy measured until noon and thereafter the amount of energy decreases because from noon the sun is moving further away from the detector with the consequence that the path length of the solar beam increases and as a result there is an intensification of attenuating effects in the atmosphere.
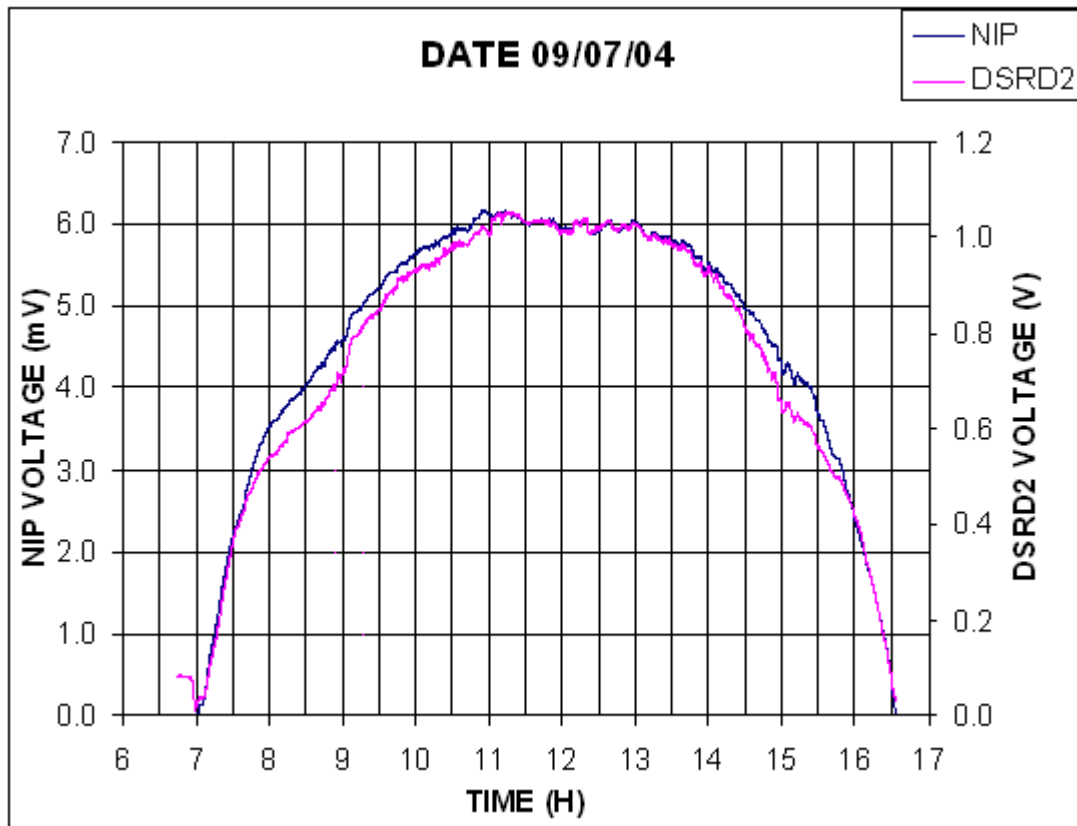
Figure 4.11: *A plot of direct solar radiation measured in volts using the DSRD2 and the NIP. The DSRD2 incorporates an optical glass filter KG. (Note that the left scale is given in V)*

For a comparison of the trend, the plot of figure 4.11 shows that the DSRD2 (coupled to the KG filter) tracks very well the variations in the amount of solar energy that reaches the earth's surface. This is because its readings follow very closely the readings of the reference instrument. The differences in the morning and in the afternoon are very small as shown by the difference in area. In either case, however, the DSRD2 reads lower than the reference. These results show a noticeable improvement to the data of Fig. 4.9, the case with no filter.

For a comparison of the magnitude of the readings obtained from the two instruments, the values of the measurements obtained from the DSRD2 were corrected to the measurements obtained with the NIP as determined from figure 4.11. This correction factor is 171.429 and the result is shown in figure 4.12. The difference between the readings is, however, lower and this indicates that the DSRD2 reads closer to the reference. The correction factor was evaluated first by the ratio between the DSRD2 measurements and the measurements from the NIP for each corresponding data point. Secondly, an average of the ratio values was calculated and this was used to divide into each data point. The result from this division was used in the plot in Fig. 4.12 and has been evaluated as 171.429.
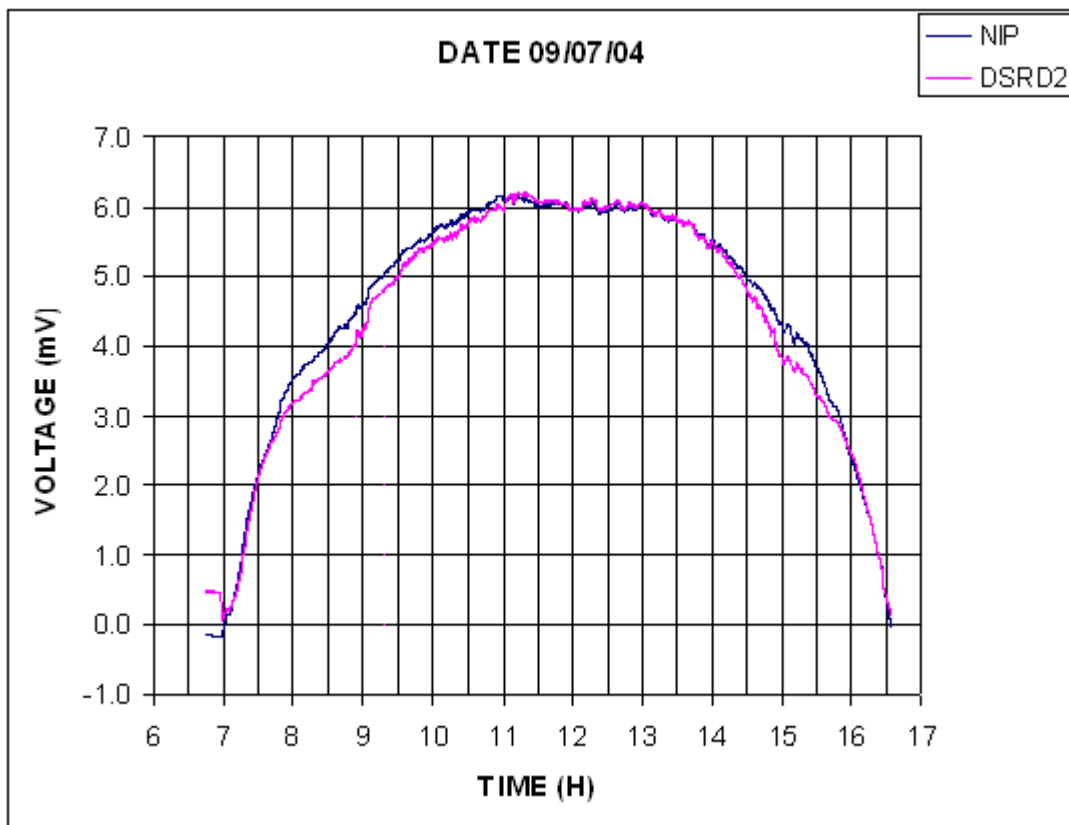
Figure 4.12: *A plot of the direct solar radiation measured in volts using the DSRD2 and the NIP. This plot indicates a characteristic behavior of the variation of solar energy on a clear atmospheric conditions day.*

A comparison between the graphs in Fig. 4.12 indicates that the DSRD2 reads lower in the period that extends from 07:45 until 11:00 and also between 14:15 and 16:00. The reason for this difference is associated with the fact that the combined spectral response of the sensing element and the KG filter (according to Fig. 3.5) varies with respect to the wavelength of solar radiation. Nevertheless, the use of the optical glass filter KG has improved the spectral response compared to the case when no filter was used.

Figure 4.13 is a plot of correlation between data obtained from the DSRD2 incorporating the KG filter and the data from the NIP showing also the calibration curve.
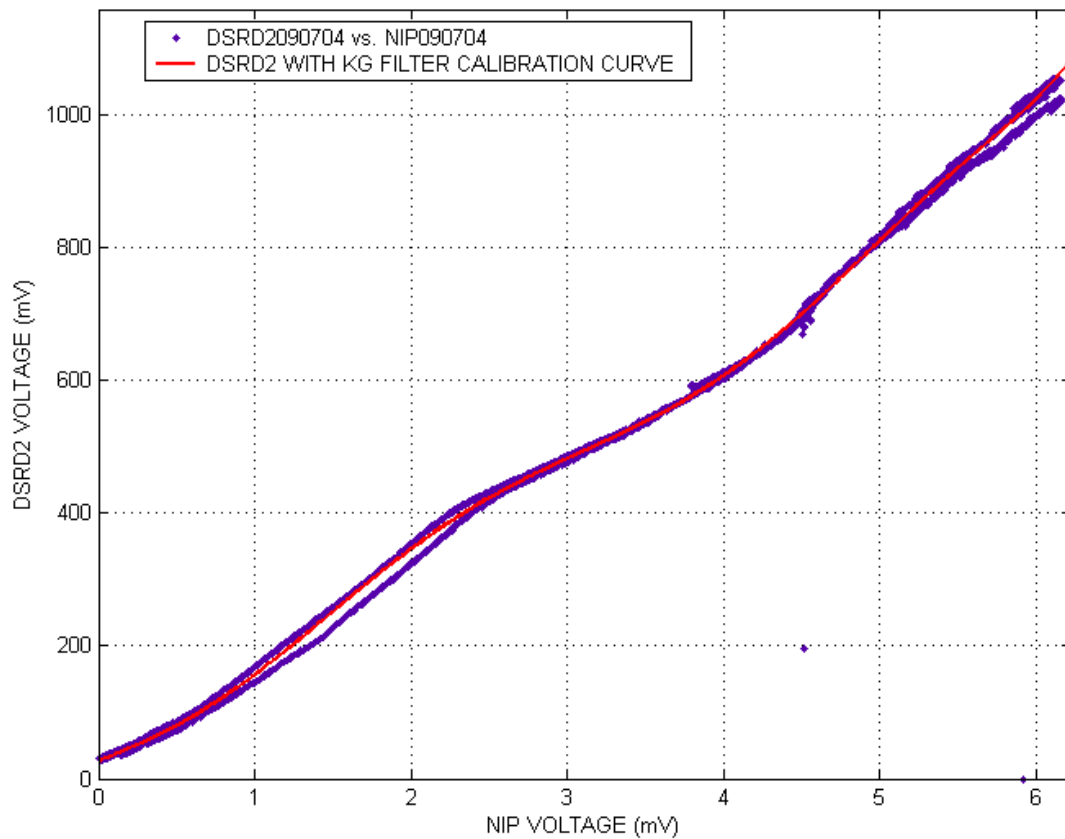
Figure 4.13: *A graph of correlation between the DSRD2 and the NIP measurements. The red curve represents the calibration factor which must be taken into account to correct the readings of the DSRD2 in order that they agree with those of the reference.*

The figure reveals that the readings of the DSRD2, when fitted with the KG filter, tracks comparatively with the reference. The figure also shows a good curve fit for calibration of the DSRD2 since the calibration curve follows very well the correlation curve. There is better agreement in this case than there was in Fig.4.10. This calibration curve is also a polynomial function of 8th order as evaluated by Eq. (4.1), with coefficients given in Table 4.2. The two lines displayed in Fig. 4.13 are due to the nearly parabolic form of the graphs in Fig. 4.12 and this causes a duplication of data points in the correlation curve.

Table 4.2: *A summary of the polynomial coefficients of the calibration curve and errors introduced by measuring direct solar radiation with the DSRD2 incorporating the KG filter.*

Data set	Polynomial coefficient								
	P_1	P_2	P_3	P_4	P_5	P_6	P_7	P_8	P_9
09/07/04	0.013	-0.185	0.060	9.762	-53.81	97.31	-23.81	100.1	26.84
	The goodness of fit								
	SSE			R^2			RMSE		
	0.4112			0.99878			0.0976		

The value of R-square is nearly equal to unity and this means that the readings given by the DSRD2 incorporating the KG filter are nearly equal to those given by the reference. In other words, this combination of the DSRD2 and the KG filter provides a better characterization of direct solar radiation which nearly mimic the reference instrument. The value of the root-mean-square error is nearly equal to zero and this means that the deviation in relation to the reference can be considered as negligible.

4.3.3   The DSRD2 (with the BG39 filter) and the NIP

In this section the results presented refer to the measurements acquired using the DSRD2 after it was fitted with the optical glass filter BG39. This filter transmits solar radiation in the wavelength range between 0.32 and 0.70 µm. Presented in Fig. 4.14 are the measurements obtained from the DSRD2 (fitted with the BG39 filter) and the NIP. The data were taken on 25th June 2004.
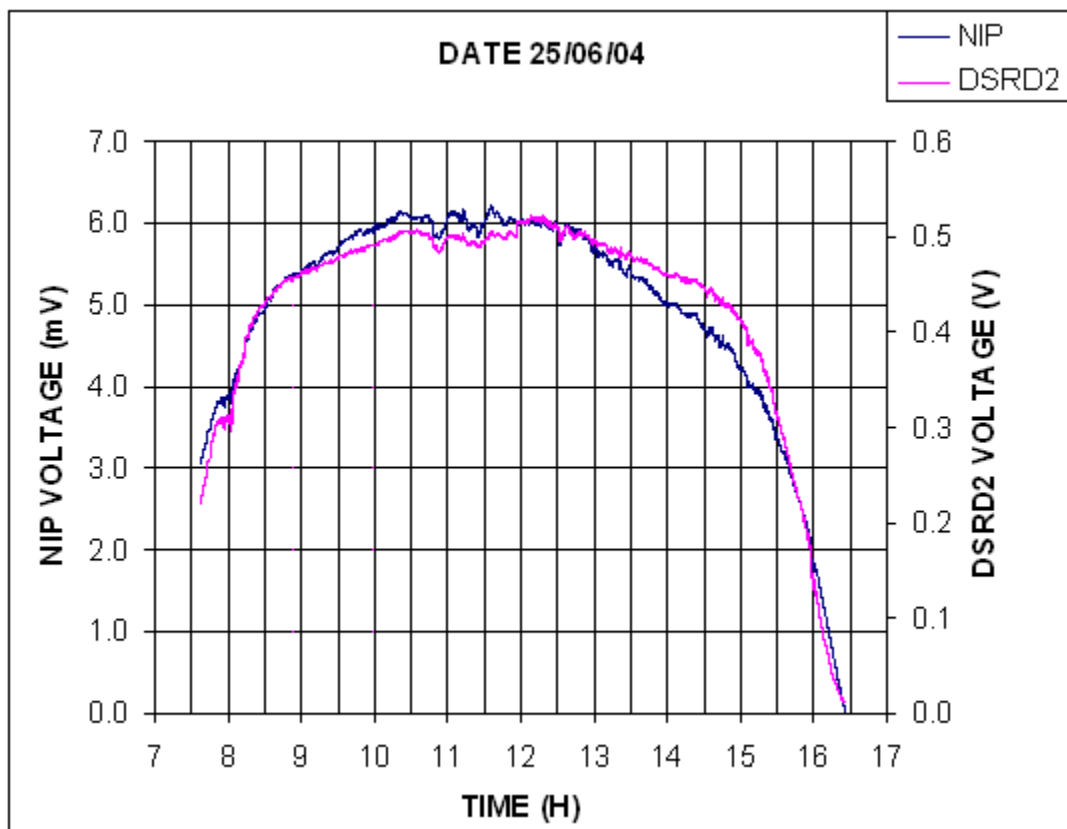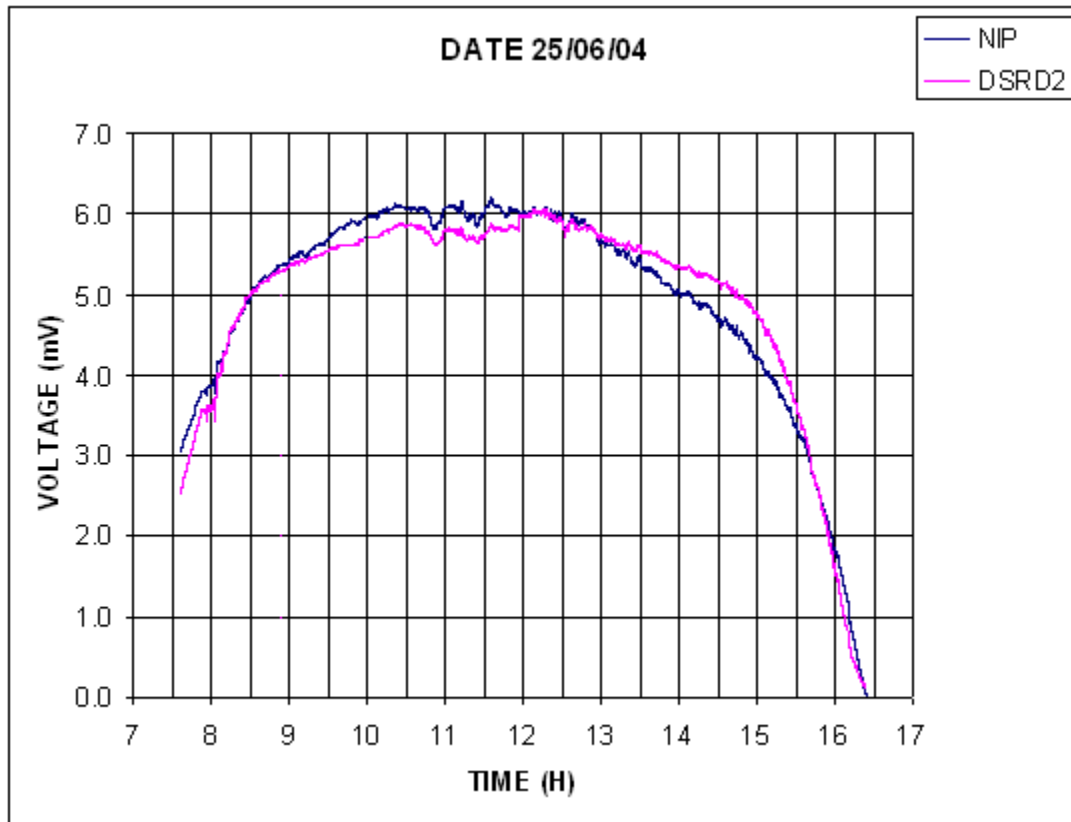

Figure 4.14: *A plot of direct solar radiation measured in volts using the DSRD2 and the NIP. The DSRD2 is fitted with the BG39 filter and the voltage is supplied from the 30 V power supply unit.*

The plot is a presentation of data obtained on a clear sky day. As can be seen from the figure, minor variations in the amount of solar energy detected are recorded and these are radomly caused by atmosoheric conditions. On a clear sky day like the case shown in the

105

figure, the amount of solar energy recorded by the NIP and the DSRD2 increases as the sun approaches the detector with a peak at noon. The DSRD2 voltage is about two orders of magnitude higher than the NIP voltage. In general, the graph of Fig. 4.14 indicates that the DSRD2, when fitted with the BG39 filter, produces a signal that follows the variations in the amount of solar energy as measured by the NIP at the earth's surface and even records the occurrence of spontanious interference. As seen in the previous sections, the magnitude of the signal obtained with the DSRD2 is higher than that obtained with


the reference instrument. In order to compare the trend and the magnitude, the data

Figure 4.15: *A plot of direct solar radiation measured in volts using the DSRD2 and the NIP on a clear sky day. The DSRD2 incorporates the optical glass filter BG39, and the DSRD2 data have been corrected to the NIP data by 85.714.*

obtained from the DSRD2 are corrected to the NIP data by multiplying by 85.714. This is

shown in Fig. 4.15

There is generally good agreement between the DSRD2 and the reference except at two regions starting around 10:00 and 14:00. In the former case the DSRD2 reads lower than the reference, while in the latter case it reads higher. This shows that the DSRD2 fitted with the BG39 filter has less sensitivity to direct solar radiation during a period in which the predominant radiation is of a wavelength of ~0.45 μm. This is towards the time of maximum solar irradiance when the sun is at the closest position in relation to the detector. In the later case, the DSRD2 has higher sensitivity in the afternoon, a period leading towards maximum temperature when the earth is beginning to irradiate more of the absorbed radiation.

A plot of the correlation curve between the data obtained with the DSRD2 incorporating the BG39 filter and data obtained by the NIP is given in Fig.4.16 together with the fitting curve for calibration of the DSRD2. The graph reveals discrepancies between the correlation curve and the fitting curve. In other words, the fitting curve does not follow the correlation curve. This suggests that a combination of the DSRD2 and the BG39 filter
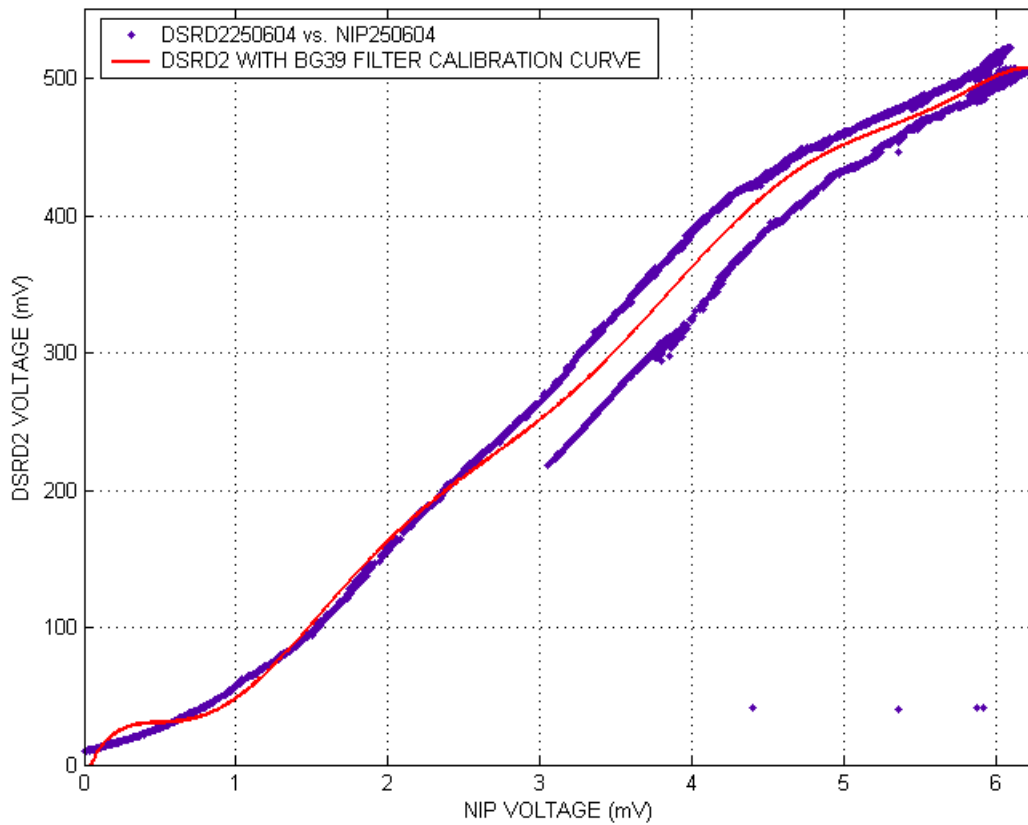
is not good for measuring direct solar radiation since it has poor agreement with the reference instrument. The second blue line appearing at higher NIP voltages can be explained for similar manner as in Fig. 4.13. The correlation coefficients and the errors are summarized in Table 4.3 and the values indicate that a better correlation between the DSRD2 and the NIP is achieved when the former detector incorporates a filter than when

108

without it. However, the R-square value obtained with the KG filter is closer to unity than that obtained with the BG39 filter.

Table 4.3: *A summary of the polynomial coefficients of the calibration curve and errors introduced by measuring direct solar radiation with the DSRD2 incorporating BG39 filter.*

Data set	Polynomial coefficient								
	P_1	P_2	P_3	P_4	P_5	P_6	P_7	P_8	P_9
22/07/04	0.011	2.844	-30.44	170.4	-530.9	900.7	-735.8	282.7	-10.9
	The goodness of fit								
	SSE			R^2			RMSE		
	2.228			0.98344			0.1454		

The RMSE value is more closer to zero in first case than in the second case. This means that a better combination between the DSRD2 and the filter is achieved with the KG filter than with the BG39 filter. Comparing R-square and RMSE values from all three tables

Figure 4.16 *A graph of correlation between the DSRD2 (incorporating the BG39 filter) and the NIP measurements. The red curve represents the calibration factor which must be taken into account when correcting the readings of the DSRD2 in order that they are of same magnitude as those from the reference.*

shows that the performance of the DSRD2 is better when it has a filter coupled to it.

Table 4.4 summarizes the values of R-square and RMSE for these three situations.

Table 4.4: *A summary of the goodness of the correlation between the readings of the DSRD2 and the NIP for the three situations presented above for a clear sky day.*

DSRD2	SSE	R^2	RMSE
With no filter	72.33	0.97638	0.5139
With the KG filter	0.4112	0.99878	0.0976

| With the BG39 filter | 2.228 | 0.98344 | 0.1454 |

4.4   The DSRD2 and the NIP on a turbid day

Measurements of direct solar radiation with the DSRD2 on a turbid sky day were also performed. The data has, however, not been used in the calibration of the DSRD2, rather it has been used to give an indication of how good the response of the DSRD2 to direct solar radiation is in other sky conditions. This means that the graphs of correlation as well as the coefficients for each situation are presented merely to evaluate the goodness and the reliability of the readings obtained from the DSRD2 and the suitability of each optical glass filter investigated.

### 4.4.1   The DSRD2 (with no filter) and the NIP

Measurements of direct solar radiation with the DSRD2 (with no filter) for a turbid sky day are presented in Fig. 4.17. The measurements were taken on 23rd July 2004, and the DSRD2 signal is about 33.33 times larger than that of the NIP.
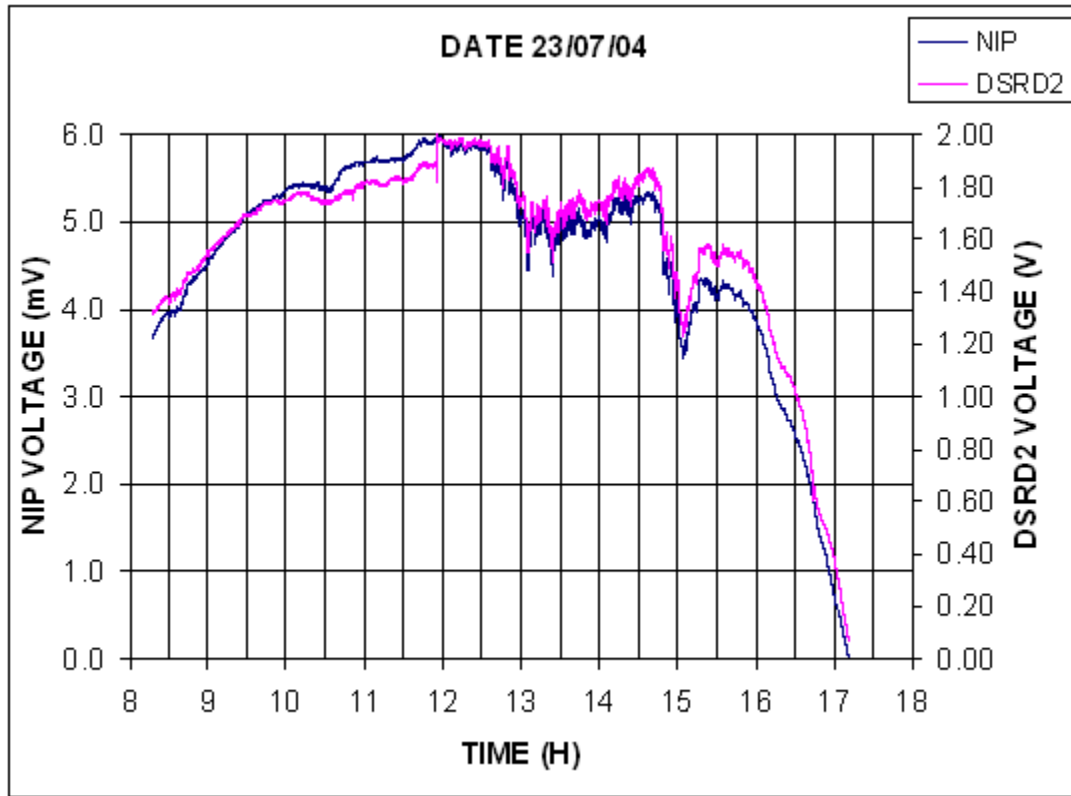
Figure 4.17: *A graph of direct solar radiation measured in volts using the DSRD2 and the NIP on a turbid sky day. The DSRD2 incorporates no filter.*

The figure shows that from about 10:00 up to 16:00 there occurred a significant variation of direct solar radiation incident onto the detector and this suggests that the sky was turbid. An important observation is that the DSRD2 keeps tracking the variations in direct solar radiation and follows closely the NIP curve. Although readings from the DSRD2 in this plot appear to be following the readings of the NIP, the data can not be used for calibration. This is because the WMO recommends that any calibration of radiometers must be carried out under clear sky conditions [Duffie and Beckman, 1991].

In Figure 4.18 the DSRD2 data has been corrected to the NIP data for a comparison of their magnitudes.
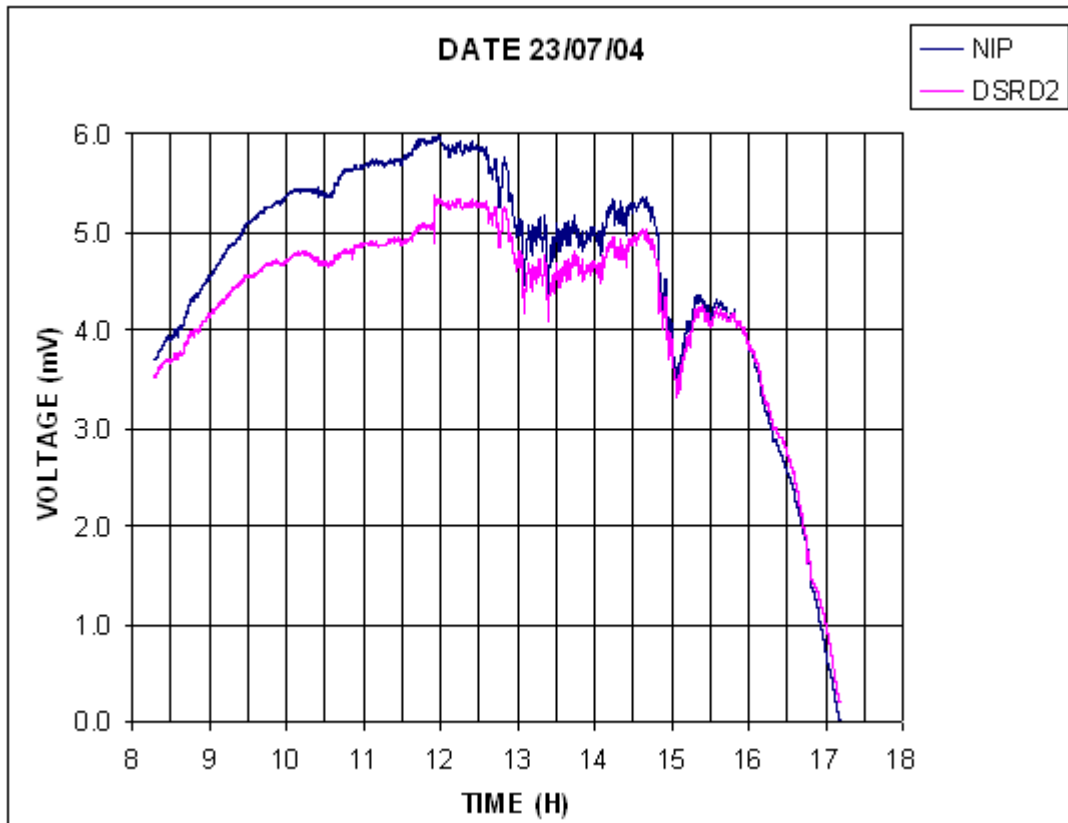
Figure 4.18: *A plot of direct solar radiation measured in volts using the DSRD2 and the NIP on a turbid day. Here, the magnitude of the signal acquired with the DSRD2 was corrected to that of the signal acquired with the reference instrument. The DSRD2 incorporates no filter.*

As seen from the figure the magnitude of the signal obtained from the DSRD2 is greater than that of the signal obtained from the reference instrument.

For correction of the measurements obtained from the DSRD2, the procedures are as explained in section 4.3.1. Of interest in the figure is that before 13:00, the NIP reads much higher than the DSRD2. In the afternoon the magnitudes are comparable.

Figure 4.19 is a plot of correlation between the DSRD2 (with no filter) and the NIP

readings on a day when the sky was turbid. The curve fit is a polynomial function of 8th

order as in Eq. (4.1). This fitting curve does not track the correlation curve and this
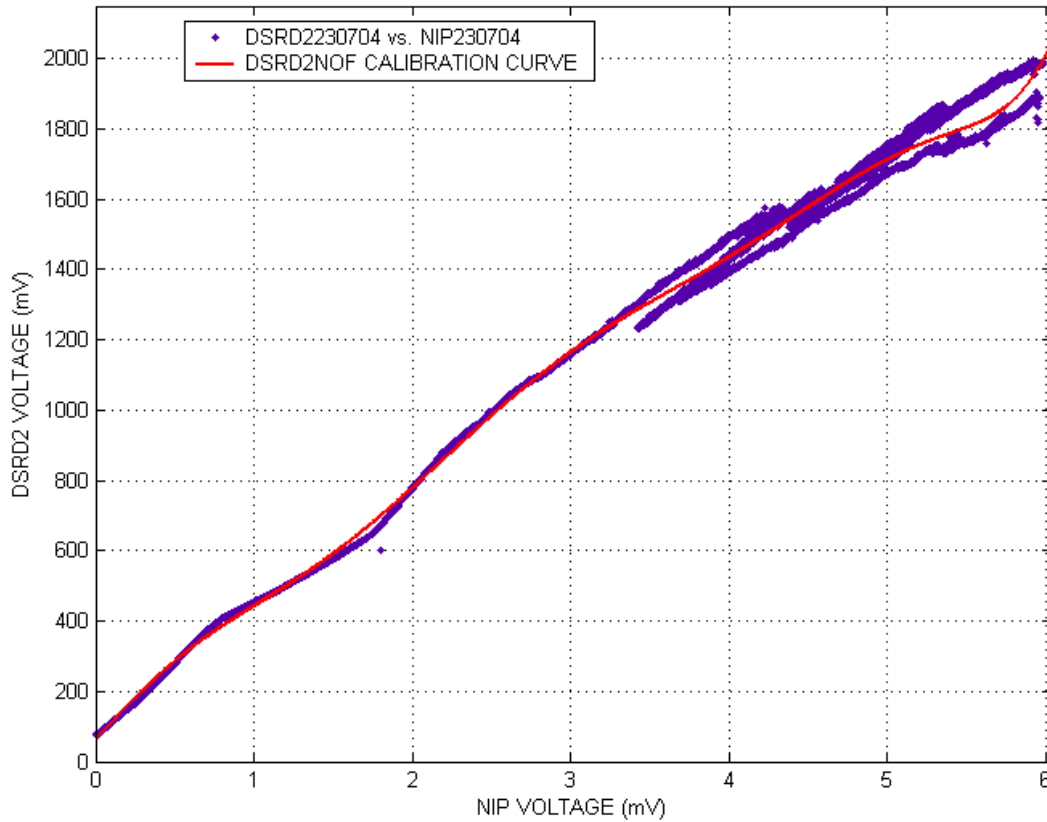
Figure 4.19: *A graph of correlation between the DSRD2 and the NIP on a turbid day. The DSRD2 incorporates no filter and the red curve represents the calibration factor that would be taken into account to correct the readings of the DSRD2 to those of the reference.*

suggests a significant level of error as evinced by the large difference in magnitudes up to

about 15:00. The polynomial coefficients corresponding to the plot of Fig.4.19, are

presented in Table 4.5 were the R^2 value is close to unity but the RMSE value is much

higher than zero.

Table 4.5: *A summary of the polynomial coefficients of the calibration curve and the errors introduced by measuring direct solar radiation with the DSRD2 with no filter on a turbid day.*

| Data set	Polynomial coefficient								
	P_1	P_2	P_3	P_4	P_5	P_6	P_7	P_8	P_9
23/07/04	0.269	-6.039	54.00	-242.3	559	-582	117.6	481.1	61.02
	The goodness of fit								
	SSE			R^2			RMSE		
	46.9472			0.98708			0.4144		

4.4.2   The DSRD2 (with the KG filter) and the NIP

Figure 4.20 is a plot of direct solar radiation measured on a turbid sky day. The DSRD2 was incorporating the optical glass filter KG. The measurements were taken on 2nd July 2004. It is important to note that the two plots of Fig. 4.18 and Fig.4.20 refer to different dates with different levels of atmospheric turbidity. The concern is, however, the manner in which the readings of the DSRD2 follow the variations in solar radiation intensity as indicated by the reference instrument. Even though it is turbid, the DSRD2 follows closely the NIP readings.
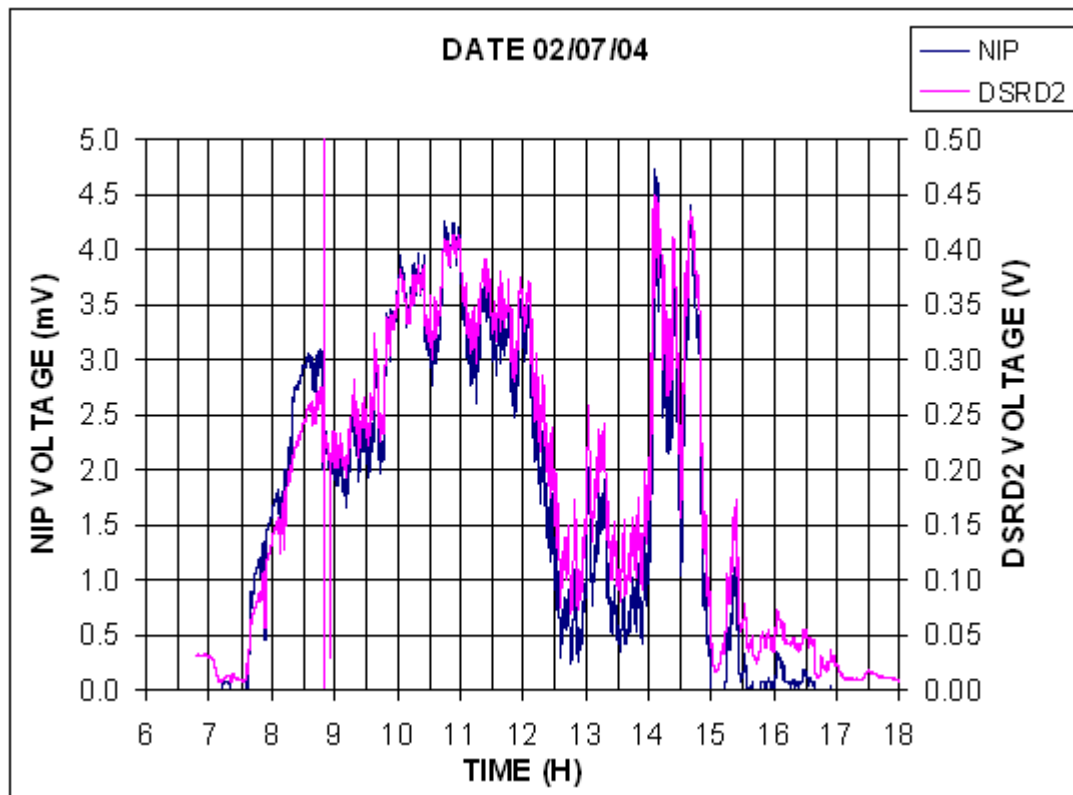
Figure 4.20: *A plot of direct solar radiation measured in volts using the DSRD2 and the NIP on a turbid day. The DSRD2 incorporates the optical glass filter KG.*

Figure 4.21 displays the measurements taken with the DSRD2 corrected to the magnitude of measurements taken with the NIP. The correction factor is 100 as evaluated from figure 4.20. The results here show that the NIP reads consistently higher than the DSRD2 in the morning, but lower in the afternoon. It is, however, to be noted that the DSRD2 follows the NIP throughout the day. This indicates that after having been calibrated the DSRD2 fitted with the KG filter will be able to read with a reasonably good accuracy.
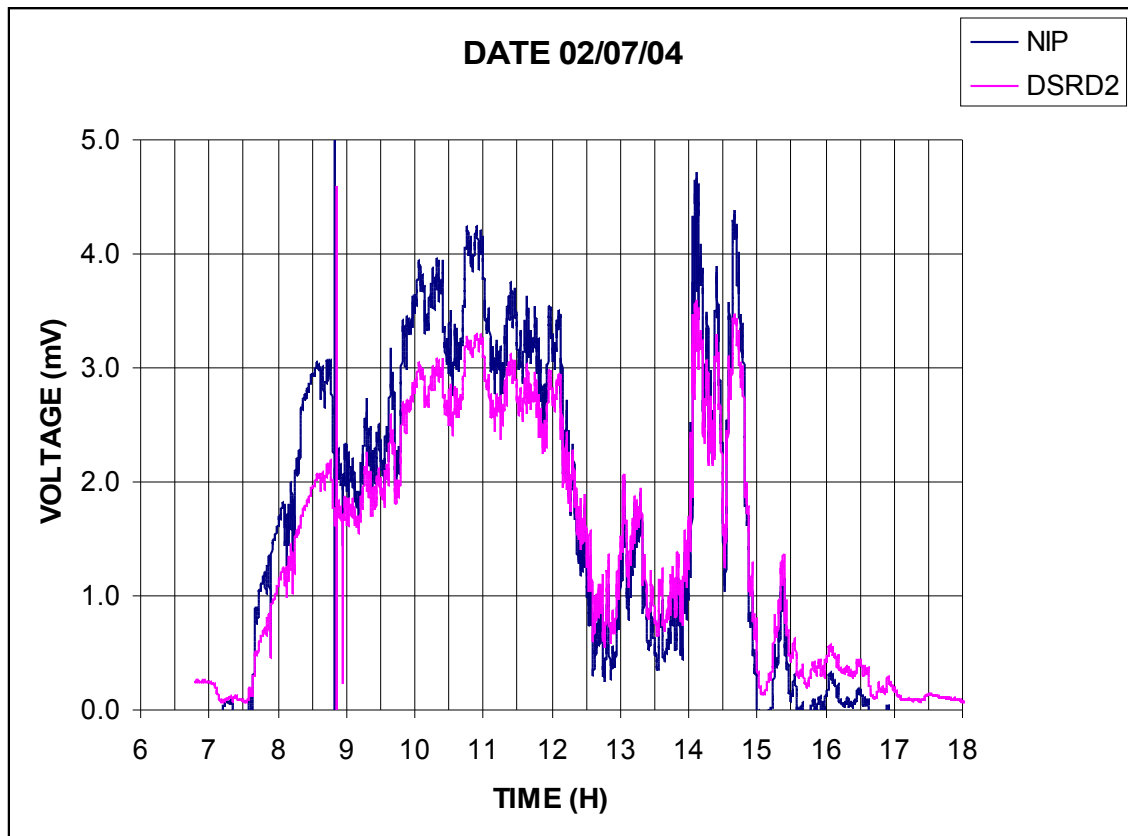
Figure 4.21: *A plot of direct solar radiation measured in volts using the DSRD2 and the NIP on a turbid day. The DSRD2 incorporates the KG filter and the magnitude of measurements obtained from it is reduced to those obtained from it has been corrected to those obtained from the reference instrument.*

This plot reveals that the DSRD2 fitted with KG filter, reads consistently lower than the NIP at around 10:00. Nevertheless, it tracks very well all fluctuations in solar energy received. This indicates that after having been calibrated the DSRD2 fitted with KG filter will be able to read with a good accuracy.

The plot of correlation between readings given by the DSRD2 in the particular situation of Fig.4.21 is shown in Fig.4.22. The curve fit is a polynomial function of 8th order. Although the scattering appears to be more pronounced in this situation, of Fig.4.21 the curve fit tracks well the correlation curve and this is an indication of reasonably good accuracy when the DSRD2 is combined with the optical filter KG.
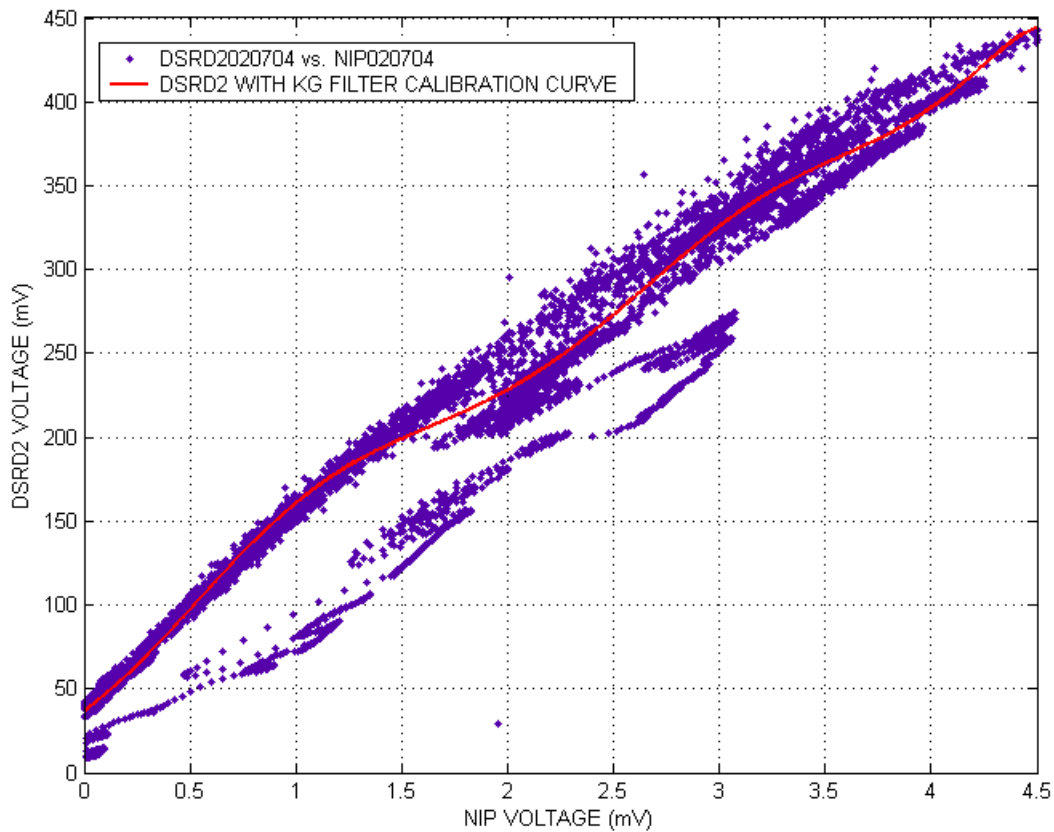
Figure 4.22: *A graph of correlation between the DSRD2 and the NIP measurements. The red curve represents the calibration factor which must be taken into account to correct the readings of the DSRD2 to conform with those from the NIP.*

From the two plots of figure 4.13 and figure 4.16, it can be understood that calibration of any radiometer based on data collected on a turbid day can not lead to a good result since the level of turbidness of the atmosphere is different and it occurs randomly. The

respective polynomial coefficients of the curve fit of Fig. 4.22 and the coefficient of the

goodness of fit are presented in Table 4.6.

Table 4.6: *A summary of the polynomial coefficients of the calibration curve and errors introduced by measuring direct solar radiation with the DSRD2 incorporating the KG filter on a turbid day.*

Data set	Polynomial coefficient								
	P_1	P_2	P_3	P_4	P_5	P_6	P_7	P_8	P_9
02/07/04	-0.545	9.230	-61.16	197.7	-311	189.8	-3.031	103.2	36.53
	The goodness of fit								
	SSE			R^2			RMSE		
	1.0060			0.99453			0.0994		

The correlation coefficient and the error in Table 4.6 suggest a better performance of the

DSRD2 when combined with the optical filter KG, in agreement with the results of Table

4.2 taken on a clear day.

4.4.3   The DSRD2 (with the BG39 filter) and the NIP

The plot of Fig. 4.26 refers to measurements of direct solar radiation taken using the

DSRD2 (incorporating optical filter BG39) and the NIP on a turbid day. The

measurements were taken on 5th October 2004. This plot displays an occurrence of heavy

interference in the period between 13:45 and 15:45. A comparison of Fig. 4.15 and

Fig.4.23 indicates in both cases higher readings by the DSRD2 in relation to the reference

instrument from 10:00 to 13:00. This suggests an influence of temperature in the readings

of the DSRD2 and can be a result of heat absorption.
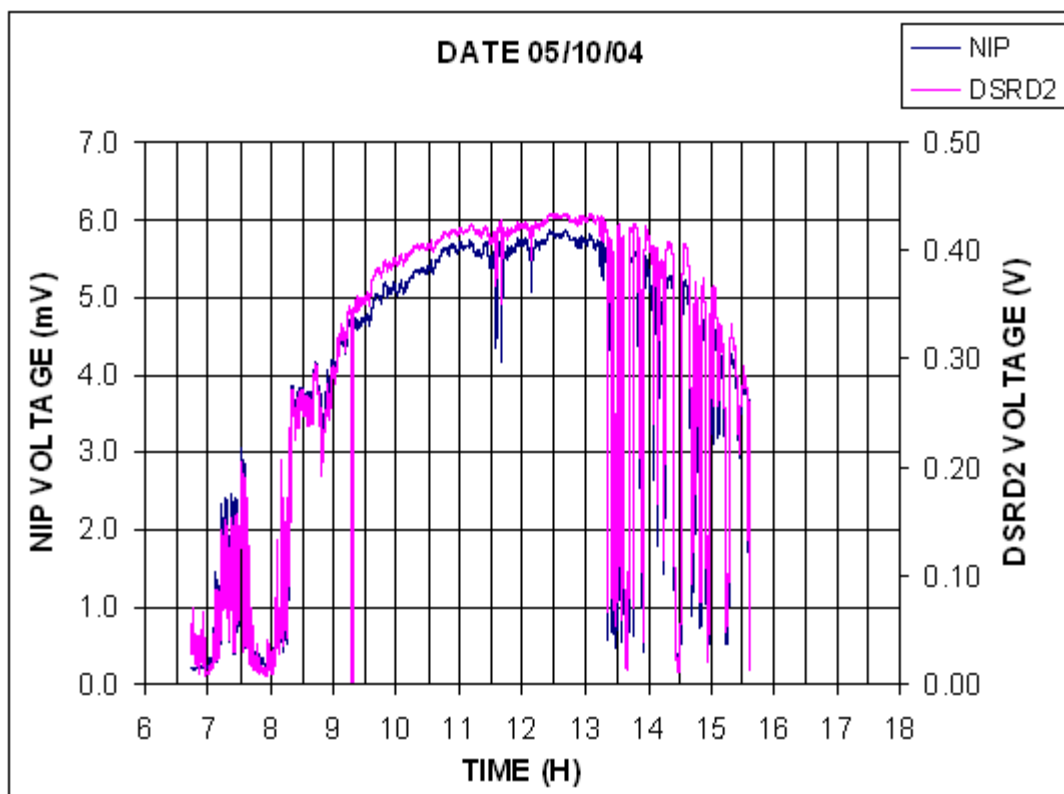
Figure 4.23: *A plot of direct solar radiation measured in volts using the DSRD2 and the NIP in a day with turbid sky. Here, the DSRD2 incorporates an optical glass filter BG39.*

It is also of interest to compare the trend in the magnitude of the data taken with the DSRD2 corrected to the data taken with the NIP. Figure 4.24 shows the plot for this case, and the results show that the NIP consistently reads higher than the DSRD2. It is worth noting that in the comparison, however, the DSRD2 tracks the variations of solar energy in a comparable manner to the reference instrument.

119
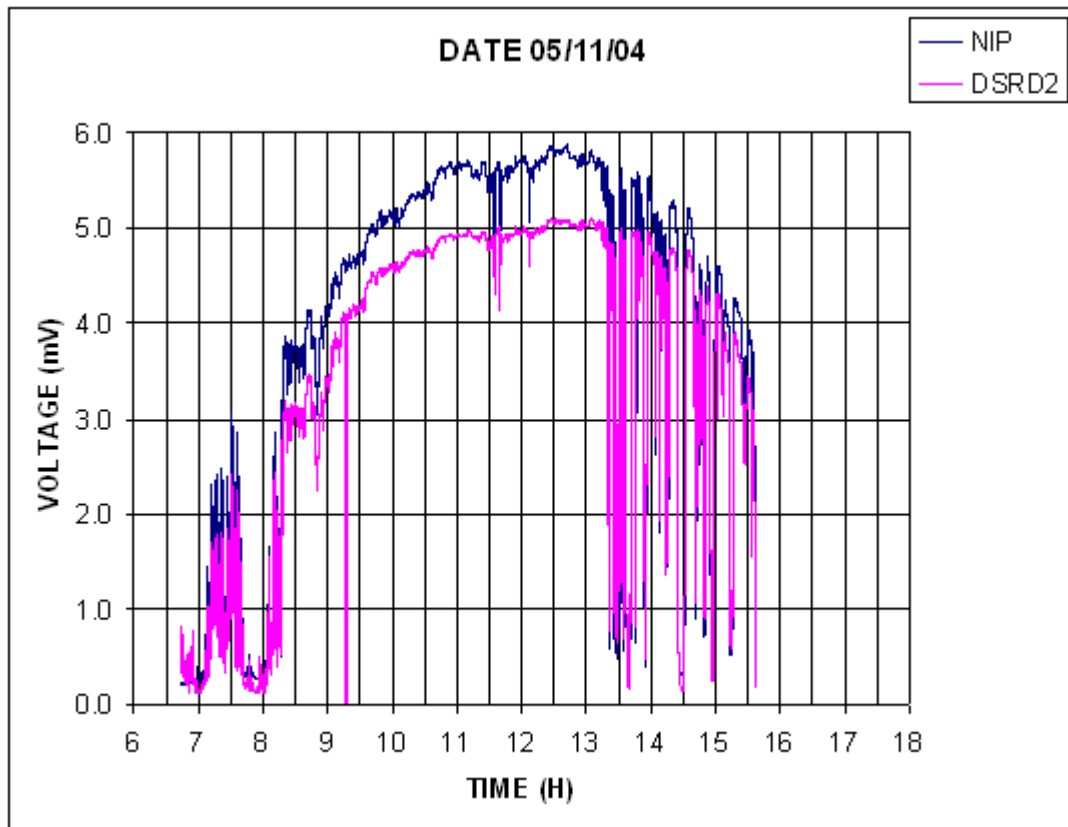
Figure 4.24: *A plot of direct solar radiation measured in volts using the DSRD2 and the NIP on a turbid day. The DSRD2 incorporates the optical glass filter BG39 and the magnitude of the measurements is corrected to that of the NIP.*

The curve fit to the plot of figure 4.24 is a polynomial function of 8th order. The plot

indicates that there is an intense scattering with the consequence that curve fitting is poor.

The curve fit in figure 4.22 is much better than here in figure 4.25. This is because there

is less scatter in figure 4.22 than in figure 4.25.
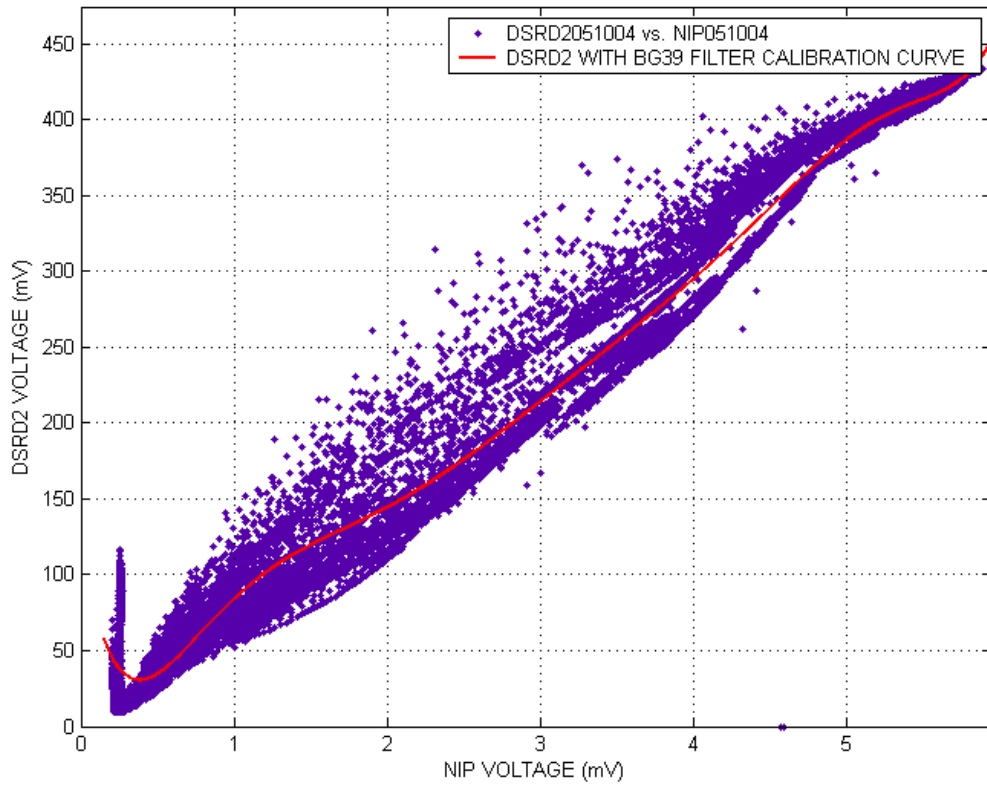
Figure 4.25: *A graph of correlation between the DSRD2 and the NIP measurements on a turbid day. The DSRD2 incorporates the BG39 filter. The plot shows a large scatter that leads to a poor fit.*

The coefficient deduced from the curve fit of figure 4.25 are summarized in Table 4.7

Table 4.7: *A summary of the polynomial coefficients of the calibration curve and errors introduced by measuring direct solar radiation with the DSRD2 incorporating the BG39 filter on a turbid day.*

Data set	Polynomial coefficient								
	P_1	P_2	P_3	P_4	P_5	P_6	P_7	P_8	P_9
05/10/04	0.142	-3.567	37.26	-209.3	681.7	-1289	1334	-586.3	118.9
	The goodness of fit								
	SSE		R^2			RMSE			
	1.2087		0.98665			0.1798			

The R^2 value is close to 1 and the RMSE value close to 0. This suggests a reasonably good fit. However, the values given in Table 4.6 are much closer to 1 and to 0 respectively, indicating that the curve fit is better when the measurements are taken with the DSRD2 coupled to the KG filter. A summary of the three situations studied is given in table 4.8, where it is noted that the results are better in the case of the KG filter. However, the results indicate that the fit is better with filter than without. This suggests that the spectral response of the DSRD2 can be improved using an optical glass filter.

Table 4.8: *A summary of the goodness of the correlation between the readings of the DSRD2 and the NIP for measurement taken on a turbid day.*

DSRD2	SSE	R^2	RMSE
With no filter	46.9472	0.98708	0.4144
With the KG filter	1.0060	0.99453	0.0994
With the BG39 filter	1.2087	0.98665	0.1798

In this work the filter that best suits the desired overall spectral response for the detector is the KG filter. This is because with this filter the values of SSE and RMSE are close to zero while the values of the R^2 are close to unity which is the ideal for a good curve fit.

4.5   Polar (or angular) response

The size of the full angle field of view of a radiometer can also contribute to the detection of unwanted radiation. A measurement of the polar response is intended to evaluate the suitability of the full angle field of view of the DSRD2. In this section results of direct solar radiation measured in volts using the DSRD2 and the NIP to investigate the
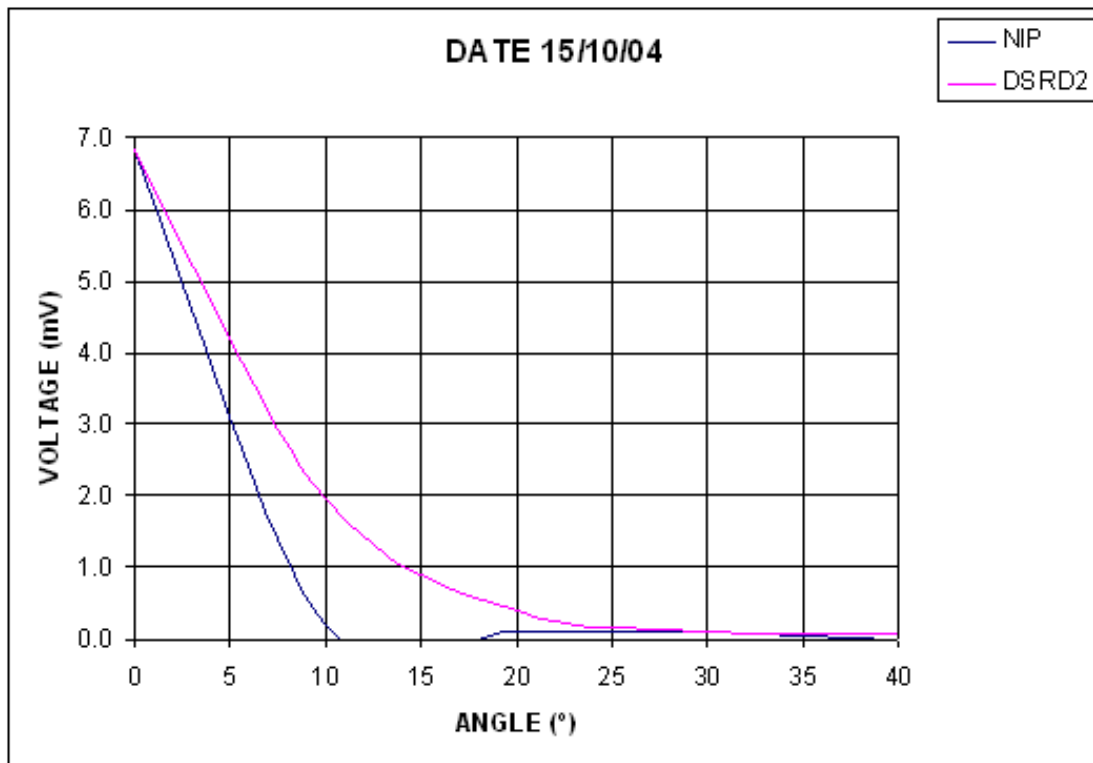
response of the DSRD2 to direct solar radiation at different angles of incidence are presented.

The measurements were carried out using the manual sun tracker, thus the accuracy of the measurements is assumed to provide an approximate idea of the goodness of the collimating hole of the DSRD2. The automatic sun tracker that would have been ideal for these type of measurements (because it can be controlled remotely) was not operating properly. The data were taken in the 3 situations of no filter, KG filter and BG39 filter. The data were collected on a clear sky day. The results of these measurements are presented below.

4.5.1 The DSRD2 (with no filter) and the NIP.

Figure 4.26 is a presentation of the direct solar radiation measured in volts for the assessment of the full angle field of view of the DSRD2. The plot shows how the amount of energy measured vary with respect to the angle of incidence of the solar beam. The measurements were taken on 15th October 2004.

The curve in blue color represents the NIP response and the curve in pink is the response of the DSRD2. The values of the direct solar radiation measured in volts using the DSRD2 were divided by 174.5207 in order to correct the magnitude of the readings to the readings of the reference. This allows the graphs generated by the two instruments to be plotted on a single graph. Thus, the data from the DSRD2 has been corrected to the reference data.

Figure 4.26: *A graph of direct solar radiation measured in volts using the DSRD2 and the NIP for different angles of incidence of the solar beam. Here, the DSRD2 incorporates no filter.*

The plot reveals a higher response by both instruments when the angle of incidence of the solar beam is equal to zero. This occurs when the solar beam strikes the surface of the sensing element at a perpendicular angle. This highlights the importance of the alignment of the detector in relation to the direction of the solar beam. Good readings are obtained up to about 10°, after which both instruments read very poorly and beyond 25° they read virtually zero.
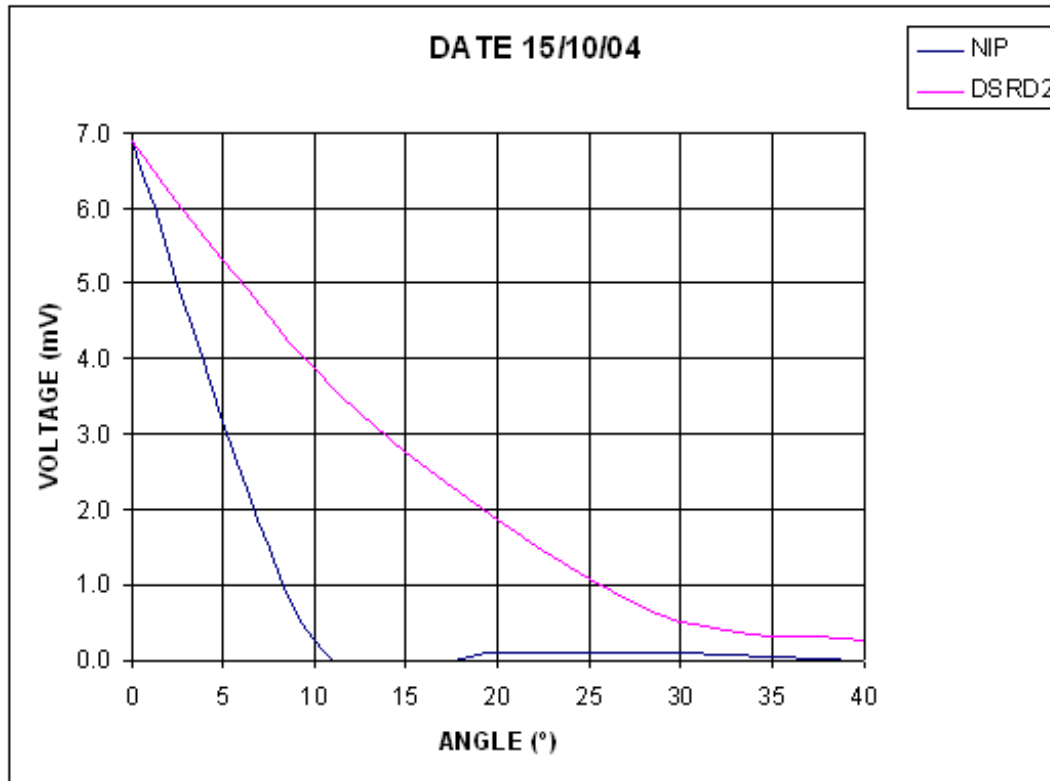
A comparison of the graph of the DSRD2 and the graph of the NIP indicates that the DSRD2 still detects radiation beyond 10º while the NIP detects no radiation at all. This is most probably due to the fact that the collimating hole in the DSRD2 is cylindrically

shaped whereas the one in the NIP is conical. The cylindrical shape of the hole in the DSRD2 allows the detection of radiation that has undergone multiple reflections. However, the characteristic responses are similar in that the sensitivity of the detectors to the incident solar beam decreases with the increase of the angle of incidence of the solar beam.

4.5.2 The DSRD2 (with the KG filter) and the NIP.

In accordance with the law of refraction the direction of the incident ray varies when it passes through mediums of different refractive index and this depends on the angle of incidence of the incident ray. This suggests that for certain angles of incidence of the solar beam, the DSRD2 with a filter may detect radiation with more significance compared to the situation when there is no filter. Thus, it is of interest to investigate the response of the DSRD2 incorporating a filter. The results of the polar response of the DSRD2 incorporating the KG filter are presented in Fig. 4.27. The measurements were taken on 15th October 2004.

The graphs indicate similar behavior of the instruments, that is a reduction in sensitivity occurs with an increase of the angle of incidence of the solar beam, a maximum detectable being 7 mV at 0°. However, the DSRD2 detects higher than the NIP for the angles of incidence greater than zero. It also detects beyond 10°, while the NIP does not. This may probably be due to the fact that the collimating hole of the DSRD2 is cylindrical whereas that of the NIP is conical. The DSRD2 then detects radiation that has been reflected.
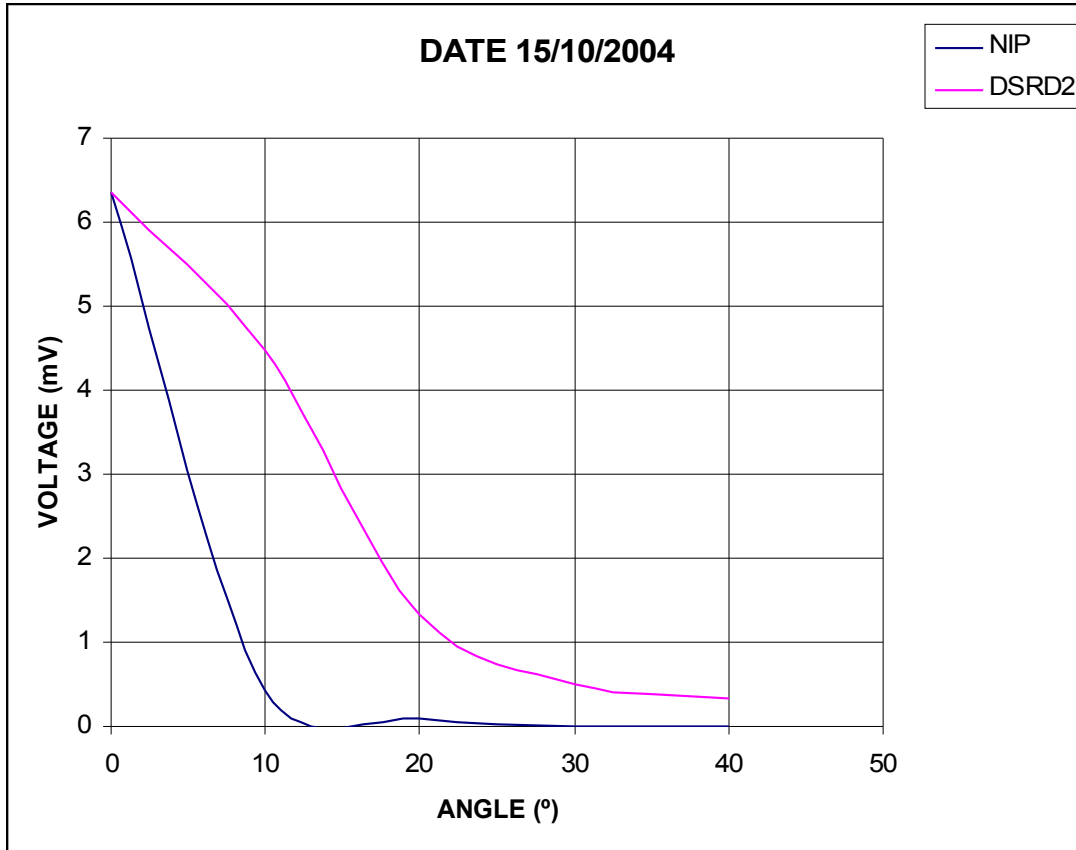
125

Figure 4.27: *A graph of direct solar radiation measured in volts using the DSRD2 and the NIP for different angles of incidence of solar beam. Here, the DSRD2 incorporates KG filter.*

A comparison of the angular response of the DSRD2 given in Fig. 4.26 for the situation with no filter and that given in Fig. 4.27 for the situation with the KG filter shows that in the first case the DSRD2 trace is moved away from the NIP trace. Thus, the DSRD2 with the KG filter reads higher than the NIP and higher than DSRD2 without the filter. This suggests that the KG filter enhances the angular response of the detector and this is caused by the refractive properties of the filter.

4.5.3 The DSRD2 (with the BG39 filter) and the NIP

Figure 4.28 is a plot of measurements carried out with the DSRD2 (coupling the BG39 filter) and the NIP. The measurements were taken on 15th October 2004.

Figure 4.28: *A graph of direct solar radiation measured in volts using the DSRD2 and the NIP for different angles of incidence of solar beam. Here, the DSRD2 incorporates BG39 filter.*

The figure show that the DSRD2 coupled to the BG39 filter has similar angular response in that a reduction in sensitivity occurs with increase of the angle of incidence of the solar beam. However, one aspect noticeable is that the trace indicates the DSRD2 over read in the interval ranging from ~4° to ~19°. It detects beyond 10° while the NIP does not. This

suggests that the refractive properties of the BG39 filter enhance the angular response of the DSRD2.

A comparison of the angular response of the DSRD2 given in Fig. 4.27 for the situation of the KG filter and that given in Fig. 4.28 for the situation of the BG39 filter leads to the fact that a better angular response is obtained with the first case.

4.6   Environmental stability

In the test for environmental stability, it was required to determine the effect of temperature changes to the output of the DSRD2. The temperature was measured with a sensor placed inside the detector housing. The black perspex was also replaced with a white perspex to minimize heat absorption and hence possible increases in temperature. The seal on the housing was also improved to attempt to reduce impurity accumulation onto the sensor surface, especially moisture and dust particles.

Only the former situation could be tested as temperature measurements could be carried out. However, the latter could not be tested and the "improvement" is only intuitive, in that surface impurities on the sensor would interfere with the incident solar beam. Thus, the detector output would be unrealistic.

4.6.1 The temperature inside of the housing of the DSRD2

Figure 4.29 is a plot of direct solar radiation measured in volts using the DSRD2 (coupled to the KG filter) and the NIP together with the measurements of the temperature in degrees centigrade inside the housing of the DSRD2. The measurements were carried out on 7th November 2004.
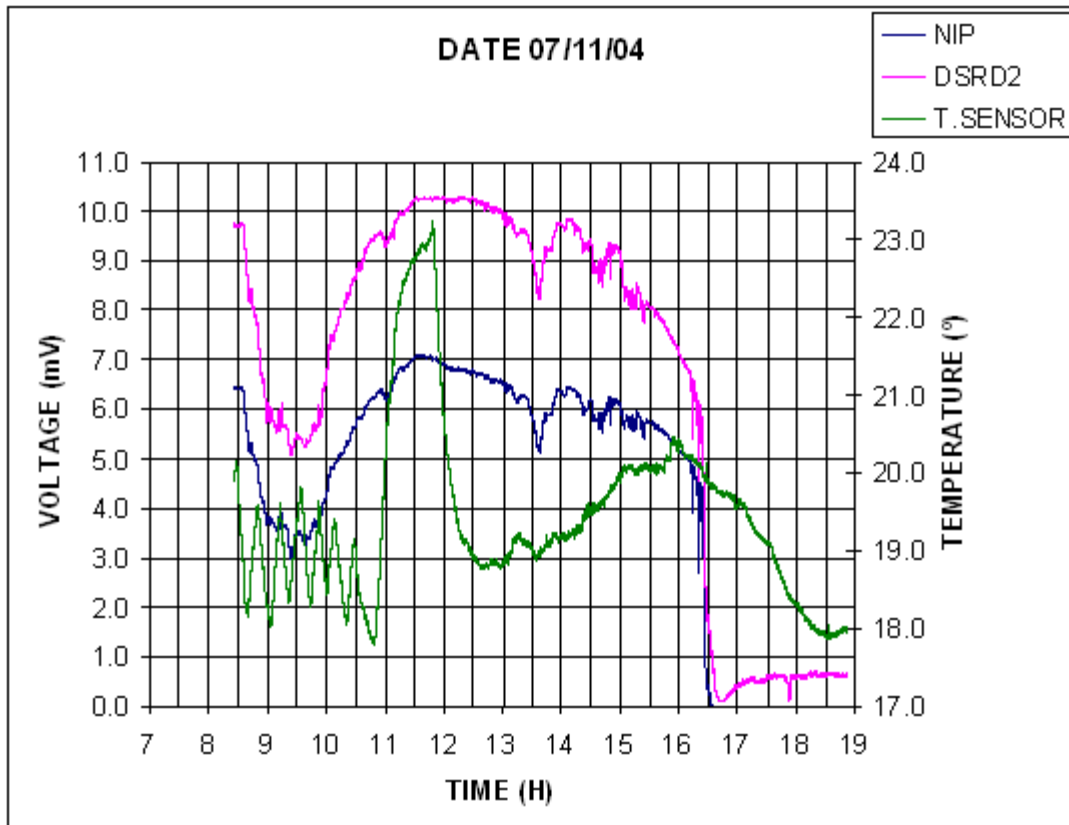
Figure 4.29: *A plot of direct solar radiation measured in volts using the DSRD2 fitted with the KG filter and the NIP. A plot of the variations in temperature inside of the housing of the DSRD2 is also presented.*

The graph in green color describes variations in temperature within the housing. The ambient temperature was not measured as the weather station was not operational at the time of this experiment. However, it is expected that it would be higher because inside the housing there is a shade. The magnitude of the DSRD2 measurements has been

129

corrected to the magnitude the NIP readings. The plot indicates that around 10:30 the temperature is lowest even though there is an increase of the amount of solar energy measured by both instruments. At around 16:30 measurements show an abrupt decrease in measured solar energy and this suggests that the sun was obscured. The temperature also falls, but at a slower rate. The temperature rise at around 11:00 with a sadden fall at 12:00 is of significance. If temperature had an effect, the readings by the DSRD2 would have been higher at this period. This is not so. This indicates that the variations of the temperature inside of the housing of the DSRD2 do not affect significantly the measurements performed with DSRD2.

4.6.2   The DSRD2 (with a white perspex) and the NIP

Results of the measurements of the direct solar radiation in volts measured using the DSRD2 with the black perspex replaced by a white perspex are presented in Fig. 4.30. The DSRD2 in this case is not coupled to any filter, the test being purely to test for changes in temperature. The measurements were performed on 4th August 2004.

The plot indicates a close coincidence between the readings of both instruments except in the time interval from 09:00 up to ~13:30. In this period the NIP reads higher than the DSRD2. The reason will probably be the fact that the sensing element of the DSRD2 is more sensitive to infrared radiation which is predominant when the scattering of the solar beam is intense. The DSRD2, however, still tracks the reference throughout the whole day. This result is not conclusive, however, since a better comparison would be between the black Perspex data and the white Perspex data. This was not possible since it would

imply a use of another detector whose optical property may differ from those of the

DSRD2.
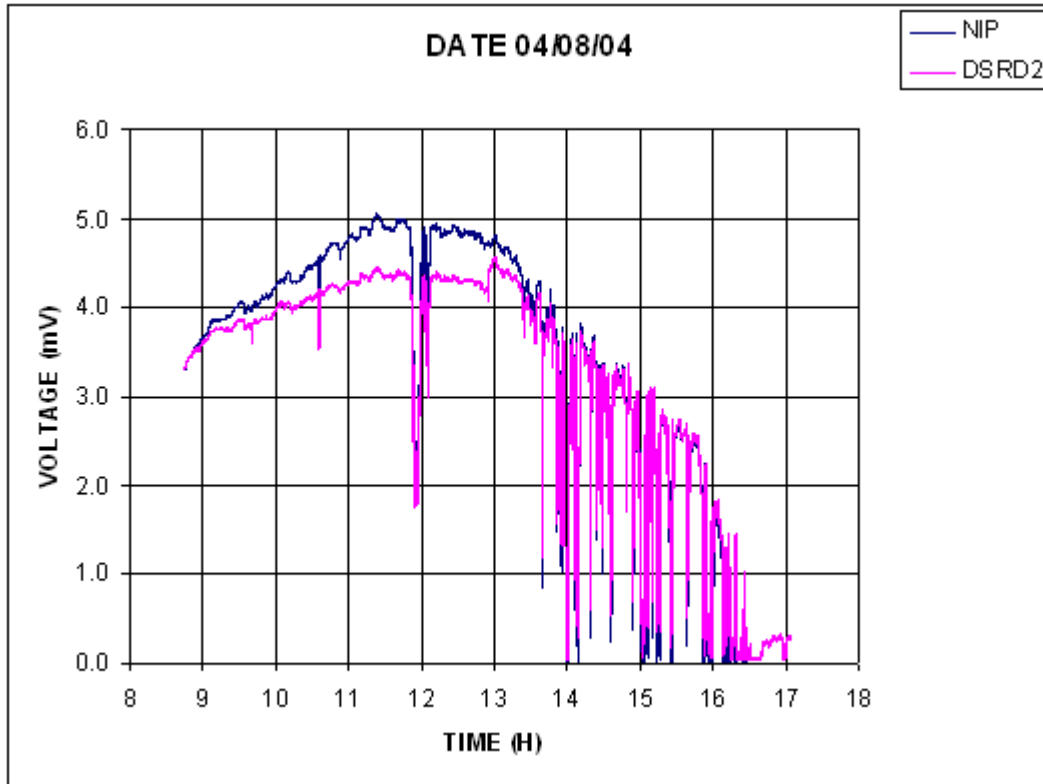
Figure 4.30: *A plot of the direct solar radiation measured in volts using the DSRD2 (with no filter) and the NIP. The black perspex is substituted with a white perspex. The DSRD2 readings are corrected to the NIP readings.*

4.7   Calibration

The calibration of any instrument is a requirement to ensure a collection of accurate data.

It is also intended to correct any imperfections which are unavoidable with commercial

instruments, some of which operate under hostile conditions like the radiometers.

Accurate measurements are necessary since they serve as a basis for the evaluation of the

performance of solar radiation systems such as solar energy concentrating systems, photovoltaic panels and solar thermal cookers.

The measurement comparison technique was the one used in this project to calibrate the DSRD against the Eppley NIP. For calibration of the DSRD2, several data sets which display the same pattern of performance by the DSRD2 incorporating the KG filter for a clear sky day, were combined in a single plot. Figure 4.31 is a plot of correlation between the measurements acquired from the NIP and the measurements acquired from the DSRD2.
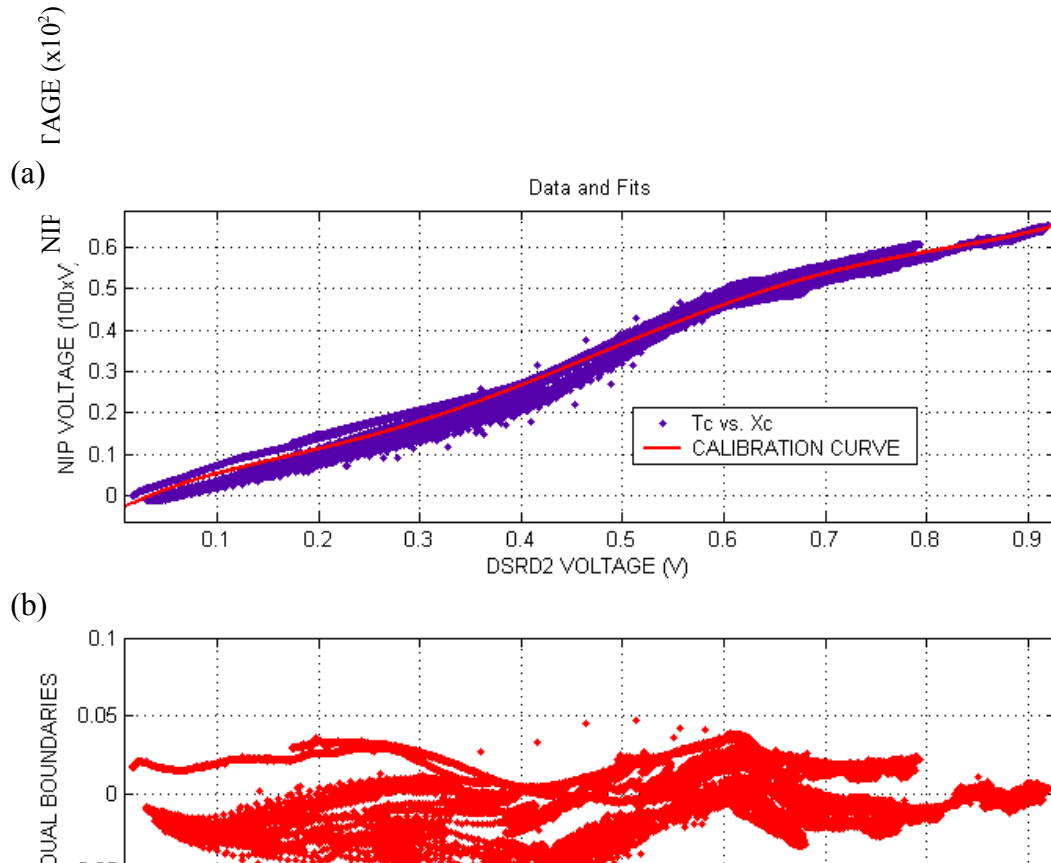
Figure 4.31: *A plot of correlation between the measurements acquired with the NIP and the DSRD2 incorporating the KG filter (a) and a plot of the residuals, the diference between the curve fit and the measured data points, (b).*

132

The plot shows also the curve fit to the correlation curve using a polynomial regression. A plot of the residuals is also given which indicates the bounds of the fluctuations of the data points with respect to the curve fit. For a good calibration curve the plot of the residuals ideally indicate a random fluctuation within the boundaries close to zero. The blue line in (a) is a scatter plot of the correlation of the measured data points from the NIP and from the DSRD2 while the red line is the fitting curve which is used to calibrate the DSRD2. The values of the measurements obtained from the NIP were multiplied by 100 the magnitudes of the measurements from both instruments. This is because the signal from the DSRD2 is 100 times larger than the signal from the NIP. The curve fit is a polynomial regression of 5th order given by

$$P = P_1 x^5 + P_2 x^4 + P_3 x^3 + P_4 x^2 + P_5 x + P_6 \qquad (4.2)$$

where P_1, P_2, …P_6 are the polynomial coefficients whose values are given in Table 4.9 and x represents the data points. The plot in (a) indicates a fairly good fit. However, the plot of the residuals indicates a small skew towards the negative. This means that the margin of deviation of the measured points to the curve fit is small. Thus, the magnitude of errors introduced by the calibration curve is somewhat negligible.

Table 4.9: *A summary of the 5th order polynomial coefficients of the curve fit used for calibration of the DSRD2. The errors that the calibration curve introduces to the measurements with the DSRD2 are also presented.*

Polynomial coefficients					
P_1	P_2	P_3	P_4	P_5	P_6
8.656	-21.07	17.4	-5.539	1.324	-0.03785
Goodness of fit					
SSE		R^2		RMSE	
28.987		0.9850		0.01657	

The table indicates that the R^2 value is 0.9850 and this is close to unity. The value of the root-mean-square-error is 0.01657 which is close to zero. The 5th order polynomial regression was chosen because it gives the best prediction when tested with other sets of data measured on different dates under different weather conditions. This is not so with other polynomials.

Figure 4.32 is a plot of correlation (a) together with the plot of residuals (b). The curve fit is a polynomial regression of 9th order given by

$$P = P_1x^9 + P_2x^8 + P_3x^7 + P_4x^6 + P_5x^5 + P_6x^4 + P_7x^3 + P_8x^2 + P_9x + P_{10} \qquad (4.3)$$
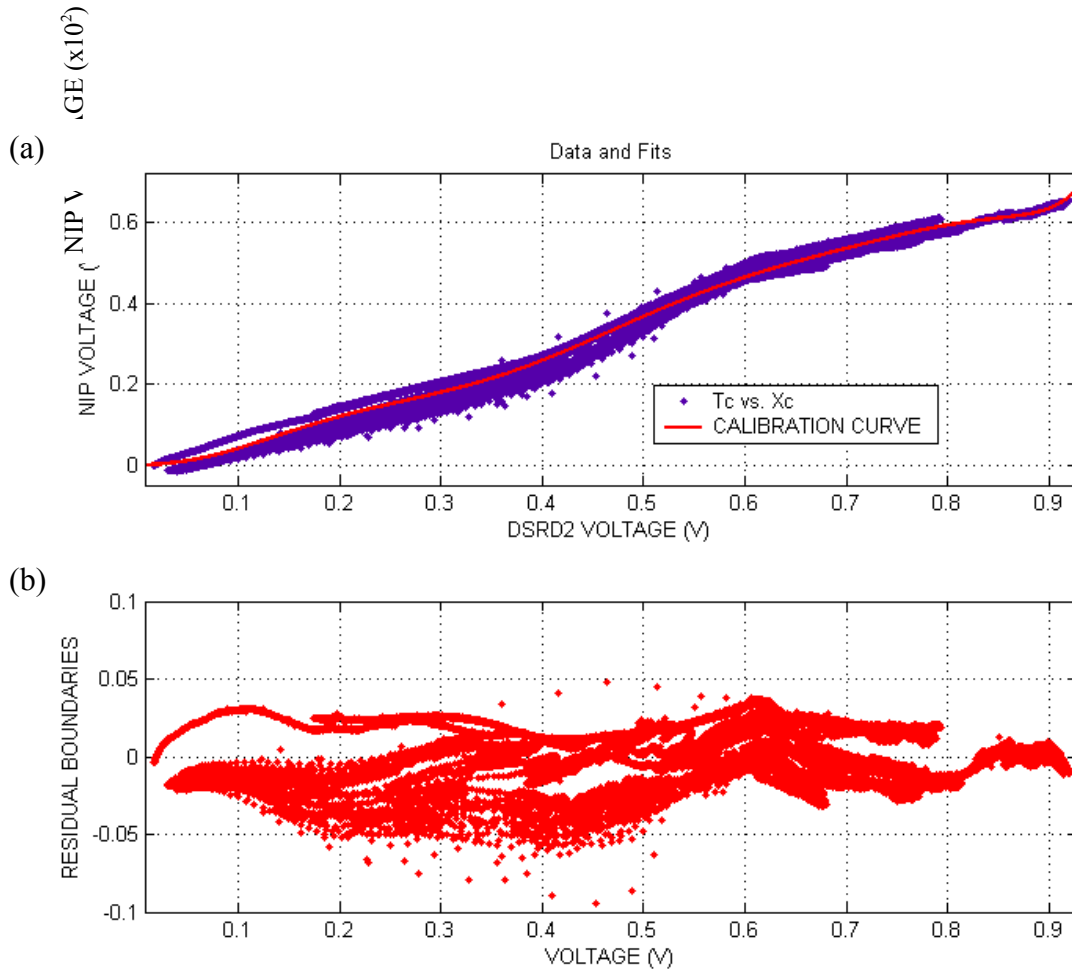
where P_1, P_2, ... P_{10} are the coefficients of the polynomial regression and x represents the data points. The 9th order polynomial was chosen for a comparison gives a very good curve fit.

The red line on plot (a) represents the curve fit that has been used for the calibration of the DSRD2. The curve fit is a polynomial regression of 9th order whose coefficients are shown in Table 4.10. Presented on plot (b) is the scatter graph of the residuals for the curve fit. The plot (a) indicates a very good fit. The plot of the residuals shows that the deviations of the data points to the curve fit are randomly close to zero even though they are skewed slightly to the negative.

Table 4.10: *A summary of the 9th order polynomial coefficients of the curve fit used for calibration of the DSRD2. The errors that the calibration curve introduces to the measurements with the DSRD2 are also presented.*
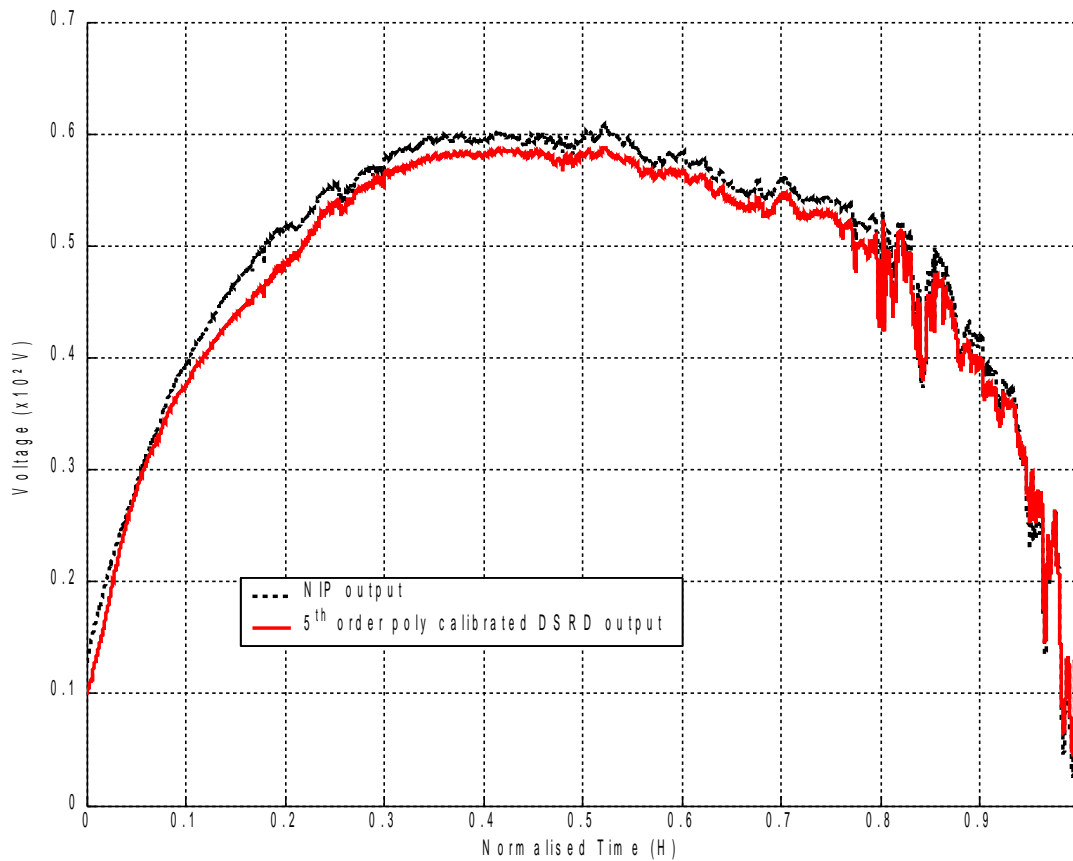
Polynomial coefficients									
P_1	P_2	P_3	P_4	P_5	P_6	P_7	P_8	P_9	P_{10}
1027	-4067	6593	-5580	2581	-6047	45.99	5.848	-0.319	0.0099
Goodness of fit									
SSE			R^2				RMSE		
27.7			0.9857				0.0162		

The table indicates that the R^2 value is 0.9857 and this is close to unity. The value of the root-mean-square-error is 0.0162 which is close to zero.

A comparison of Fig. 4.31 and Fig. 4.32 indicates that the plot of the deviations of the data points to the curve fit are closer to zero better in the case of the 9th order regression than in the case 5th order regression. Further to this, a comparison of the SSE, the R^2 and

the RMSE values shows that the 9th order polynomial regression indicates a better correlation and a smaller error. However, in a general test, the polynomial coefficients on another data set collected on a different date, the 5th order polynomial coefficients reveal better results. A comparison of the test of the two polynomials is presented in the following paragraphs for the same data set.

Figure 4.33 shows a scatter plot of the measurements obtained from the NIP and those obtained from the DSRD2 incorporating the KG filter specifically for testing the calibration coefficients obtained from the fitting by the 5th order regression polynomial.

Figure 4.33: *A scatter plot of measurements carried out with the DSRD2 and the NIP. The polynomial coefficients obtained from the calibration curve of 5th order were used.*

The measurements were carried out with both instruments but on a day with different atmospheric conditions to those used in the plot presented in Fig. 4.30.

The graph in black color is a plot of measurements obtained from the NIP. The values of the measurements performed with NIP were multiplied by 100, to reduce the order of magnitude of the measurements obtained from the NIP to those obtained from the DSRD2. The graph in red color represents the test of the calibration coefficients obtained from the 5th order polynomial regression. The plot indicates that the measurements acquired from the DSRD2 even though slightly lower magnitude, track very closely the measurements given by the reference instrument when the DSRD2 is calibrated with a polynomial regression of the 5th order. The data set presented here corresponds to a clear sky day.

Figure 4.34 is a plot of correlation between the measurements from the NIP and those from the DSRD2 calibrated output. This graph has been generated from the data of figure 4.33. The blue graph is a scatter plot of correlation between readings of the NIP and the readings of the DSRD2 calibrated with the polynomial regression of 5th order. Presented in red color is the curve fit for the goodness of the correlation. The curve fit is a linear regression whose equation is given by

$$A = 0.977\,T - 0.00369 \qquad\qquad (4.4)$$

as shown on the plot. Here, A represents the measurements obtained from the NIP and T are the data points from the readings of the DSRD2.
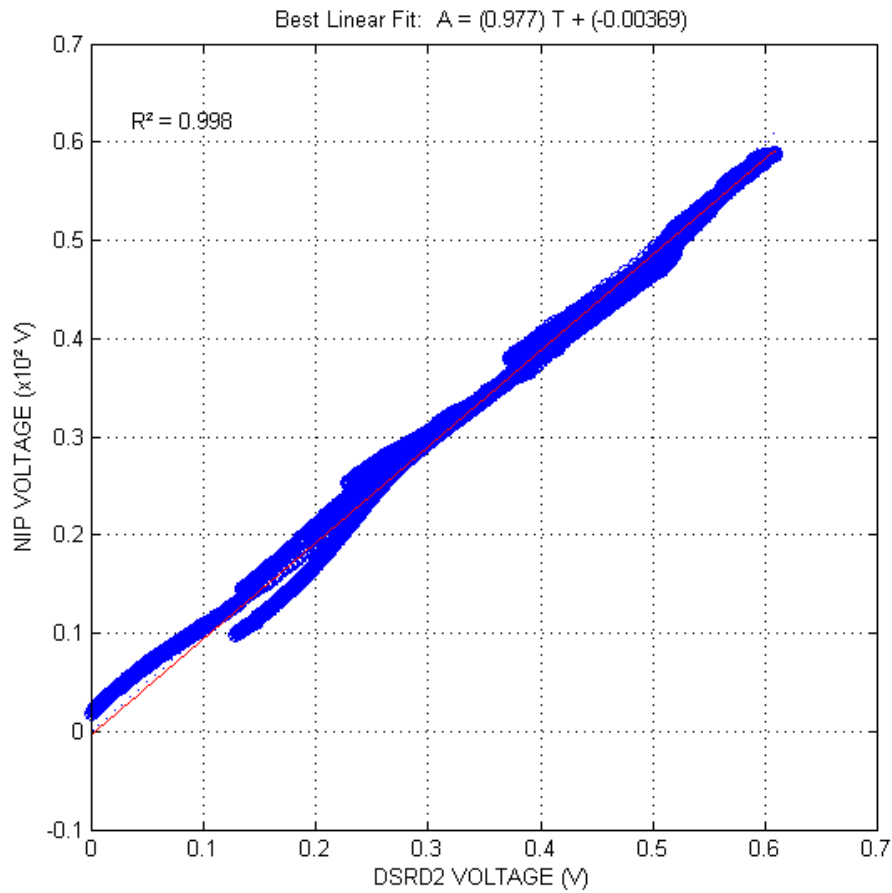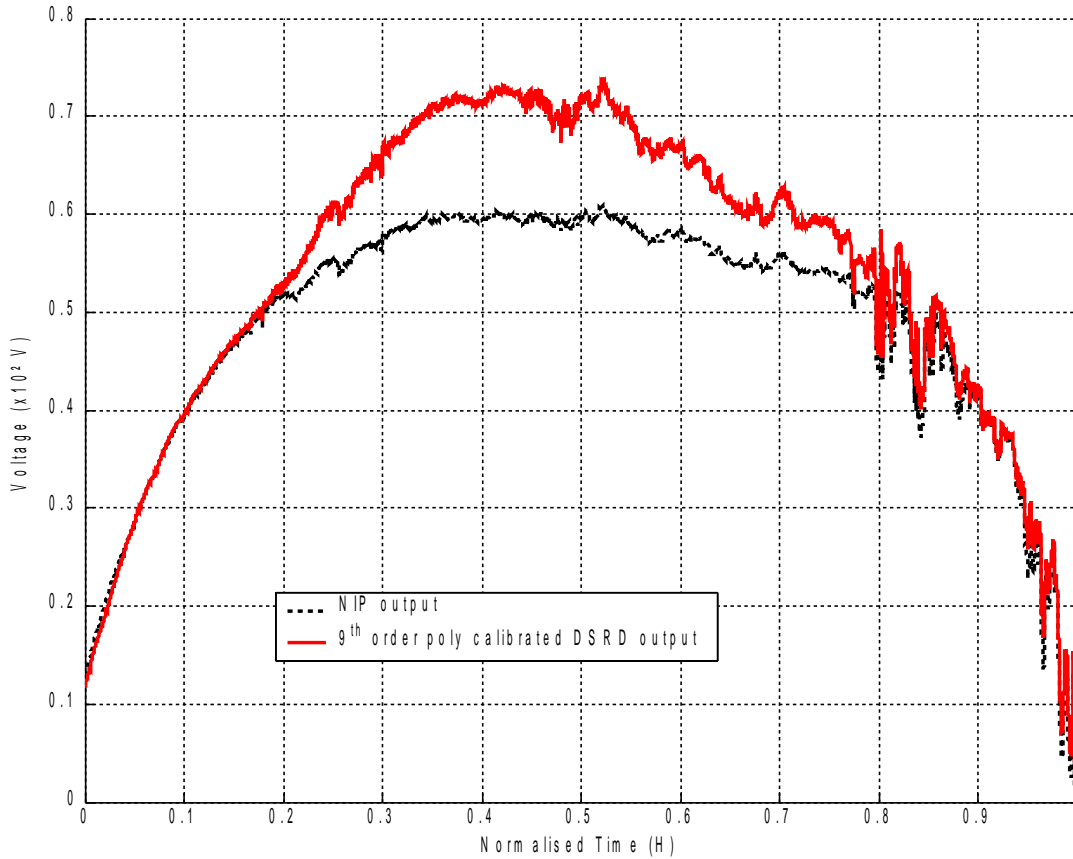
Figure 4.34: *A plot of correlation between measurements obtained from the NIP and those obtained from the DSRD2. This plot corresponds to the test of the polynomial coefficients resulting from the 5th order polynomial regression.*

The R^2 value is 0.9976 which is nearly equal to unity and the RMSE value is 0.0175 which is close to zero. This result shows that the 5th order polynomial regression is ideal for calibration of the DSRD2 incorporating the optical glass filter KG. A different result is given below for the 9th order polynomial.

In Figure 4.35, a plot of the test of the calibration coefficients obtained from the 9th order polynomial regression curve fit is presented. This plot refers to the same data set used in the plot in Fig. 4.33. The measurements carried out with the NIP are represented by the

graph in black and those obtained from the DSRD2 calibrated with the 9th order polynomial regression are indicated with the graph in red.


Figure 4.35: *A scatter plot of measurements carried out with the DSRD2 and the NIP. The polynomial coefficients obtained from the calibration curve of 9th order were used.*

The plot indicates that with the polynomial coefficients obtained from the 9th order the measurements carried out with the DSRD2 do not track very well the behavior of the NIP. This is especially apparent in time interval that ranges from 0.2 hours to 0.8 hours.

Figure 4.36 is a plot of correlation between readings of the NIP and those obtained from the DSRD2 with the 9th order polynomial coefficients. The blue graph is a scatter plot of the data points that represent the readings of both instruments and the red graph is the curve fit. The curve fit is a linear regression whose equation is

$$A = 1.26T - 0.0742 \tag{4.5}$$

as shown on the plot. A represents the measurements obtained from the NIP and T are the data points from the readings of the DSRD2.
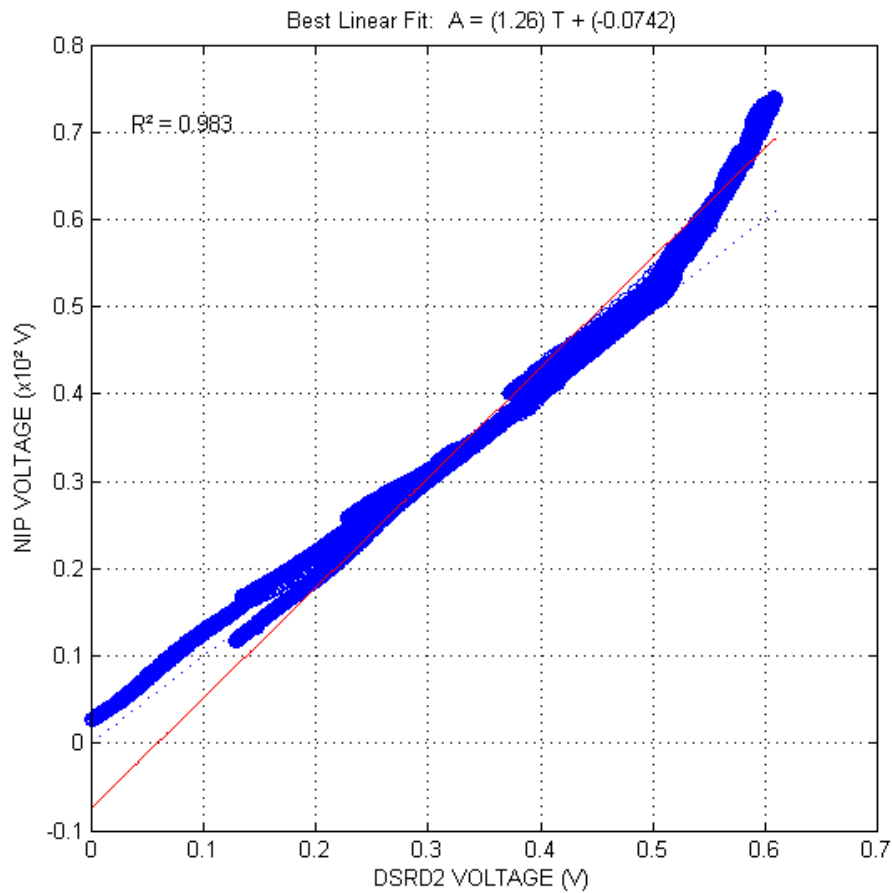
Figure 4.36: *A plot of correlation between measurements obtained from the NIP and those obtained from the DSRD2. This plot corresponds to the test of the polynomial coefficients resulting from the 9th order polynomial regression.*

140

Another of the polynomial coefficients attained from the 5th order polynomial regression for a day with different weather conditions presented in figure 4.37. This is a scatter plot of direct solar radiation measurements performed with the NIP and the DSRD2. In this plot scattering of solar radiation soon after sunrise and just before sunset is
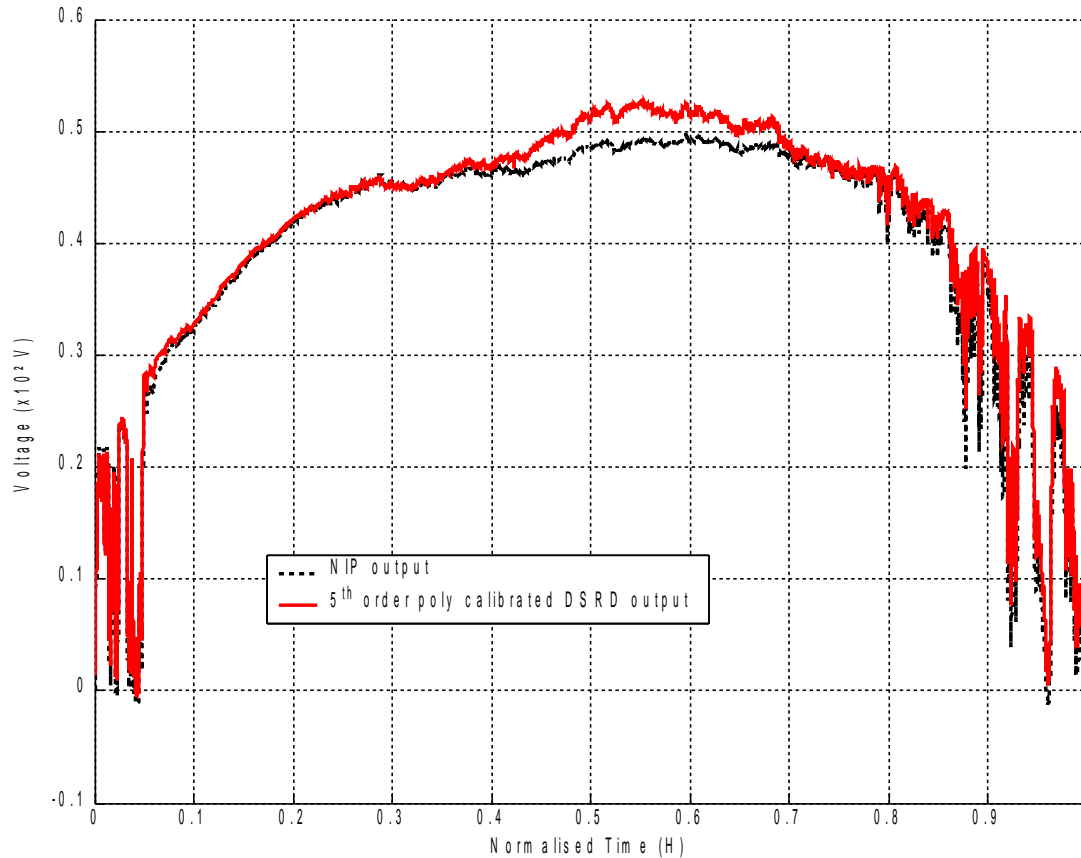
Figure 4.37: *A scatter plot of measurements performed with the DSRD2 and the NIP. The polynomial coefficients obtained from the calibration curve of 5th order were used.*

noticeable. The plot reveals that, except between 0.4 h and 0.7 h the DSRD2 tracks the variations in solar energy very well. The discrepancy, between 0.4 h and 0.7 h occurs because of the variations in sensitivity of the sensing element of the DSRD2 with the wavelength of the radiation and this is a random situation.

Figure 4.38 is a plot of the measurements performed with NIP and DSRD2 for the same date as in Fig. 4.37. This is for testing the consistence of the 9th order polynomial coefficients.
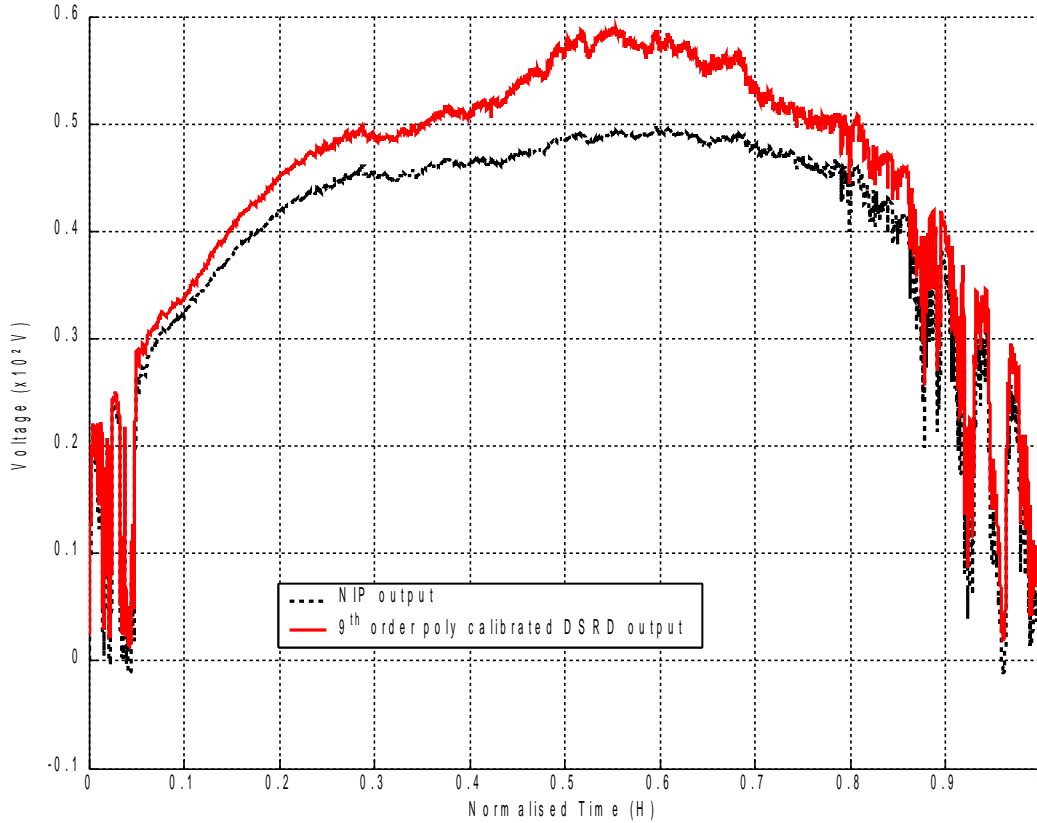
Figure 4.38: *A scatter plot of measurements performed with the DSRD2 and the NIP. The polynomial coefficients obtained from the calibration curve of 9th order were used.*

The result reveals that with the 9th order polynomial coefficients, the DSRD2 consistently overestimates the incident solar energy over a wide range of time interval. This means that the 9th order polynomial regression is not very good for the calibration of the DSRD2. It is not necessary to present the fitting curve for the two cases since the same result as in figures 4.34 and 4.36 is apparent.

Table 4.11 is a summary of the magnitude of the error introduced in the measurements of the direct solar radiation using the DSRD2 incorporating the KG filter for both the 5th and the 9th order polynomial regression.

Table 4.11 *A summary of the goodness of the correlation between the readings of the DSRD2 and the NIP. This represents the errors introduced by measuring direct solar radiation with the DSRD2 calibrated with the 5th order and with the 9th order polynomial regression.*

Order of the polynomial regression	R^2	RMSE
5th	0.9976	0.0175
	0.9950	0.0183
9th	0.9830	0.0688
	0.9901	0.0524

A comparison of the R^2 values and the RMSE values shown in the table reveals that the 5th order polynomial regression is the best option for the calibration of the DSRD2. This is because the values of R^2 are much closer to unity than those obtained from calibrating with the 9th order polynomial regression. The values of the RMSE obtained by calibrating with the 5th order polynomial regression are much closer to zero than those obtained by calibrating with the 9th order polynomial regression.

4.8   Factors influencing the uncertainty in the measurements.

The uncertainty of the DSRD readings depends on a large number of factors besides the calibration factor described in section 4.7. The other relevant factors are random noise, temperature, aperture cleanliness, solar tracking errors, wind and long-term stability. These are described briefly below.

One source of random noise encountered during measurements was an irregular presence of birds at the location where the instruments were mounted. At times the birds would perch over the detectors obstructing the solar beam to the detector. The detector housing is a black plastic enclosure and an absorber of long wave radiation. This is a thermal energy source which could cause a rise in temperature in the vicinity of the detector. Nevertheless, this factor has been discounted by the results, possibly because the sensor can operate under temperatures ranging from 0 °C to 70 °C according to manufacturer specifications.

Aperture cleanliness is another factor to be considered. In general, a window that looks mildly dirty can easily absorb and reflect a portion of the incoming radiation. In this particular situation the windows of the DSRD2 and the NIP were regularly checked and cleaned.

The tracking mechanism used in this research is manually operated and this means that every few hours adjustments have to be made of the declination and azimuth to ensure that the detectors are well aligned towards the sun. The sun tracker is designed to accommodate up to three instruments and incorporates worm and gear fine adjustments for declination. The ST-3 solar tracker model uses a clock-based motor which makes one revolution every 24 hours and the cable that feeds the output signal from the instrument to the data acquisition system swings around on the tracker polar axis every revolution.

The wind speed effect was not tested in the experiment but it may have an effect on the output signal of the DSRD2 since the wind can cause a vibration of the mounting mechanism of the tracker on which the DSRD2 is mounted and this may lead to offset errors. The temperature may also be altered by wind such that offset errors occur. Another consideration is that wind may contribute to the transport of dust and moisture onto the surface of the filter and this would cause a scattering of the incident radiation which would lead to a distortion of the readings by the DSRD2.

Chapter 5

5. Conclusions and possible future work

This research work has highlighted the fact that proper design and calibration can go a long way to ensure that the quality of solar radiation data is good and reliable. This will assist in the design of low cost instrumentation. This is the main contribution of this research work to knowledge.

The detector that was to be characterized had a housing, which was not well sealed. This contributes to the detection of unwanted radiations and accumulation of moisture and dust onto the surface of the sensing element through these improperly sealed sections. These resulted on a bad performance of the detector and hence an unreliable quality of data collected. The detector is also characterized by a spectral response that varies with respect to the wavelength of the incident radiation and this is not ideal.

The results obtained from the detector that was to be characterized and improved (designated by DSRD1) revealed that the original properties of the sensing element had been altered over a period of time. This is associated with the design of the housing of the detector which was not properly constructed to prevent moisture and dust particles from accumulating onto the surface of the sensing element. Thus, a proper sealing of the housing is vital to protect the detector from adverse weather conditions and to ensure good quality data. Further to this, a properly designed housing would ensure life time durability of the detector. The results have also indicated that the measurements performed with the DSRD are not significantly influenced by the temperature in the interior of the housing.

A main weakness of the detector characterized in this work was its selective spectral response. The results have shown that quantum detectors, despite their selective spectral response, can be used for measuring direct solar radiation with a good and reliable accuracy. The spectral response of a quantum detector can be modified to the desired spectral response by combining the spectral transmittance of an optical glass filter with the spectral responsivity of a photodiode.

The measurements carried out for the characterization of the DSRD in terms of the polar response show that the dimensions of the collimating hole are acceptable. This is because the polar response of the detector is similar to that of the reference instrument. It is only the magnitudes of the readings from the two instruments that are different but this difference has been corrected by calibration.

The magnitude of the measurements obtained from the DSRD is larger than that of the measurements obtained from the reference instrument. This shows that quantum detectors are highly sensitive. Thus, they are ideal for measuring fluctuating events such as solar radiation. A proper calibration of the detector can ensure results that are comparable, in magnitude, to that of the reference.

The graphical and the numerical measures of the correlation between measurements obtained from the reference instrument, and those obtained from the modified DSRD indicate a better performance by the DSRD. In the numerical case, the correlation value between the reference instrument and the modified DSRD is ~0.9976. This is close to

unity, which means that there is good agreement in the data acquired by the DSRD and data acquired by the reference instrument. The value of the root mean square error is ~0.0175 which is close to zero. This means that the differences between the DSRD data and the NIP data are not significant. Both of these values are an indication of a good performance of the DSRD in comparison to the reference instrument.

In this manner the modifications carried out on the DSRD have contributed to improving the quality of data acquired by the detector. If designed properly, quantum detectors are better alternatives for low cost designs in solar radiation instrumentation.

Possible future work will be concentrating on the control of the variations of the calibration factor. This is because the sensitivity of the sensing element of the DSRD may vary with time and with the intensity of the incident radiation. The design of a suitable sun tracker in the perspective of simple, user-friendly and low cost instrumentation will also be considered.

References

1. Ångström A. and Rodhe B. (1996), "*Pyrheliometric measurement with special regard to the circumsolar sky radiation",* Newport R.I. and Swedish Meteorolgical and Hydrological Institute, Tellus XVIII., Trigger.
2. Burr-Brown (1996), "*Optical sensors*", in IC data book, **PP**, Tucson.

3. Campbell Scientific (1998), *"Calculating sunshine hours from pyranometer/solarimeter data"*, Technical note 18, Campbell Scientific, Leicestershire, UK.

4. Close K.J. and Yarwood J. (1976), *"Electronics"*, University Press, London.

5. Colle S. et al (1999), *"Distribution of solar irradiance in Brazil derived from geostationary satellite data"*, Solar World Congress, 04-09 July 1999, Jerusalem, Israel, p50

6. Cuamba B.C. et al (2001), *"General characterization of the solar radiation components in Mozambique"*, Unpublished.

7. Dhavraj M. (1998), *"The setting up and calibration of radiometers for the measurements of direct and diffuse solar radiation at the university of Durban-Westville",* MSc thesis, University of Durban-Westville, Durban, South Africa.

8. Duffie J.A. and Beckman W.A. (1991), *"Solar engineering of thermal processes"*, 2nd ed, Wiley, New York.

9. Gore B. (2003), *"Scaling up biogas technology in Nepal"* Proc. Workshop in energy for development technology, 06-08 August 2003, Valley Trust, Durban, South Africa.

10. Guyot G. (1998), *"Physics of the environment and climate"*, 1st ed, Wiley and Praxis, New York.

11. Hughes E. (1995), "*Electrical technology*", 7th ed, Prentice Hall, London.

12. Iziomon M.G., et al (1999), *"Global solar irradiance and clearness index in South-West Germany"*, Solar Energy Congress, 04-09 July 1999, Jerusalem, Israel.

13. Jacovides C.P. et al (1996), *"On the diffuse fraction of daily and monthly global radiation for the the Island of Cyprus"*, Solar Energy, **56**, 565-572.

14. McDaniels D.K. (1984), "*The sun our future energy source",* 2nd ed, Wiley, New York.

15. McPherson M. (1997), *"Irradiated silicon detectors as relaxation devices"*, PhD thesis, Lancaster University, UK.

16. McPherson M., Jones BK., Sloan T (1997), "*Suppression of irradiation effects in gold-doped silicon detectors*", J. Phys. D: Appl. Phys. **30** 3028

17. McPherson M. (2002), "*Capacitive effects in neutron-irradiated silicon diodes*", Nucl. Inst. Meth. A **488** 100-109

18. McPherson (2003), verbal communication.

19. McPherson M. (2004[a]), *"The space charge relaxation behaviour of silicon diodes irradiated with 1 MeV neutrons"*, Nucl. Int. and Meth. A **517**, 42-53

20. McPherson M. (2004[b]), "*Infrared photoconduction in radiation-damaged silicon diodes*", J. Opt. A: Pure Appl. Opt. **7**, 1-6

21. Myers D.R. (2003) *"Solar radiation modeling and measurement for renewable energy applications: Data and model quality"*, Proc. Int. Expert Conf. on Mathematical Modeling of Solar Radiation and Daylight: challenges for 21st Century, 15-16 September 2003, Edinburgh, Scotland.

22. Odon A. (2001), *"Processing of signal of pyroelectric sensor in laser energy meter"*, Measurement Science Review, **1**, 215-218.

23. Rivington M., Matthews K.B. and Buchan K. (2002), "*A comparison of methods for providing solar radiation data to crop models and decision support systems'*,

Proc. Int. Environmental Modelling and Software Society, Lugano, Switzerland, 24-27 June 2002, **3**, 193-198

24. Ryer A. (1998), *"Light measurement handbook"*, International light, Inc., Newburyport, USA.

25. Smith R.J. (1983*), "Circuits, devices and systems"*, 4th ed, Wiley, New York.

26. Streetman B.G. (1990), "*Solid state electronic devices*", 3rd ed., Prentice Hall, New York.

27. Sze S.M. (1969), "*Physics of semiconductor devices*", Wiley, New York.

28. Thacher P.D., Boyson W.E. and King D.L. (2000) "*Investigation of factors influencing the accuracy of pyrheliometer calibration"*, Proc. 28th IEEE Conf. of the PV Specialists, 15-22 September 2000, Anchorage AK, USA, 1395-1398

29. Twidell J. and Weir T. (1996), *"Renewable energy resources"*, 1st ed, Cambridge University Press, Cambridge, UK.

30. Uiso C.B.S. (2004), *"Solar radiation"*, Proc. 8th College on Thin Film Technology, University of Dar es Salaam, Dar es Salaam, Tanzania, **8.6**, 1-28

31. van den Heetkamp R. (2002), *"The development of small solar concentrating systems with heat storage for rural food preparation"*, Physica Scripta **T97**, 99-106.

32. Website 1 (www.almashriq.hiof.no)

33. Website 2 (www.cmdl.com)

34. Website 3 (www.me.umn.edu)

35. Website 4 (www.iamest.jrc.it)

36. Website 5 (www.eko.co.jp)

37. Website 6 (www.besoptics.com)

38. Website 7 (www.optics.online.com)